НАЦІОНАЛЬНА АКАДЕМІЯ НАУК УКРАЇНИ
ІНСТИТУТ ЗАГАЛЬНОЇ ТА НЕОРГАНІЧНОЇ ХІМІЇ імені В. І. ВЕРНАДСЬКОГО
КИЇВСЬКИЙ НАЦІОНАЛЬНИЙ УНІВЕРСИТЕТ імені ТАРАСА ШЕВЧЕНКА

УКРАЇНСЬКИЙ ХІМІЧНИЙ ЖУРНАЛ

№ 5
Том 92 / Vol. 92
2026
https://ucj.org.ua

UKRAINIAN CHEMISTRY JOURNAL

Зміст

ФІЗИЧНА ХІМІЯ

О. Пасенко, Є. С. Осокін, А. В. Іванченко
ДСОРБЦІЯ ІОНІВ Pb^{2+} КОСТРИЦЕВИМ БІОВУГІЛЛЯМ ІЗ ТЕХНІЧНОЇ КОНОПЛІ (CANNABIS SATIVA) 3

ЕЛЕКТРОХІМІЯ

О. В. Потапенко, Г. В. Потапенко, В. О. Олійник, В. А. Сірош, С. Тичина, Чанцзі Чжоу, Чі Сянь Вонг, Чанбо Юй, Ченьчунь Чжан
ВПЛИВ ПРИРОДИ ЗВ'ЯЗУВАЧА НА ЕЛЕКТРОХІМІЧНІ ВЛАСТИВОСТІ КАТОДНОГО МАТЕРІАЛУ $LiMn_{0.7}Fe_{0.3}PO_4$ 19

ОРГАНІЧНА ХІМІЯ

Аліція Взорек, Таїзо Оно, Даніель Беккер, Вей Чжан, Хіроїкі Морівакі, Кунісуке Ізава, Хіройукі Конно, Вадим А. Солошонок
ЗАСТОСУВАННЯ D-АМІНОКИСЛОТ У ДИЗАЙНІ ЛІКАРСЬКИХ ЗАСОБІВ (огляд) 31

Contents

PHISICAL CHEMISTRY

O. Pasenko, Y. Osokin, A. Ivanchenko
ADSORPTION OF Pb^{2+} IONS BY HEMP HURD BIOCHAR FROM INDUSTRIAL HEMP (CANNABIS SATIVA). 17

ELECTROCHEMISTRY

O.V. Potapenko, H.V. Potapenko, V.O. Oliinyk, V.A. Sirosh, Changji Zhou, Chee Sien Wong, Changbo Yu, Chenchun Zhang
INFLUENCE OF THE NATURE OF A BINDER ON THE ELECTROCHEMICAL PROPERTIES OF THE $LiMn_{0.7}Fe_{0.3}PO_4$ CATHODE MATERIAL... 19

ORGANIC CHEMISTRY

Alicja Wzorek, Taizo Ono, Daniel Baecker, Wei Zhang, Hiroki Moriwaki, Kunisuke Izawa, Hiroyuki Konno, Vadim A. Soloshonok
APPLICATION OF D-AMINO ACIDS IN DRUG DESIGN (review) 31

УДК 544.723.2:546.3'131+628.394 doi: 10.33609/2708-129X.92.5.2026.3-18

АДСОРБЦІЯ ІОНІВ Pb^{2+} КОСТРИЦЕВИМ БІОВУГІЛЛЯМ ІЗ ТЕХНІЧНОЇ КОНОПЛІ (CANNABIS SATIVA)

О. О. Пасенко[1] https://orcid.org/0000-0003-3486-1864
Є. С. Осокін[2] * https://orcid.org/0000-0001-8894-0723
А. В. Іванченко[1] https://orcid.org/0000-0002-1404-7278

[1]*Дніпровський державний технічний університет,*
вул. Дніпробудівська, 2, Кам'янське 51900, Дніпропетровська область, Україна;
[2]*Інститут теоретичної фізики імені Боголюбова НАН України,*
вул. Метрологічна, 14-Б, Київ 03143, Україна
**e-mail: osokin@bitp.kyiv.ua*

Досліджено адсорбційні властивості трьох форм сорбентів на основі костриці технічної коноплі (*Cannabis sativa L.*) сорту «Гляниця» українського походження: необробленої (КН), частково обвугленої за 350 °С (КЧ) та повністю обвугленої за 550 °С (КБ, біовугілля) – щодо іонів Pb^{2+} із модельних розчинів. Параметри ізотерм Ленґмюра і Фрейндліха та моделі псевдо-другого порядку визначено нелінійним методом найменших квадратів. Модель Ленґмюра забезпечує фізично обґрунтований опис рівноважних даних завдяки наявності плато насичення; максимальна сорбційна ємність q_{max} зростає в ряду КН (103.1 мг/г) < КЧ (177.3 мг/г) < КБ (247.1 мг/г), наближаючись до показників комерційного активованого вугілля. Початкова швидкість сорбції h_0 збільшується у 5.7 разів від КН до КБ. Модель Вебера – Морріса виявила спільний вклад зовнішньої масопередачі та внутрішньочастинкової дифузії. Оптимальний *pH* 5.0–6.0; КБ найбільш стійке до конкуренції іонів Ca^{2+} та Mg^{2+}. Регенерація 0.1 М HNO_3 зберігає 90 % ємності КБ після п'яти циклів. Собівартість біовугілля у 8–17 разів нижча за комерційне активоване вугілля.

Ключові слова: адсорбція Pb^{2+}; біовугілля з *Cannabis sativa*; костриця технічної коноплі; ізотерма Ленгмюра; кінетика сорбції; очищення стічних вод.

ВСТУП. Забруднення водного середовища іонами важких металів є однією з найгостріших екологічних проблем в індустріальних регіонах України, зокрема для підприємств металообробної, акумуляторної та лакофарбової галузей. Свинець належить до пріоритетних токсикантів I класу небезпеки: гранично допустима концентрація Pb^{2+} у водоймах господарсько-питного призначення становить лише 0.03 мг/л, тоді як у виробничих стічних водах вона нерідко перевищує цей рівень у сотні разів.

Вплив іонів свинцю на живі організми проявляється у пригніченні ферментативних систем, порушенні кровотворення та накопиченні в кісткових тканинах, що зумовлює необхідність максимально повного вилучення Pb^{2+} із промислових скидів перед їхнім відведенням до природних водойм [1].

Традиційні методи очищення стічних вод від важких металів – хімічне осадження, іонообмінне розділення, мембранні процеси – забезпечують високий ступінь вилучення, однак потребують значних капітальних і експлуатаційних витрат. Це суттєво обмежує їхнє застосування на малих і середніх підприємствах, для яких актуальним є пошук ефективних і дешевих сорбційних матеріалів, здатних замінити комерційне активоване вугілля [2].

Перспективним джерелом сировини для виготовлення таких сорбентів є лігноцелюлозні агропромислові відходи. Целюлоза, геміцелюлози та лігнін за контрольованого термічного оброблення утворюють вуглецеві каркаси з розвиненою питомою поверхнею і високим вмістом кисневмісних функціональних груп [3]. Костриця конопель (*Cannabis sativa L.*) є побічним продуктом первинного перероблення стебел технічної коноплі, вихід якого становить 55–70 % маси сухого стебла. У зв'язку зі стрімким відновленням посівів технічної коноплі в Україні утворюються значні обсяги костричної маси, переважна частина якої наразі залишається невикористаною [10].

Аналіз останніх досліджень та публікацій. Сучасні дослідження у сфері сорбційного очищення води від важких металів фокусуються на переході від комерційного активованого вугілля до дешевих біосорбентів рослинного походження [2, 11]. Термічне оброблення лігноцелюлозної сировини в інтервалі 400–600 °C є оптимальною для формування мікропористої структури з розвиненою питомою поверхнею (300–700 $м^2/г$) і збереженням достатньої кількості поверхневих кисневмісних функціональних груп [3]. За температур понад 700 °C відбувається подальша графітизація вуглецевого каркаса, що супроводжується втратою активних центрів.

Систематичний огляд механізмів адсорбції важких металів на біосорбентах [4] виокремлює п'ять основних типів взаємодій: комплексоутворення з кисневмісними функціональними групами, іонний обмін, фізичну адсорбцію в порах, π-катіонні взаємодії з ароматичними фрагментами та поверхневе осадження. Кінетику сорбційних процесів у переважній більшості випадків описують моделлю псевдо-другого порядку Хо – Маккея [5], рівноважні дані – ізотермою Ленґмюра [6] або Фрейндліха [12], для опису дифузії – модель Вебера – Морріса [7].

Серед недавніх досліджень у праці [1] показано, що піроліз костриці за 500 °C забезпечує отримання біовугілля з максимальною сорбційною ємністю по Pb^{2+} на рівні 110–130 мг/г. У праці [9] застосовано гідротермальний синтез біочару зі стрижневої частини конопляного стебла, що дозволило досягти ємності близько 150 мг/г. У новіших дослідженнях ультразвук-асистована KOH-активація гідротермального біовугілля з конопляного стебла забезпечила ємність по Pb^{2+} до 345.8 мг/г [14], а порівняння температур піролізу та способів модифікації лігноцелюлозного біовугілля показало визначальну роль кисневмісних

груп і питомої поверхні у сорбції Pb^{2+} і Cd^{2+} [13]. Огляд [8] підкреслює, що ефективність біосорбентів суттєво залежить від географічного походження рослинної маси, що робить актуальним дослідження саме сорбентів із костриці конопель українського походження, систематичне порівняння необробленої та термічно модифікованої форм яких у літературі досі не представлено.

Постановка завдання. Мета дослідження – підвищення ефективності сорбційного вилучення іонів Pb^{2+} зі стічних вод шляхом застосування кострицевих сорбентів із технічної коноплі українського походження різного ступеня термічного обробления, встановлення параметрів рівноважних ізотерм і кінетики сорбції, визначення механізму адсорбції та оцінювання практичного потенціалу матеріалів для очищення промислових стоків.

ЕКСПЕРИМЕНТ І ОБГОВОРЕННЯ РЕЗУЛЬТАТІВ. Роботу проводили з кострицею технічної коноплі (*Cannabis sativa L.*) сорту «Гляниця», отриманою від переробного підприємства Полтавської області як побічний продукт первинного перероблення стебел. Вологість вихідної сировини становила 12.4 %, зольність – 2.8 %. Із вихідної сировини отримано три форми сорбентів: КН – необроблена костриця (вихідний матеріал); КЧ – частково обвуглена костриця (піроліз за 350 °С, 45 хв, закриті тиглі); КБ – повністю обвуглена костриця – біовугілля (піроліз за 550 °С, 75 хв, закриті тиглі). Всі три форми подрібнено до фракції 0.5–1.0 мм та висушено за 105 °С до постійної маси (табл. 1). Вибір температур 350 і 550 °С зумовлений потребою порівняти частково карбонізовану форму зі збереженими кисневмісними групами (350 °С) із повністю карбонізованим біовугіллям, отриманим у межах оптимального для лігноцелюлозної сировини інтервалу 400–600 °С [3, 13]; за температур понад 700 °С прогресуюча графітизація вуглецевого каркаса супроводжується втратою поверхневих активних центрів [3]. Жодних хімічних реагентів-активаторів на стадії піролізу не застосовували – усі три форми одержано винятково термічним обробленням без додаткової хімічної активації.

Табл. 1

Фізико-хімічні характеристики отриманих сорбентів

Table 1.

Physico-chemical characteristics of the obtained sorbents.

Характеристика	КН (необроблена)	КЧ (350 °С)	КБ (550 °С)
Вихід продукту, %	100	52.3 ± 1.4	29.7 ± 0.9
Вміст С, % (CHN)	47.2	62.8	81.4
Вміст Н, %	6.1	4.3	2.8
Вміст О, % (різниця)	44.1	30.6	13.9
pH водної суспензії	6.2 ± 0.1	6.0 ± 0.1	8.4 ± 0.2
$pH_{\text{ТНЗ}}$	5.8	6.1	7.9

Звертає на себе увагу різне співвідношення між точкою нульового заряду і *pH* водної суспензії для слабко модифікованих форм: для КН $pH_{ТНЗ}$ (5.8) нижчий за *pH* суспензії (6.2), тоді як для КЧ $pH_{ТНЗ}$ (6.1) дещо перевищує *pH* суспензії (6.0). Це свідчить про перерозподіл кислотно-основних поверхневих груп уже на стадії часткової карбонізації; для повністю карбонізованого біовугілля КБ обидва показники помітно зростають ($pH_{ТНЗ}$ 7.9; *pH* суспензії 8.4) внаслідок видалення кислих кисневмісних груп і збагачення поверхні основними центрами.

Сорбційні досліди проводили при *pH* 5.5 (ацетатний буфер), $T = 25 \pm 1$ °C, маса сорбенту 0.100 г, об'єм розчину 50.0 мл. Аналіз Pb^{2+} – ААС (λ = 217.0 нм), кожний дослід проводили у трьох паралельних зразках (табл. 2). Результати наведено як середнє арифметичне трьох паралельних визначень. Стандартне відхилення сорбційної ємності (табл. 3) розраховували за вибіркою з $n = 3$; для параметрів ізотерм q_{max}, K_L, K_F і $1/n$ (табл. 4) наведено 95 % довірчі інтервали, обчислені за розподілом Стьюдента ($n = 3$) за трьома незалежними паралельними апроксимаціями (SigmaPlot 15.0).

Результати рівноважних сорбційних дослідів для трьох форм сорбенту наведено в табл. 3.

Табл. 2

Умови проведення сорбційних дослідів

Table 2.

Conditions for conducting sorption experiments.

Параметр	**Значення**
Метал-модель	Pb^{2+} ($Pb(NO_3)_2$ «ч.д.а.»)
pH досліду	5.5 (ацетатний буфер)
Температура	25 ± 1 °C
Маса сорбенту	0.100 ± 0.001 г
Об'єм розчину	50.0 мл
Концентрації C_0 (ізотерма)	10; 25; 50; 100; 200; 400; 600 мг/л
Час контакту (ізотерма)	180 хв
C_0 для кінетики	100 мг/л
Метод аналізу	ААС полум'яна (λ = 217.0 нм)
Кількість паралелей	3

Табл. 3

Рівноважні дані сорбції Pb^{2+} на трьох формах кострицевих сорбентів (*pH* = 5.5; *T* = 25 °C; *m* = 0.100 г; *V* = 50 мл; *n* = 3; значення *q* наведено як середнє ± стандартне відхилення)

Table 3.

Equilibrium data of Pb^{2+} sorption on three forms of hemp hurd sorbents. (*pH* = 5.5; *T* = 25 °C; *m* = 0.100 g; *V* = 50 ml; *n* = 3; *q* values are given as mean ± standard deviation).

C_0, мг/л	C_e(КН), мг/л	q(КН), мг/г	R(КН), %	C_e(КЧ), мг/л	q(КЧ), мг/г	R(КЧ), %	C_e(КБ), мг/л	q(КБ), мг/г	R(КБ), %
10	2.1	3.94 ± 0.04	79.0	0.8	4.62 ± 0.02	92.0	0.2	4.91 ± 0.03	98.0
25	7.3	8.84 ± 0.03	70.8	2.6	11.17 ± 0.04	89.6	0.9	12.07 ± 0.08	96.4
50	18.6	15.71 ± 0.02	62.8	8.1	20.95 ± 0.05	83.8	2.8	23.60 ± 0.03	94.4
100	47.2	26.41 ± 0.03	52.8	22.4	38.80 ± 0.02	77.6	9.3	45.35 ± 0.02	90.7
200	113.5	43.25 ± 0.02	43.3	67.3	66.35 ± 0.02	66.3	31.4	84.32 ± 0.02	84.3
400	268.4	65.82 ± 0.02	32.9	180.2	109.91 ± 0.02	54.9	98.6	150.70 ± 0.02	75.3
600	439.1	80.45 ± 0.01	26.8	320.5	139.75 ± 0.02	46.6	201.2	199.40 ± 0.01	66.5

Апроксимація ізотермами Ленґмюра і Фрейндліха. Для кількісного опису рівноважних даних та встановлення механізму взаємодії іонів Pb^{2+} із поверхнею кострицевих сорбентів експериментальні ізотерми апроксимовано класичними моделями Ленґмюра [6] і Фрейндліха [12]. Модель Ленґмюра передбачає моношарову адсорбцію на енергетично однорідних активних центрах з обмеженою ємністю насичення q_{max}, тоді як модель Фрейндліха описує адсорбцію на енергетично неоднорідній поверхні без чіткого плато. Параметри обох моделей визначено нелінійним методом найменших квадратів (SigmaPlot 15.0) і зведено у табл. 4. Рівняння нелінійних форм моделей Ленґмюра (1) і Фрейндліха (2) мають вигляд:

$$q_e = q_{max} K_L C_e / (1 + K_L C_e) \quad (1)$$

$$q_e = K_F \cdot C_e^{1/n} \ . \quad (2)$$

Табл. 4

Параметри ізотерм Ленґмюра і Фрейндліха для сорбції Pb^{2+} (q_{max}, K_L, K_F, $1/n$ – середнє ± 95 % довірчий інтервал, n = 3)

Table 4.

The parameters of Langmuir and Freundlich isotherms for Pb^{2+} sorption (q_{max}, K_L, K_F, $1/n$ – mean ± 95% confidence interval, n = 3).

Сорбент	q_{max}, мг/г	K_L, л/мг	R_L (при C_0 = 100)	R^2 (Ленґмюр)	K_F	$1/n$	R^2 (Фрейндліх)
КН	103.1 ± 3.5	0.00704 ± 0.00010	0.353	0.990	3.76 ± 0.01	0.507 ± 0.001	0.997
КЧ	177.3 ± 1.9	0.01021 ± 0.00008	0.240	0.987	8.06 ± 0.02	0.497 ± 0.001	0.998
КБ	247.1 ± 0.5	0.01793 ± 0.00029	0.146	0.987	15.88 ± 0.16	0.481 ± 0.002	0.998

Графічне зображення апроксимації рівноважних даних моделлю Ленґмюра наведено на рис. 1. Усі три криві мають класичну форму ізотерм I типу: круте зростання сорбційної ємності в області низьких рівноважних концентрацій з поступовим виходом на насичення при C_e > 200 мг/дм^3. Послідовне зростання нахилу початкової ділянки в ряду КН → КЧ → КБ свідчить про підвищення спорідненості поверхні сорбенту до іонів Pb^{2+} зі збільшенням ступеня термічного оброблення, що корелює з підвищенням константи Ленґмюра K_L від 0.00704 до 0.0179 л/мг (табл. 4). Максимальна сорбційна ємність q_{max} зростає в ряду КН (103.1 мг/г) < КЧ (177.3 мг/г) < КБ (247.1 мг/г), що відображає послідовне збільшення кількості активних центрів та розвиненості пористої структури. Значення безрозмірного фактора Ленґмюра R_L для всіх трьох форм перебуває в інтервалі $0 < R_L < 1$, що підтверджує сприятливий характер процесу адсорбції [6]. Зниження R_L у ряду КН (0.353) → КЧ (0.240) → КБ (0.146) додатково підтверджує підвищення спорідненості поверхні до Pb^{2+} зі збільшенням ступеня обвуглення сировини.

Апроксимацію тих самих експериментальних даних моделлю Фрейндліха наведено на рис. 2. На відміну від Ленґмюра, криві Фрейндліха не виходять на плато і продовжують монотонно зростати у всьому діапазоні концентрацій, що є наслідком степеневої природи рівняння $q_e = K_F \cdot C_e^{1/n}$. За низьких та середніх рівноважних концентрацій (C_e < 100 мг/дм^3) обидві моделі описують експериментальні дані з порівнянною точністю. Однак за високих концентрацій модель Фрейндліха систематично завищує розрахункові значення q_e – особливо для форми КБ, де прогнозоване значення при C_e = 500 мг/дм^3 сягає ~315 мг/г, тоді як модель Ленґмюра дає фізично обґрунтоване значення ~223 мг/г, близьке до експериментального плато.

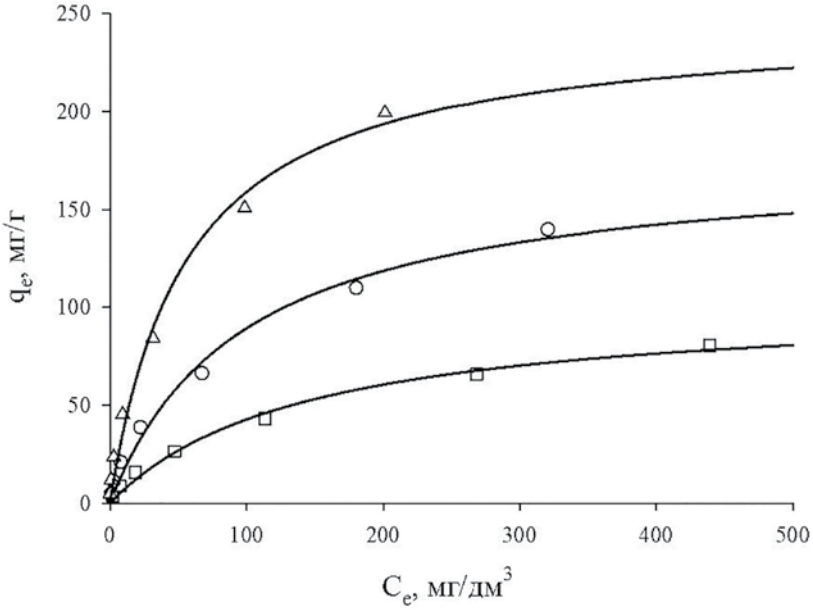

Рис. 1. Ізотерми адсорбції Pb^{2+} на кострицевих сорбентах: апроксимація моделлю Ленґмюра (*pH* 5.5; *T* = 25 °C). □ КН; ○ КЧ; △ КБ
Fig. 1. Adsorption isotherms of Pb^{2+} on hemp hurd sorbents: Langmuir model fit (*pH* 5.5; *T* = 25 °C). □ US; ○ PC; △ BC.

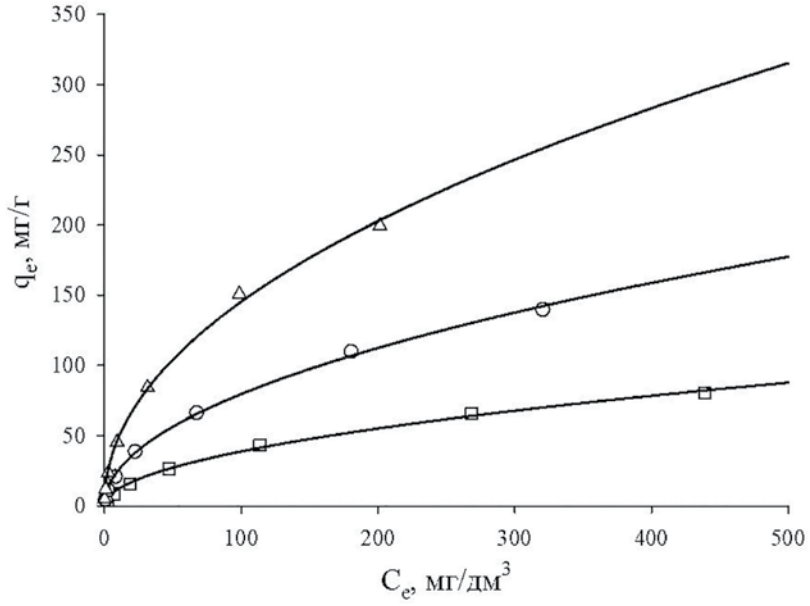

Рис. 2. Ізотерми адсорбції Pb^{2+} на кострицевих сорбентах: апроксимація моделлю Фрейндліха (*pH* 5,5; *T* = 25 °C). □ КН; ○ КЧ; △ КБ
Fig. 2 Adsorption isotherms of Pb^{2+} on hemp hurd sorbents: Freundlich model fit (*pH* 5.5; *T* = 25 °C). □ US; ○ PC; △ BC.

Формальне порівняння коефіцієнтів детермінації (табл. 4) показує, що обидві моделі забезпечують високу якість апроксимації (R^2 > 0.987 для обох). Проте вибір оптимальної моделі не може ґрунтуватися виключно на числових критеріях. Ключовим аргументом на користь моделі Ленґмюра є її фізична обґрунтованість: наявність плато насичення відповідає реальній поведінці сорбентів з обмеженою кількістю активних центрів, тоді як необмежене зростання ємності за Фрейндліхом при $C_e \to \infty$ не має фізичного сенсу для реальних сорбційних систем. Отримане для біовугілля КБ значення q_{max} = 247.1 мг/г перевищує більшість літературних аналогів біочару з агровідходів (88–150 мг/г) [11] і узгоджується з рівнем сучасних конопляних біовуглецiв [14], наближаючись до показників комерційного активованого вугілля (200–350 мг/г), що підтверджує конкурентоспроможність розробленого матеріалу.

Кінетика сорбції Pb^{2+} на кострицевих сорбентах. Для встановлення швидкісних характеристик процесу проведено кінетичні дослідження (C_0 = 100 мг/дм^3; *pH* 5,5; T = 25 °C). Кінетичні дані апроксимовано моделлю псевдо-другого порядку (ПДП) Хо – Маккея [5]. Лінеаризовану форму рівняння ПДП (3) та початкову швидкість сорбції h_0 (4) надано рівняннями:

$$t/q_t = 1 / (k_2 \cdot q_e^{\,2}) + t/q_e \qquad (3)$$

$$h_0 = k_2 \cdot q_e^{\,2} \ . \qquad (4)$$

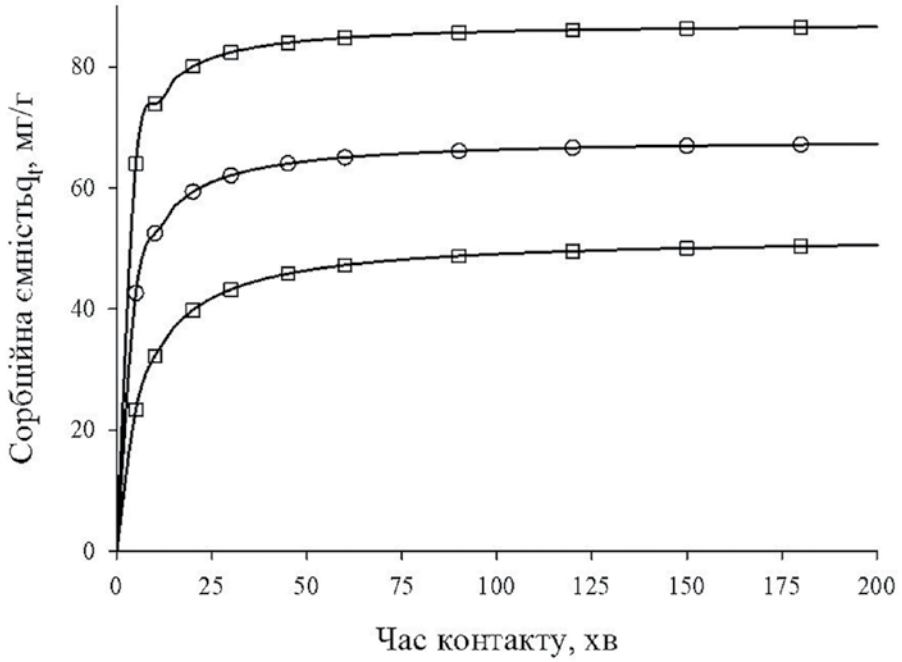

Рис. 3. Кінетика адсорбції Pb^{2+} на кострицевих сорбентах: апроксимація моделлю ПДП (C_0 = 100 мг/дм^3; *pH* 5,5; T = 25 °C). □ КН; ○ КЧ; △ КБ
Fig. 3. Kinetics of Pb^{2+} adsorption on hemp hurd sorbents: pseudo-second-order model fit (C_0 = 100 mg/L; *pH* 5.5; T = 25 °C). □ US; ○ PC; △ BC.

Кінетичні криві сорбції Pb^{2+} для трьох форм сорбенту наведено на рис. 3. Усі три залежності демонструють характерну двофазну поведінку: інтенсивне поглинання іонів свинцю в перші 30 хв контакту, протягом яких реалізується від 55 до 60 % загальної сорбційної ємності з подальшим уповільненням процесу та виходом на рівноважне плато в інтервалі 120–150 хв. Така динаміка пояснюється послідовною зміною лімітуючої стадії: на початковому етапі процес контролюється масопередачею до високодоступних поверхневих центрів, тоді як на завершальному – внутрішньочастинковою дифузією іонів Pb^{2+} у мікропористій структурі вуглецевого каркаса. Нахил початкової ділянки кривих суттєво зростає в ряду КН → КЧ → КБ, що відображає збільшення початкової швидкості сорбції. Теоретичні криві моделі ПДП, розраховані нелінійним методом найменших квадратів (SigmaPlot 15.0), адекватно описують експериментальні дані у всьому часовому інтервалі.

Модель забезпечує відмінну апроксимацію для всіх трьох форм сорбенту з коефіцієнтом детермінації $R^2 = 0.993–0.999$ і збігом розрахованого та дослідного q_e в межах $\Delta < 3.5$ %, що однозначно вказує на хемосорбцію як лімітуючу стадію процесу [5] (рис. 3). Початкова швидкість сорбції $h_0 = k_2 \cdot q_e^2$ зростає у 5.7 разів від необробленої кострицi (8.47 мг·г$^{-1}$·хв$^{-1}$) до біовугілля КБ (47.98 мг·г$^{-1}$·хв$^{-1}$), що має важливе практичне значення для проєктування швидкодіючих систем очищення стічних вод з обмеженим часом контакту, де ключовим параметром є саме початкова продуктивність сорбенту.

Табл. 5

Параметри моделі псевдо-другого порядку для сорбції Pb^{2+}

Table 5.

Parameters of the pseudo-second-order model for Pb^{2+} sorption.

Сорбент	k_2, г·мг$^{-1}$·хв$^{-1}$	q_e(розрах.), мг/г	q_e(експерт.), мг/г	Δq_e, %	R^2	Початкова швидкість h_0, мг·г$^{-1}$·хв$^{-1}$
КН	0.00312	52.1	50.4	3.4	0.998	8.47
КЧ	0.00487	68.3	66.0	3.5	0.999	22.72
КБ	0.00628	87.4	85.2	2.6	0.999	47.97

Для додаткової верифікації результатів нелінійної регресії кінетичні дані подано у лінеаризованих координатах $t/q_t - t$ (рис. 4). Лінеаризована форма моделі ПДП $t/q_t = t/q_e + 1/(k_2 \cdot q_e^2)$ дозволяє незалежно визначити параметри з нахилу і відрізку прямої. Експериментальні точки для всіх трьох сорбентів формують чіткі лінійні залежності з $R^2 = 0.997–1.000$, що підтверджує коректність обраної моделі. Значення q_e, визначені з лінеаризації (64.1; 81.3; 103.3 мг/г), дещо перевищують результати нелінійного фіту (52.1; 68.3; 87.4 мг/г), що є відомою особливістю лінеаризованого методу, який надає більшої ваги точкам за великих значень t [5].

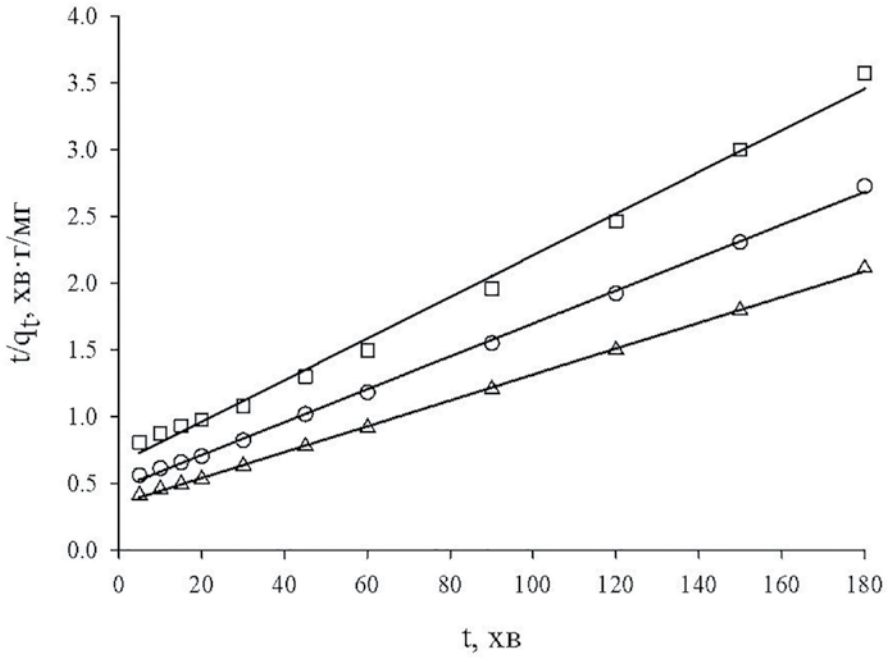

Рис. 4. Лінеаризація моделі псевдо-другого порядку: t/q_t – t. □ КН; ○ КЧ; △ КБ
Fig. 4. Linearization of pseudo-second-order model: t/q_t vs t. □ US; ○ PC; △ BC.

Модель внутрішньочастинкової дифузії Вебера – Морріса. Для виявлення дифузійного вкладу в загальну швидкість процесу кінетичні дані оброблено за моделлю Вебера – Морріса у координатах q_t – $t^{1/2}$ за рівнянням (5):

$$q_t = k_{id} \cdot t^{1/2} + C \,. \qquad (5)$$

Залежності на рис. 5 для всіх трьох форм сорбенту чітко розділяються на два лінійні сегменти. Перший сегмент із більшим нахилом k_{id1} відповідає стадії швидкої сорбції на легкодоступних поверхневих активних центрах, контрольованій переважно зовнішньою масопередачею з об'єму розчину до поверхні частинок. Другий сегмент із меншим нахилом k_{id2} відображає повільнішу внутрішньочастинкову дифузію іонів Pb^{2+} у мікропористій структурі вуглецевого каркаса аж до встановлення сорбційної рівноваги.

Принципово важливо, що жодна з прямих не проходить через початок координат – наявність ненульового відрізка C на осі q_t свідчить про те, що внутрішньочастинкова дифузія не є єдиною лімітуючою стадією процесу, а зовнішня масопередача також робить помітний вклад у загальну кінетику [7]. Зростання відрізка C від 7.4 (КН) до 17.6 (КБ) корелює зі зростанням розвиненості мікропористої структури біовугілля, що підтверджується незалежними даними CHN-аналізу.

Оптимальний інтервал pH для всіх форм становить 5.0–6.0: поверхня несе від'ємний заряд ($pH > pH_{\text{ТНЗ}}$), що сприяє електростатичному притяганню Pb^{2+}. При $pH < 4$ зростає конкуренція протонів; при $pH > 7$ починається гідроліз $Pb(OH)_2$.

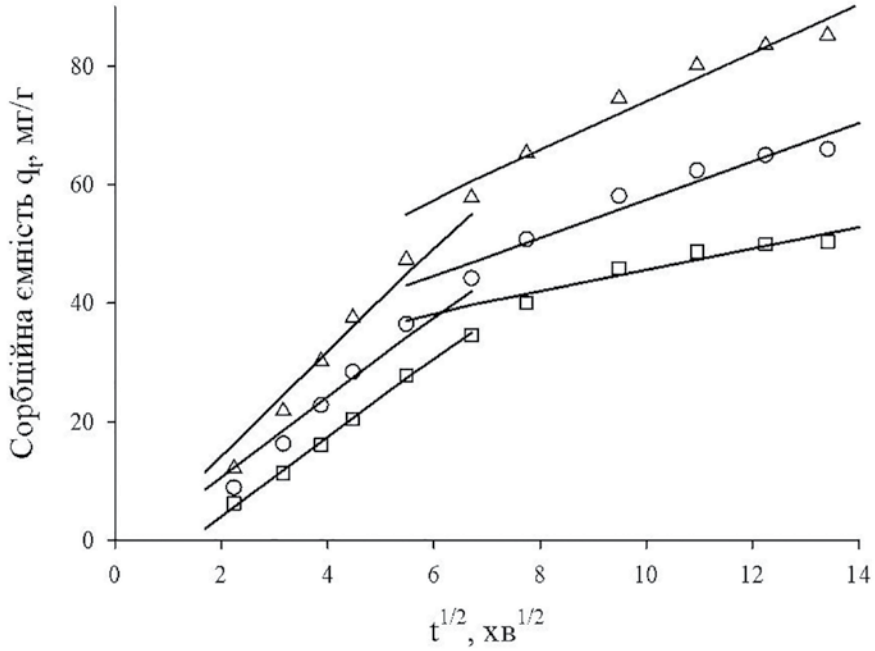

Рис. 5. Модель Вебера – Морріса: q_t – $t^{1/2}$ (C_0 = 100 мг/дм^3; *pH* 5,5; *T* = 25 °C). □ КН; ○ КЧ; △ КБ
Fig. 5. Weber-Morris model: q_t vs $t^{1/2}$ (C_0 = 100 mg/L; *pH* 5.5; *T* = 25 °C). □ US; ○ PC; △ BC.

Було показано конкуруючий вплив іонів Ca^{2+} та Mg^{2+}. За присутності цих іонів (50 мг/дм^3) зниження ємності для КН – 18–22 %, для КЧ – 12–15 %, для КБ – лише 8–10 %. Більша стійкість КБ може бути зумовлена ймовірним переважанням π-катіонних взаємодій з ароматичними фрагментами карбонізованого каркаса, які менш чутливі до конкуренції двовалентних катіонів; це припущення потребує підтвердження прямими спектральними методами.

Регенерація відпрацьованих сорбентів. Можливість багаторазового використання сорбенту є одним із ключових критеріїв його практичної придатності. Регенерацію відпрацьованих кострицевих сорбентів проводили шляхом оброблення 0.1 М розчином нітратної кислоти за кімнатної температури упродовж 60 хв із подальшим відмиванням дистильованою водою до нейтральної реакції. Вибір саме нітратної кислоти зумовлений тим, що протонування поверхневих кисневмісних груп у кислому середовищі витісняє іони Pb^{2+} з активних центрів, а нітрат-іон утримує свинець у розчині завдяки високій розчинності $Pb(NO_3)_2$ і не утворює малорозчинних осадів (на відміну від сульфатної чи хлоридної кислот, що здатні давати $PbSO_4$ або малорозчинні хлоридні форми); крім цього, нітрат-аніон збігається з протиіоном вихідного модельного розчину $Pb(NO_3)_2$, що виключає внесення стороннього аніона. Подібний регенераційний підхід із застосуванням розведеної HNO_3 описано для лігноцелюлозного біовугілля [13]. Динаміку зміни сорбційної ємності протягом п'яти послідовних циклів сорбції – десорбції наведено на рис. 6.

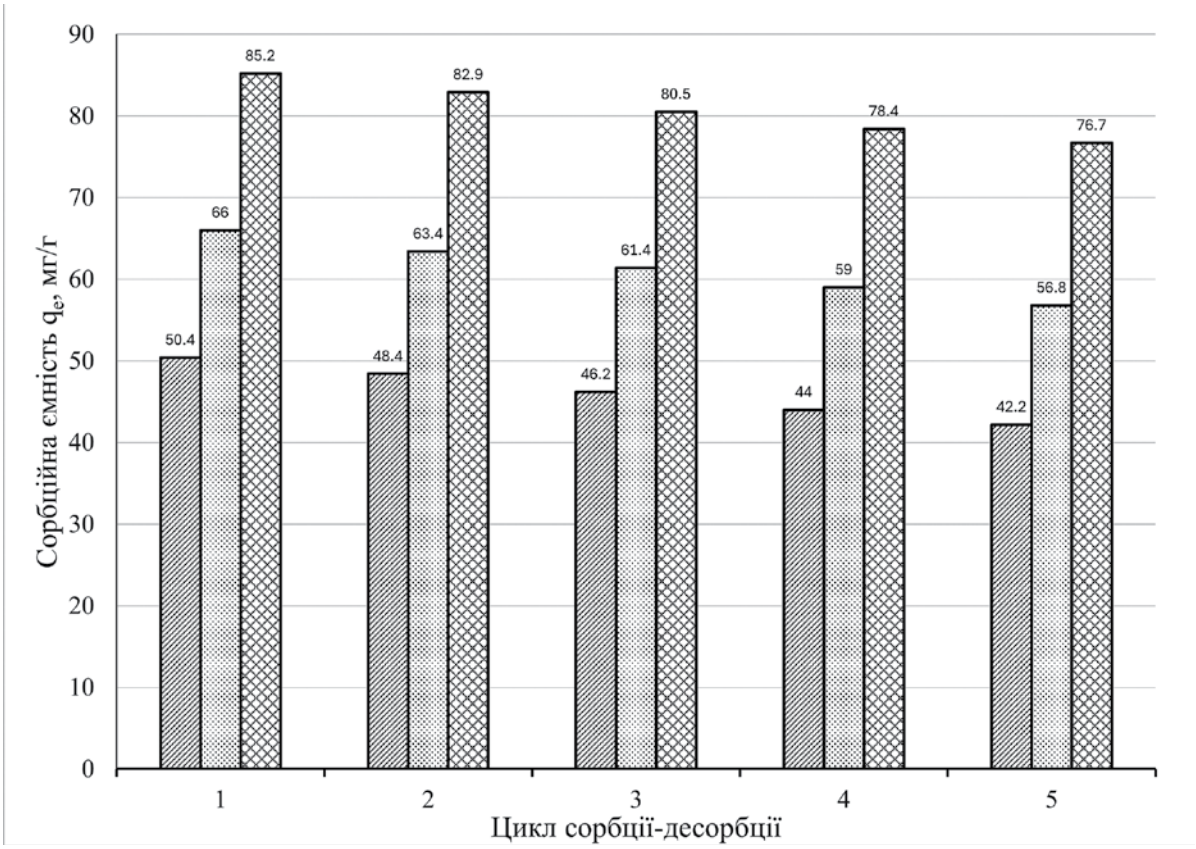

Рис. 6. Зміна сорбційної ємності протягом 5 циклів сорбції – десорбції (0.1 М HNO_3)
Fig. 6. Sorption capacity over 5 sorption-desorption cycles (0.1 M HNO_3).

Ступінь десорбції Pb^{2+} для біовугілля КБ знижується від ~92 % у першому циклі до ~86 % у п'ятому, залишаючись у межах 86–92 %. Збереження сорбційної ємності після п'яти циклів становить ~90 % для КБ, ~86 % для КЧ і ~84 % для КН відносно початкових значень. Вища стійкість біовугілля КБ до циклічної регенерації, ймовірно, пов'язана з переважанням π-катіонних взаємодій та фізичної адсорбції в мікропорах, які є більш оборотними порівняно з комплексоутворенням через функціональні групи –COOH і –OH, характерним для необробленої кострици КН. Поступове зниження ємності з кожним циклом зумовлено частковим руйнуванням активних центрів під дією кислотного середовища та незворотним зв'язуванням частини іонів свинцю у важкодоступних мікропорах.

Порівняльна оцінка. Орієнтовну економічну привабливість матеріалу оцінювали за відносною собівартістю, нормованою на вартість вихідної сировини (умовна одиниця – питома вартість 1 кг кострици). За такого нормування відносна собівартість кострицевого біовугілля становить ~1.8 (з урахуванням виходу 29.7 % і енерговитрат піролізу при 550 °C), тоді як для комерційного активованого вугілля аналогічний показник, за літературними даними, пе-

ISSN 2708-129X. Укр. хім. журн., 2026

ребуває в межах 15–30 [2, 15], тобто собівартість біовугілля приблизно у 8–17 разів нижча. Наведена оцінка є попередньою і ґрунтується на порівнянні сировинної та енергетичної складових; вона не враховує повний життєвий цикл та ресурс роботи комерційного сорбенту, тому потребує уточнення за результатами техніко-економічного розрахунку. При q_{max} = 247.1 мг/г (діапазон АВ: 200–350 мг/г) та збереженні ~90 % ємності після п'яти циклів регенерації біовугілля КБ є потенційно привабливою низьковартісною альтернативою, остаточна конкурентоспроможність якої потребує підтвердження порівняльними кінетичними та ресурсними випробуваннями з комерційним АВ.

Обмеження дослідження. Текстурні характеристики сорбентів (питома поверхня за БЕТ, розподіл пор) і поверхневі функціональні групи (ІЧ-/Раман-спектроскопія) у межах цієї роботи інструментально не визначали; їх оцінювали опосередковано – за даними елементного CHN-аналізу, виходу продукту та параметрів кінетичних моделей. Тому твердження про розвинену мікропористу структуру та запропоновані механізми адсорбції (π-катіонні взаємодії, комплексоутворення з групами –COOH і –OH) слід розглядати як узгоджені з літературою [3, 4, 13] гіпотези, що потребують підтвердження прямими структурними та спектральними методами. Термогравіметричний аналіз вихідної сировини також не виконували. Пряме інструментальне визначення текстурних і спектральних характеристик, а також порівняльні кінетичні й ресурсні випробування з комерційним активованим вугіллям становлять основні напрями подальших досліджень.

ВИСНОВКИ. Уперше системно досліджено адсорбційні властивості трьох форм кострицевих сорбентів *з Cannabis sativa L.* сорту «Гляниця». Контрольоване термічне оброблення (350–550 °C) забезпечує конкурентоспроможний сорбент без дорогих активуючих реагентів.

Рівноважні дані найкраще описують ізотермою Ленґмюра: q_{max} зростає від 103.1 (КН) до 247.1 мг/г (КБ), що перевищує більшість літературних аналогів [11] і наближається до комерційного АВ.

Кінетика підпорядковується моделі ПДП Хо – Маккея (R^2 = 0.993–0.999). Початкова швидкість h_0 зростає у 5.7 разів від 8.47 до 47.98 мг·г$^{-1}$·хв$^{-1}$. Модель Вебера – Морріса виявила спільний вклад зовнішньої масопередачі та дифузії в порах [7].

Оптимальний *pH* 5.0–6.0. Біовугілля КБ найбільш стійке до конкуренції Ca^{2+}/Mg^{2+} (зниження ємності лише 8–10 %).

Регенерація 0.1 М HNO_3 забезпечує 86–92 % десорбції для КБ зі збереженням 90 % ємності після 5 циклів. Собівартість у 8–17 разів нижча за комерційне АВ.

ВКЛАД АВТОРІВ:

А. В. Іванченко – постановка завдання дослідження, аналіз отриманих даних;

О. О. Пасенко – проведення експериментальних робіт;

Є. С. Осокін – оброблення результатів експериментів.

Автори брали участь у підготовці, редагуванні та доопрацюванні статті. Усі автори ознайомилися з результатами дослідження та схвалили остаточну версію статті.

КОНФЛІКТ ІНТЕРЕСІВ. Автори заявляють про відсутність конфлікту інтересів.

ФІНАНСУВАННЯ. Роботу виконано в рамках науково-дослідної роботи кафедри хімічних та біологічних технологій Дніпровського державного технічного університету «Одержання хімічно модифікованих сорбентів із вторинної сировини» (01.09.2024–31.08.2026), № ДР 0124U004316.

ADSORPTION OF Pb^{2+} IONS BY HEMP HURD BIOCHAR FROM INDUSTRIAL HEMP (CANNABIS SATIVA).

O. Pasenko[a], Y. Osokin[b], A. Ivanchenko[a]

[a]Dniprovsky State Technical University, Dniprobudivska str., 51900 Kamianske, Ukraine;
*[b]Bogolyubov Institute for Theoretical Physics, 4-B Metrolohichna str., 03143Kyiv, Ukraine, *e-mail: osokin@bitp.kyiv.ua*

The adsorption properties of three sorbent forms derived from industrial hemp hurd (*Cannabis sativa L.*, 'Glianytsia' variety, Poltava region, Ukraine) untreated (US), partially carbonized at 350 °C for 45 min (PC) and fully carbonized biochar at 550 °C for 75 min (BC) were studied for Pb^{2+} removal from model aqueous solutions. Equilibrium data were described by the Langmuir and Freundlich models with parameters determined by nonlinear least-squares regression (SigmaPlot 15.0). The Langmuir model provided a physically sound description due to its saturation plateau corresponding to the finite number of active sites; the maximum sorption capacity q_{max} increased as US (103.1 mg/g) < PC (177.3 mg/g) < BC (247.1 mg/g), approaching commercial activated carbon (200–350 mg/g). Although the Freundlich model yielded comparable R^2 values, it overestimated q_e at high equilibrium concentrations, confirming the Langmuir preference on the basis of physical adequacy. Sorption kinetics followed the Ho–McKay pseudo-second-order model (R^2 = 0.993–0.999), confirming chemisorption as the rate-limiting step. The initial sorption rate h_0 increased 5.7-fold from US (8.47 mg · g^{-1} · min^{-1}) to BC (47.98 mg · g^{-1} · min^{-1}). Weber-Morris analysis revealed two linear segments with non-zero intercepts, indicating combined contributions of external mass transfer and pore diffusion. Optimum *pH* was 5.0-6.0; BC showed the highest resistance to Ca^{2+}/Mg^{2+} competition (capacity loss only 8–10 %). Regeneration with 0.1 M HNO_3 retained 90 % of BC capacity after five sorption-desorption cycles. The estimated production cost is 8–17 times lower than commercial activated carbon, making hemp hurd biochar an economically attractive alternative for Pb^{2+} removal from industrial wastewater.

Keywords: Pb^{2+} adsorption; Cannabis sativa biochar; hemp hurd; Langmuir isotherm; sorption kinetics; wastewater treatment.

ЛІТЕРАТУРА

1. Puglia M. et al. Assessment of hemp hurd-derived biochar. *Heliyon*. 2023. **9**. P. e14698. doi: 10.1016/j.heliyon.2023.e14698
2. Wang J., Wang S. Preparation, modification and environmental application of biochar: A review. Journal of Cleaner Production. 2019. **227**. P. 1002–1022. doi: 10.1016/j.jclepro.2019.04.282

3. Tan X. et al. Application of biochar for removal of pollutants. *Chemosphere*. 2015. **125**. P. 70–85.
doi: 10.1016/j.chemosphere.2014.12.058
4. Raji Z. et al. Adsorption of heavy metals: mechanisms, kinetics. *Waste*. 2023. **1**(3). P. 775–805.
doi: 10.3390/waste1030046
5. Ho Y. S., McKay G. Pseudo-second order model. *Process Biochem.* 1999. **34**(5). P. 451–465.
doi: 10.1016/S0032-9592(98)00112-5
6. Langmuir I. Adsorption of gases on plane surfaces. *J. Am. Chem. Soc.* 1918. **40**(9). P. 1361–1403.
doi: 10.1021/ja02242a004
7. Weber W. J., Morris J. C. Kinetics of adsorption on carbon. *J. Sanit. Eng. Div. ASCE*. 1963. **89**(2). P. 31–60.
8. Demirbas A. Heavy metal adsorption onto agro-based waste materials. *J. Hazard. Mater.* 2008. **157**. P. 220–229.
doi: 10.1016/j.jhazmat.2008.01.024
9. Zhang Z. et al. Single-step hydrothermal synthesis of biochar from hemp stalk core. *Sustain. Chem. Pharm.* 2023. **36**. P.101316.
doi: 10.1016/j.scp.2023.101316
10. Amaducci S. et al. Key cultivation techniques for hemp. *Ind. Crops Prod.* 2015. **68**. P. 2–16.
doi: 10.1016/j.indcrop.2014.06.041
11. Patra, J. M., Panda, S. S., & Dhal, N. K. Biochar as a low-cost adsorbent for heavy metal removal: A review. *Int. J. Res. Biosci*. 2017. **6**(1). P. 1–7.
12. Freundlich H. Über die Adsorption in Lösungen. *Z. Phys. Chem.* 1907. **57**. P. 385–470.
doi: 10.1515/zpch-1907-5723
13. Huang Z., Wang Q., Zhang Y., Du B., Zhou J., Ji D. Effects of pyrolysis temperatures and modified methods on rice husk-derived biochar characteristics and heavy metal adsorption. *Molecules*. 2025. **30**(17). P. 3616.
https://doi.org/10.3390/molecules30173616
14. Liu L., Yu W., Zhang Z., Li Q., Peng C., Wu K., Liu D., He S., Liu N., Li X. Ultrasonic-assisted K^+ modification of industrial hemp stalk hydrothermal biochar for highly effective adsorption of Pb^{2+}. *Materials*. 2025. **18**(10). P. 2348.
https://doi.org/10.3390/ma18102348
15. Bassareh H., Karamzadeh M., Movahedirad S. Synthesis and characterization of cost-effective and high-efficiency biochar for the adsorption of Pb^{2+} from wastewater. *Sci. Rep.* 2023. **13**. P. 15608.
https://doi.org/10.1038/s41598-023-42918-0

REFERENCES

1. Puglia M. et al. Assessment of hemp hurd-derived biochar. *Heliyon*. 2023. **9**: e14698.
doi: 10.1016/j.heliyon.2023.e14698
2. Wang J., Wang S. Preparation, modification and environmental application of biochar: A review. Journal of Cleaner Production. 2019. **227**: 1002–1022.
doi: 10.1016/j.jclepro.2019.04.282
3. Tan X. et al. Application of biochar for removal of pollutants. *Chemosphere*. 2015. **125**: 70–85.
doi: 10.1016/j.chemosphere.2014.12.058
4. Raji Z. et al. Adsorption of heavy metals: mechanisms, kinetics. *Waste*. 2023. **1**(3): 775–805.
doi: 10.3390/waste1030046
5. Ho Y. S., McKay G. Pseudo-second order model. *Process Biochem.* 1999. **34**(5): 451–465.
doi: 10.1016/S0032-9592(98)00112-5
6. Langmuir I. Adsorption of gases on plane surfaces. *J. Am. Chem. Soc.* 1918. **40**(9): 1361–1403.
doi: 10.1021/ja02242a004
7. Weber W. J., Morris J. C. Kinetics of adsorption on carbon. *J. Sanit. Eng. Div. ASCE*. 1963. **89**(2): 31–60.
8. Demirbas A. Heavy metal adsorption onto agro-based waste materials. *J. Hazard. Mater.* 2008. **157**: 220–229.
doi: 10.1016/j.jhazmat.2008.01.024
9. Zhang Z. et al. Single-step hydrothermal

synthesis of biochar from hemp stalk core. *Sustain. Chem. Pharm*. 2023. **36**: 101316. doi: 10.1016/j.scp.2023.101316
10. Amaducci S. et al. Key cultivation techniques for hemp. *Ind. Crops Prod.* 2015. **68**: 2–16. doi: 10.1016/j.indcrop.2014.06.041
11. Patra, J. M., Panda, S. S., & Dhal, N. K. Biochar as a low-cost adsorbent for heavy metal removal: A review. *Int. J. Res. Biosci*. 2017. **6**(1): 1–7.
12. Freundlich H. Über die Adsorption in Lösungen. *Z. Phys. Chem.* 1907. **57**: 385–470. doi: 10.1515/zpch-1907-5723
13. Huang Z., Wang Q., Zhang Y., Du B., Zhou J., Ji D. Effects of pyrolysis temperatures and modified methods on rice husk-derived biochar characteristics and heavy metal adsorption. *Molecules*. 2025. **30**(17): 3616. https://doi.org/10.3390/molecules30173616
14. Liu L., Yu W., Zhang Z., Li Q., Peng C., Wu K., Liu D., He S., Liu N., Li X. Ultrasonic-assisted K^+ modification of industrial hemp stalk hydrothermal biochar for highly effective adsorption of Pb^{2+}. *Materials*. 2025. **18**(10): 2348. https://doi.org/10.3390/ma18102348
15. Bassareh H., Karamzadeh M., Movahedirad S. Synthesis and characterization of cost-effective and high-efficiency biochar for the adsorption of Pb^{2+} from wastewater. *Sci. Rep.* 2023. **13**: 15608. https://doi.org/10.1038/s41598-023-42918-0

Стаття надійшла: 28.04.2026.
Статтю прийнято до друку: 10.05.2026.
Статтю опубліковано: 25.06.2026.

UDC: 542.8+544.6 doi: 10.33609/2708-129X.92.5.2026.19-30

INFLUENCE OF THE NATURE OF A BINDER ON THE ELECTROCHEMICAL PROPERTIES OF THE $LiMn_{0.7}Fe_{0.3}PO_4$ CATHODE MATERIAL

O.V. Potapenko[1] https://orcid.org/0000-0002-0169-2403
H.V. Potapenko[1,2] https://orcid.org/0000-0002-1071-0183
V.O. Oliinyk[1] https://orcid.org/0000-0002-0929-8662
V.A. Sirosh[1] https://orcid.org/0000-0001-9620-8073
Changji Zhou[2] https://orcid.org/0009-0006-2539-0692
Chee Sien Wong [2,3] https://orcid.org/0000-0003-4504-3664
Changbo Yu[2] https://orcid.org/0009-0001-1912-9766
Chenchun Zhang[2] https://orcid.org/0009-0009-2203-0503

[1]V.I. Vernadsky Institute of General and Inorganic Chemistry of the National Academy of Sciences of Ukraine, 32/34 Acad. Palladina Ave., 03142 Kyiv, Ukraine;
[2]Zhejiang Casnovo New Materials Co., Ltd., No.1 Zhongke Road, Zhanmao Street, Putuo District, Zhoushan City, Zhejiang Province, China;
[3]School of Petrochemical Engineering and Environment, Zhejiang Ocean University, No. 1, Haida South Road, Lincheng Street, Dinghai District, Zhoushan City, Zhejiang Province, China
**e-mail: 1978hiking@gmail.com*

This study presents an electrochemical comparison of $Li||LiMn_{0.7}Fe_{0.3}PO_4$ coin cells using two different polymers as binders: PVDF and the water-soluble binder NV-1A. The charge/discharge curves obtained at a current rate of 0.05 C exhibit two well-defined plateaus at approximately 3.5 V and 4.1 V, corresponding to the Fe^{2+}/Fe^{3+} and Mn^{2+}/Mn^{3+} redox pairs, respectively. The capacity ratio of these plateaus is about 7:3, which matches the Mn/Fe ratio in the pristine material. The specific capacity of the coin cells with different binders falls within the range of 137–141 $mAh \cdot g^{-1}$, which is consistent with the manufacturer's specifications for the material. However, upon the first cycles, the coin cells with NV-1A binder exhibit a slightly lower specific capacity. This is attributed to the possible formation of Li_3PO_4 particles on the electrode surface, which leads to a decrease in specific capacity upon the initial cycles but improves the overall stability upon prolonged cycling. The first-cycle coulombic efficiency is 96.0 % for PVDF and 94% for NV-1A, increasing to 99.5% ± 0.1 % upon further cycling for both systems. Increasing the charge/discharge current density leads to a decrease in the specific capacity of $Li||LiMn_{0.7}Fe_{0.3}PO_4$ electrodes. This decrease is more pronounced for PVDF. At 0.5 C, the specific capacity reaches 68 $mAh \cdot g^{-1}$ for PVDF and 85 $mAh \cdot g^{-1}$ for NV-1A. Cyclic stability tests reveal that, despite the lower initial capacity of the NV-1A based coin cells, their capacity fade rate is only 0.1 % per cycle at 0.1 C, compared with 0.45 % for PVDF. Consequently, after 75 cycles, the NV-1A coin cells exhibit superior capacity retention. These findings are further discussed in the context of electrode degradation mechanisms upon cycling.

Key words: polymer binder, water-soluble binder, lithium manganese ion phosphate, galvanoatatic cycling, electrochemical impedance spectroscopy, capacity retention.

INTRODUCTION.

The development of lithium-ion battery (LIB) technologies is one of the key directions of modern science [1], driven by their widespread application in electric vehicles, energy storage systems, and portable electronic devices [2]. Particular attention has been paid to olivine-structured cathode materials [3, 4], especially $LiMn_xFe_{1-x}PO_4$ (LMFP) [5], which combines the high thermal stability of $LiFePO_4$ (LFP) with the elevated operating voltage (~4.1 V) characteristic of $LiMnPO_4$ [6, 7]. As a result, LMFP provides a higher energy density compared to conventional LFP (~3.4 V) without a significant loss of safety [8, 9]. However, LMFP exhibits intrinsically low electronic conductivity ($\approx 10^{-10}$–10^{-9} S/cm) and slow lithium-ion diffusion kinetics, which adversely affect its rate capability and cycling stability [6, 9].

One of the effective approaches to improving the electrochemical parameters of $LiMn_xFe_{1-x}PO_4$ is the optimization of electrode composition, particularly through the selection of a suitable polymer binder. As an essential component of LIB electrodes, the polymer binder mechanically holds together the active material particles and conductive additives, ensures adhesion to the current collector, and, via electrolyte wetting, facilitates lithium-ion transport to the cathode material. Improvement of the adhesive and cohesive properties of the binder positively affects the formation of the solid electrolyte interphase (SEI) during the initial charge–discharge cycles, which largely determines the overall resistance of both the electrode and the battery.

Polyvinylidene fluoride (PVDF) is traditionally used as a cathode binder; however, its processing requires the toxic organic solvent N-methyl-2-pyrrolidone (NMP). This complicates manufacturing, increases production costs, and raises environmental issues [10–12]. In recent years, the global trend has been towards replacing PVDF with water-soluble binders that are more cost-effective and environmentally friendly. Among them, polyacrylic acid (PAA)-based materials and their derivatives have attracted considerable interest [10–12], as they can reduce the internal resistance of electrode composites. Nevertheless, the rigid structure of PAA may lead to cracking of the electrode layer during cycling due to volume changes in the crystal lattice, resulting in the loss of electrical contact between particles and delamination of the electrode coating from the current collector.

To overcome these limitations, PAA is often modified with various monomers, particularly nitrogen-containing compounds, which improve adhesion through the formation of covalent bonds at the polymer–substrate interface [13] and enhance the flexibility of the material [14–17]. One such binder is NV-1A, a commercial water-soluble polymer based on polyacrylic acid modified with various monomers, including nitrogen-containing species, to improve its adhesive, cohesive, and mechanical properties.

Despite the considerable number of studies devoted to the synthesis and electrochemical performance of LMFP, the influence of polymer binders on the structural and electrochemical characteristics of LMFP cathodes remains insufficiently explored. Most recent investigations have focused on anode materials, whereas issues related to cathode microstructure formation, cycling stability, and adhesion properties remain largely unresolved [11, 18].

The aim of this work is to investigate the effect of binder type on the electrochemical

properties of $LiMn_{0.7}Fe_{0.3}PO_4$ cathode material. The combination of lithium manganese iron phosphate (LMFP) cathode material with a water-based polyacrylic acid (PAA) binder is a significant advancement in lithium-ion battery technology, offering novelty in i) environmental sustainability and manufacturing safety; (ii) superior electrochemical performance (PAA binders exhibit exceptional electrochemical properties that address key limitations of conventional binder systems); (iii) addressing LMFP-specific challenges (LMFP is a promising high-energy-density cathode material, but it suffers from manganese dissolution during charge-discharge cycles, which degrades battery life and storage performance. The novelty of PAA-based aqueous binders lies in their ability to mitigate this issue); (iv) superior adhesion and mechanical properties (the carboxyl-rich structure of PAA enables strong hydrogen bonding and covalent interactions with active material surfaces, providing excellent adhesion that maintains electrode integrity during volume changes. This is particularly valuable for LMFP cathodes, where structural stability is critical for long-term performance. Unlike conventional binders that rely on weak van der Waals forces, PAA offers robust mechanical properties essential for high-voltage operation); (v) cost-effectiveness and process compatibility (water-based PAA binders offer lower material costs and simplified manufacturing processes compared to NMP-based systems).

Thus, taking into account the above, the purpose of this work was to perform a comparative analysis of cycling performance and electrochemical impedance spectroscopy (EIS) data with two different binders. Based on the obtained results, the advantages of use the water-soluble NV-1A binder were evaluated, and possible explanations for the observed structural changes in the electrode material were proposed.

EXPERIMENT AND DISCUSSION OF THE RESULTS.

Commercial $LiMn_{0.7}Fe_{0.3}PO_4$ sample ("Qiquling Electrochemistry", Guangzhou, China) has been used as the cathode material.

Electrochemical tests have been performed in sample $Li||LiMn_{0.7}Fe_{0.3}PO_4$ cells on a Neware potentiostat/galvanostat (Shenzhen, Guandong, China). Working electrodes have consisted of 90 wt. % of the studied material, 5 wt. % of a conductive additive (soot) and 5 wt. % of binders (poly (vinyliden) difluoride and NV-1A ("Zhejiang Casnovo New Materials Co Ltd.")). A 50 μm layer of the slurry was applied onto aluminum foil with a doctor blade and then dried at 100–120 °C 18-21 h under a vacuum. The mass loading of $LiMn_{0.7}Fe_{0.3}PO_4$ in a dried electrode was 6.5–9 $mg{\cdot}cm^{-2}$. To increase the cathode density and improve the electrical contact between the active material particles and the conductive additive, the electrodes were pressed at a pressure of 190 MPa. This process reduced the electrode thickness from 65–66 to 50–52 μm. Coin cells were assembled in 2032 cases with Celgard 2500 separators and an electrolyte containing the 1 M solution of $LiPF_6$ in a mixture of ethylene carbonate and dimethyl carbonate taken in the 1:1 mass ratio. The reference and counter electrode were made of lithium metal. Galvanostatic tests have been performed within the voltage range of 2.0–4.5 V at the different current rates (0.05–1C). As noticed above, the theoretical specific capacity of the compound studied, $Li||LiMn_{0.7}Fe_{0.3}PO_4$ is 170 mAh/g, therefore, 1C = 170 $mAh{\cdot}g^{-1}$.

Impedance measurements were performed using an AUTOLAB electrochemical workstation (Netherlands) by applying a harmonic perturbation signal with an amplitude of 5 mV over the frequency range from 1 MHz to 10 mHz. The obtained spectra were processed using Nova 2.1 software. To approach the equilibrium state of the electrochemical cells, each spectrum was recorded after a relaxation period of no less than 2 h. All measurements were carried out at room temperature (25 °C), with the electrochemical cells maintained in a discharged state.

The charge/discharge curves for $Li||LiMn_{0.7}Fe_{0.3}PO_4$ coin cells at 0.05C are shown in Fig. 1. These curves exhibit two pairs of well-defined plateaus at approximately 3.5 V and 4.1 V, corresponding to the redox potentials of the Fe^{2+}/Fe^{3+} and Mn^{2+}/Mn^{3+} couples, respectively, with the capacity ratio of these plateaus being about 7/3, which is consistent with the Mn/Fe ratio in the raw material. The specific capacity of the coin cells with different binders varies slightly, ranging from 137 to 141 $mAh \cdot g^{-1}$, which agrees with the manufacturer's data sheet for the electrode material. At the same time, a lower specific capacity is observed during the initial cycles for the coin cells containing the NV-1A binder. As a tentative explanation and in accordance with Ref. [19], this effect is attributed to the aqueous processing technique, which promotes metal leaching, leading to the formation of Li_3PO_4 particles on the electrode surface. Although this layer improves the overall stability, it also reduces the specific capacity during the early stages of cycling.

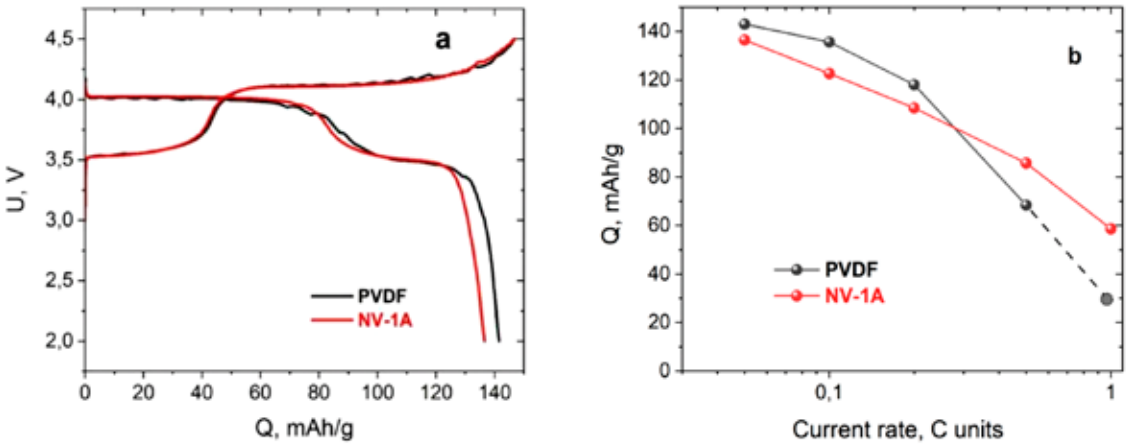

Fig. 1. Charge/discharge curves of the LMFP on the 1st cycle t 0.05C (a) and the change in specific capacity depending on the density of the discharge current (in "C" units) (b).

The coulombic efficiency obtained in the first cycle for $Li||LiMn_{0.7}Fe_{0.3}PO_4$ coin cells is 96.0 % (± 0.5 %) for the PVDF binder and 94 % (± 0.5 %) for NV-1A, respectively, and increases to 99.5 % (± 0.1 %) in the third cycle. An increase in the charge/discharge current density leads to a regular decrease in specific capacity (Fig. 1b). However, the decrease in specific capacity for $Li||LiMn_{0.7}Fe_{0.3}PO_4$ with the PVDF binder is more pronounced. Thus, at 0.5C, the

specific capacity of Li||$LiMn_{0.7}Fe_{0.3}PO_4$ is 68 and 85 mAh·g^{-1} for coin cells with PVDF and NV-1A binders, respectively. This sharp drop in specific capacity when using PVDF is attributed to the higher cell resistance associated with this binder material, as discussed below.

The cycling performance of Li||$LiMn_{0.7}Fe_{0.3}PO_4$ coin cells fabricated with the two types of binders is shown in Fig. 2. Cycles 1–35 reflect the variation in specific capacity upon cycling at different current densities (from 0.05C to 0.5C). Reference cycles 36–40 demonstrate the capacity retention after power tests, reaching 98% and 93% for the PVDF and NV 1A binders, respectively. Although cells with NV 1A exhibited lower initial capacity, their degradation at 0.1C (cycles 41–90) was only 0.1% per cycle versus 0.45% for PVDF. Although cells with NV 1A exhibited lower initial capacity, their degradation at 0.1C (cycles 41–90) was only 0.1% per cycle versus 0.45% for PVDF. Consequently, the capacity retention of the NV 1A-based cells exceeds that of PVDF-based cells after 75 cycles (Fig. 2). To explain this behavior, cell degradation was evaluated by electrochemical impedance spectroscopy (EIS).

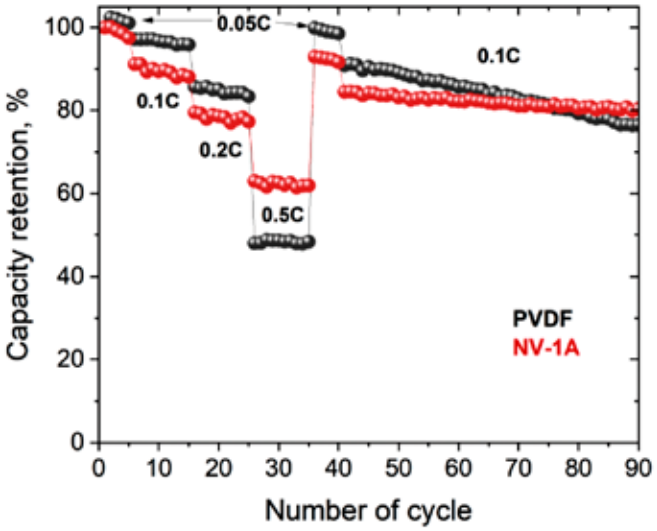

Fig. 2. Capacity retention of the LMFP electrodes upon cycling.

The change in impedance spectra upon cycling of Li||$LiMn_{0.7}Fe_{0.3}PO_4$ coin cells in 2032 case is shown in Fig. 3. Nyquist diagrams present a noticeable transformation of the impedance spectra from a "freshly assembled" sample to a sample "after 40 cycles". Namely, one semicircle of the spectrum, observed in the frequency range from $1 \cdot 10^5$ to 20 Hz and responsible for the process of charge transfer across the "electrode-electrolyte" interface, transforms into two clearly visible semicircles after 40 cycles. The first lies in the frequency range of $1 \cdot 10^5 \div 30$ Hz, while the second ranges from 30 to 0.5 Hz. These semicircles can be correlated with charge transfer processes across the "electrode-electrolyte" interface, where the first semicircle corresponds to charge transfer through the SEI formed on lithium metal

(R1). This is evidenced by the coincidence of the frequency range in the Bode diagrams of the impedance spectra of a coin cell with varying degrees of degradation, accompanied by a slight shift of the maximum to the low-frequency region with an increase in the number of cycles. The second semicircle, observed in the frequency range from 30 to 0.5 Hz, is absent in the freshly assembled element.

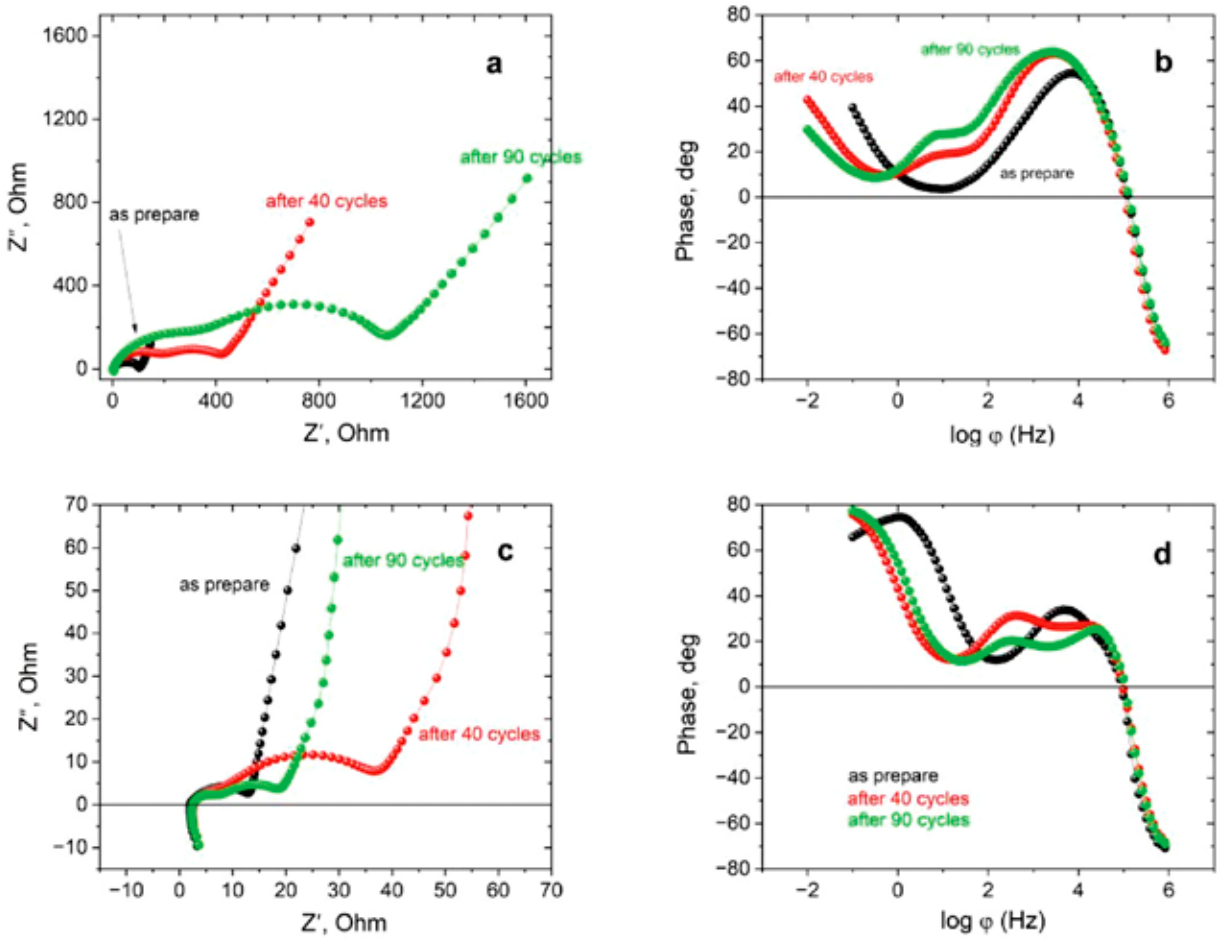

Fig. 3. Nyquist diagrams, and Bode diagrams with varying degrees of degradation of the coin cell, cathode composition: 90% - LMFP+ 5% - super P + 5% binder (a,b – PVDF; c,d – NV-1A).

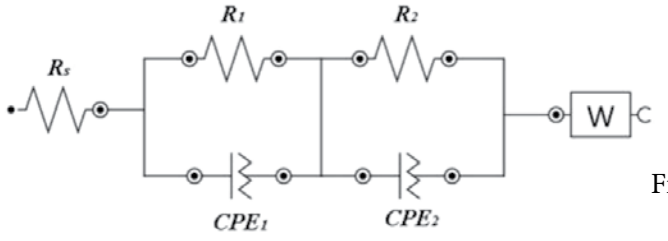

Fig. 4. An equivalent circuit used in processing impedance spectra.

The appearance and transformation of this arc can be observed upon cycling of the coin cell, which is characteristic of the formation of a high-resistance SEI film (probably due to the formation of a poorly conductive layer on the surface of the electrodes consisting of products of the interaction of manganese ions with an electrolyte at high potentials, for example MnF_2, $MnCO_3$ [20] on the surface of the cathode material *(R2)*. In addition, the frequency of the maximum of the second f_{max} arc is in the typical range for cathodic charge transfer in lithium-ion batteries (usually 0.001–0.5 kHz). SEI on lithium usually manifests itself at higher frequencies (1–100 kHz), which is observed in the impedance spectra [21, 22].

The equivalent circuit used in the fitting of impedance spectra is shown in Fig. 4. The R_s parameter in the equivalent circuit corresponds to the resistance of the electrolyte in the separator pores and is determined in the frequency range of 1–0.1 MHz. It should be noted that the R_s values exhibit non-monotonic dynamics upon cycling, which is typical for lithium-ion cells and is associated with a combination of physicochemical processes (changes in wettability, contact resistances, temperature fluctuations, etc.). However, the absolute changes in R_s do not exceed 0.7 Ω, which amounts to less than 1% of the total cell resistance R_{ct} at low frequencies and does not significantly affect the regularities discussed in this work. Table 1 lists the calculated parameters of the constituent elements and their variation upon cycling of the LMFP cells.

Table 1.

EIS data for the electrodes with different types of binders.

Binder	Parameter							
	State of the coin cell	$R_{s,}$ Ohm	$R_{1,}$ Ohm	$R_{2,}$ Ohm	$R_{ct,}$ Ohm	f_{max}, Hz	$C_{dl,}$ μF	$A_{active,}$ cm²
PVDF	as prepare	3.20	-	-	103.50	-	-	-
	after 40 cycles	2.90	226	368	492	4	108.00	5.41
	after 90 cycles	3.50	480	936	1164	4	32.50	2.13
NV-1A	as prepare	2.01	-	-	12.57	-	-	-
	after 40 cycles	2.71	6.85	34.19	38.49	150	27.56	1.38
	after 90 cycles	2.47	5.00	15.28	19.25	150	69.40	3.47

* – The measurement error of the equivalent circuit parameters does not exceed 5%.

To estimate the double-layer capacitance (C_{dl}) and to calculate the electrochemically active surface area (A_{act}) of the electrode, the parameters of the low-frequency arc were employed. This arc corresponds to the charge transfer process through the solid electrolyte interphase (SEI) formed on the cathode material. The resistance *R2* and the maximum frequency f_{max} of this arc allow C_{dl} to be calculated using the formula for a parallel RC circuit, under the assumption that the low-frequency arc is not significantly distorted by diffusion:

$$C_{dl} = \frac{1}{2\pi f_{\max} R2}, \quad (1)$$

where f_{max} is the frequency at the apex of the arc, corresponding to the maximum of the imaginary component -Z" on the charge-transfer semicircle.

The electrochemically active surface area A_{act} is related to the double-layer capacitance by the following expression:

$$A_{act} = \frac{C_{dl}}{S_{sp}}, \quad (2)$$

where S_{sp} is the specific double-layer capacitance per unit of true surface area. For smooth electrodes, this value typically lies in the range of 10 - 40 μF/cm^2, and may be slightly higher for porous or rough surfaces.

In the present work, a value of S_{sp}=20 μF/cm^2 was adopted for calculations. This is a commonly accepted reference value for flat surfaces and is widely used in the literature (e.g., Moriguchi et al. [23] reported a value of 20 ± 2 μF/cm^2 for ideal carbon surfaces). Similar values have been reported by other authors. For instance, Hang Shi estimated the specific double-layer capacitance on the micropore surface to be approximately 15–20 μF cm^{-2} [24]. This assumption was introduced for comparative purposes to assess the relative changes in the electrochemically accessible surface area upon cycling within the same series of experiments. It should be emphasized that the obtained A_{act} values do not represent the absolute true surface area, but rather provide an effective electrochemically active surface area within the framework of a smooth-electrode model.

The calculated A_{act} values reliably reflect the relative changes in the surface area available for electrochemical processes during cycling. For the PVDF-based electrodes, a decrease in A_{act} from 5.41 cm² (after 40 cycles) to 2.13 cm² (after 90 cycles) was observed. This trend correlates well with the increase in charge-transfer resistance R2 and the corresponding drop in capacity retention from 98% to 76%, respectively. These findings suggest progressive surface passivation and loss of active sites due to the formation of a blocking interfacial layer.

In contrast, for the PAA-based electrodes, a decrease and subsequent stabilization of the charge-transfer resistance *R2* was observed, along with a steady increase in A_{act}. This indicates an expansion of the electrochemically active surface area, which may be attributed to continuous electrolyte infiltration and/or the development of microcracks without loss of electrical contact between particles. The capacity retention for the PAA-based samples was found to be 92% and 80% after 40 and 90 cycles, respectively, further confirming the superior performance of this binder compared to PVDF.

CONCLUSIONS.

A comparative study of the $LiMn_{0.7}Fe_{0.3}PO_4$ cathode material with two types of polymer binders (conventional PVDF and water-soluble NV-1A (PAA-based)) reveals significant differences in their electrochemical behavior upon cycling.

1. The charge transfer resistance (*Rct*) for the electrodes based on the NV-1A binder remains practically unchanged upon cycling (from 12.6 Ω as prepared to 15.3 Ω after 90 cycles), whereas for the PVDF-based electrodes a nearly 10-fold increase in Rct*Rct* is observed (from 103.5 Ω to 936 Ω after 90 cycles). This indicates a substantially higher stability of the electrode/electrolyte interface when using the water-soluble binder.

2. The use of the NV-1A binder results in higher specific capacity of the material at C/2

and higher rates, as well as lower capacity loss upon cycling, compared to the standard PVDF binder. These observations are consistent with the impedance data and confirm the better electrochemical performance of the PAA-based system.

3. The calculated effective electrochemically active surface area (A_{act}) for the NV-1A-based electrodes shows an increasing trend upon cycling (from 1.38 cm^2 after 40 cycles to 3.47 cm^2 after 90 cycles), whereas for the PVDF-based electrodes a decrease is observed (from 5.41 to 2.13 cm^2). The observed increase in A_{act} for the PAA-based system may be tentatively attributed to progressive electrolyte infiltration and/or the development of microcracks without loss of electrical contact between particles, which could lead to additional surface availability for electrochemical reactions. However, direct evidence for this hypothesis is not available within the scope of the present work, and the obtained A_{act} values should be considered as relative estimates rather than absolute surface areas. In contrast, the decrease in A_{act} for the PVDF-based electrodes is consistent with gradual blocking of the electrode surface by the accumulation of electrolyte decomposition products and/or manganese dissolution products (e.g., MnF_2, $MnCO_3$), leading to reduced availability of active sites for lithium-ion insertion and ultimately resulting in capacity decay upon prolonged cycling.

Overall, the water-soluble binder NV-1A demonstrates clear advantages over the conventional PVDF binder in terms of interfacial stability and capacity retention, making it a promising candidate for high-performance LMFP cathodes. Further studies, including post-cycling surface analysis (e.g., SEM, XPS, or BET), are required to clarify the mechanism of the observed increase in the electrochemically active surface area.

ACKNOWLEDGMENTS.

We appreciate the international collaboration with Zhejiang Casnovo New Materials Co., Ltd (China) and the opportunity to conduct a series of studies using its laboratory facilities.

AUTHORS' CONTRIBUTION:

O.V. Potapenko: investigation, methodology, datacuration, visualization, writing – original draft.
H.V. Potapenko: supervision, conceptualization, methodology, writing review & editing.
V.O. Oliinyk: writing – original draft, visualization, data curation, writing review & editing.
V.A. Sirosh: investigation, data curation, visualization.
Changji Zhou: investigation, data curation.
Chee Sien Wong: data curation.
Changbo Yu: investigation, data curation.
Chenchun Zhang: data curation, visualization.

All authors have read the results of the study and approved the final version of the manuscript.

CONFLICT OF INTEREST. The authors declare no conflict of interest.

FUNDING. This work was carried out with the support of the National Academy of Sciences of Ukraine as part of a research project commissioned by the Chemistry Department of the National Academy of Sciences of Ukraine titled "Modification of materials obtained from the recycling of lithium iron phosphate batteries in order to improve their energy characteristics", registration number 0126U001632.

ВПЛИВ ПРИРОДИ ЗВ'ЯЗУВАЧА НА ЕЛЕКТРОХІМІЧНІ ВЛАСТИВОСТІ КАТОДНОГО МАТЕРІАЛУ $LiMn_{0.7}Fe_{0.3}PO_4$

О. В. Потапенко[1], Г. В. Потапенко[1,2], В. О. Олійник[1], В. А. Сірош[1], С. Тичина[1], Чанцзі Чжоу[2], Чі Сянь Вонг[2,3], Чанбо Юй[2], Ченьчунь Чжан[2]

[1] Інститут загальної та неорганічної хімії ім. В.І. Вернадського НАН України, просп. Академіка Палладіна, 32/34, Київ 03142, Україна;
[2] Компанія «Чжецзян Касново Нью Матеріалс» (Zhejiang Casnovo New Materials Co., Ltd.), вул. Чжунке, 1, вулиця Чжаньмао, район Путуо, м. Чжоушань, провінція Чжецзян, Китай;
[3] Факультет нафтохімічної інженерії та довкілля, Чжецзянський океанічний університет, Південна вулиця Хайда, 1, вулиця Лінчен, район Дінхай, м. Чжоушань, провінція Чжецзян, Китай
e-mail: 1978hiking@gmail.com

Дослідження присвячено електрохімічному порівнянню макетів ґудзикового типу $Li||LiMn_{0.7}Fe_{0.3}PO_4$ з використанням двох різних полімерів: PVDF та водорозчинного зв'язувача NV-1A. Криві заряджання/розряджання, отримані за струму 0.05 C, демонструють два чітко виражені плато приблизно при 3.5 В та 4.1 В, які відповідають окисно-відновним парам Fe^{2+}/Fe^{3+} та Mn^{2+}/Mn^{3+} відповідно. Співвідношення ємностей цих плато становить близько 7:3, що відповідає співвідношенню Mn/Fe у вихідному матеріалі. Питома ємність макетів ґудзикового типу з різними матеріалами-зв'язувачами знаходиться в межах 137–141 мАгод·г$^{-1}$ та узгоджується з паспортними характеристиками матеріалу. Однак на перших циклах макети ґудзикового типу з NV-1A демонструють дещо нижчу питому ємність. Це пов'язано з можливим утворенням частинок Li_3PO_4 на поверхні електрода, що призводить до зменшення питомої ємності на початкових циклах, але покращує загальну стабільність при тривалому циклюванні. Кулонівська ефективність першого циклу становить 96.0 % для PVDF та 94 ± 0,5 % для NV-1A, збільшуючись до 99.5 ± 0.1 % при подальшому циклуванні для обох систем. Збільшення густини струму заряду/розряду призводить до зменшення питомої ємності $LiMn_{0.7}Fe_{0.3}PO_4$, проте це зменшення є більш вираженим для PVDF: при 0.5 C ємність становить 68 мАгод·г$^{-1}$ для PVDF та 85 мАгод·г$^{-1}$ для NV-1A. Випробування циклічної стабільності показали, що, незважаючи на нижчу початкову ємність макетів ґудзикового типу на основі NV-1A, швидкість деградації їхньої ємності становить лише 0.1 % за цикл при 0.1 C, тоді як для PVDF цей показник дорівнює 0.45 %. У результаті після 75 циклів макетів ґудзикового типу із NV-1A демонструють кращу схоронність заряду. Отримані результати додатково обговорюються з точки зору механізмів деградації електродів у процесі циклування.

Ключові слова: полімерний зв'язувач, водорозчинний зв'язувач, літій-манган-залізо-фосфат, гальваностатичне циклування, електрохімічна імпедансна спектроскопія, збереження ємності.

REFERENCES

[1] Sciatti F., Tamburrano P., Distaso E., Amirante R., Radogna A.V., Morciano A., Grassi G. A comprehensive overview of lithium-ion batteries for electric vehicles: Materials, performance, safety, recycling, and emerging technologies. *J. Energy Storage*. 2026. **144**: 119694–119726. https://doi.org/10.1016/j.est.2026.119694.

[2] Xu C., Dai Q., Gaines L., Hu M., Tukker A., Steubing B. Future material demand for automotive lithium-based batteries. *Commun. Mater*. 2020. **1**: 99. https://doi.org/10.1038/s43246-020-00095-x.

[3] Manfo T.A., Laaksonen H. A Comparative study of the modified high voltage olivine-phosphate $LiMPO_4$ (M = Fe, Mn, Co, Ni) as promising cathode materials for next-generation rechargeable batteries. *J. Energy Storage*. 2026. **160**: 121797–121823. https://doi.org/10.1016/j.est.2026.121797.

[4] Dorri M., Nekahi A., Ahmed S., Dawkins J.I.G., Guimaraes T.M.S., Kumar M.R.A., Zaghib K. Exploring sustainable lithium iron phosphate cathodes for Li-ion batteries: From mine to precursor and cathode production. *J. Power Sources*. 2025. **656**: 238041–238061. https://doi.org/10.1016/j.jpowsour.2025.238041.

[5] Hirayama Y., Oikawa M., Yokoyama A., Kegami J., Ishida H., Ogami T. Electrochemical performance of spherical $LiMn_{0.7}Fe_{0.3}PO_4$ cathode materials for lithium-ion batteries. *Muki Mater*. 2025. **32** (Suppl.): P. 38–46. https://doi.org/10.11451/mukimate.25.Suppl.07.

[6] Wen Z. et al. Research progress in lithium manganese iron phosphate cathode material modification. Energy Storage Sci. Technol. 2024. https://doi.org/10.19799/j.cnki.2095-4239.2023.0771.

[7] Huang S., Lin W., Li L. et al. Pathway for high-energy density $LiMnFePO_4$ cathodes. *Prog. Nat. Sci.: Mater. Int*. 2023. **33** (1): 126–131. https://doi.org/10.1016/j.pnsc.2023.01.003.

[8] Zeng Y., Wang X., Li X. et al. Sustainable $LiFePO_4$ and $LiMn_xFe_{1-x}PO4$ (x = 0.1–1) cathode materials for lithium-ion batteries: A systematic review from mine to chassis. *Mater. Sci. Eng. R: Rep*. 2024. **159**: 100797. https://doi.org/10.1016/j.mser.2024.100797.

[9] Yang L., Deng W., Xu W. et al. Unlocking the full potential of $LiMn_{1-x}Fe_xPO_4$: Advances in synthesis, modification, and future directions for high-energy cathode materials. *Mater. Today Energy*. 2025. **52**: 101965. https://doi.org/10.1016/j.mtener.2025.101965.

[10] Ajayi S.O., Dolla T.H., Makgwane P.R. et al. A review of aqueous-based binders used for cathode fabrication in lithium-ion batteries. *RSC Sustain*. 2026. **4**: 1160–1179. https://doi.org/10.1039/D5SU00849B.

[11] Yoon J., Lee J., Kim H. et al. Polymeric binder design for sustainable lithium-ion battery chemistry. Polymers. 2024. 16: 254. https://doi.org/10.3390/polym16020254.

[12] Rolandi A.C., de Meatza I., Casado N., Forsyth M., Mecerreyes D., Pozo-Gonzalo C. Unlocking sustainable power: Advances in aqueous processing and water-soluble binders for NMC cathodes in high-voltage Li-ion batteries. *RSC Sustain*. 2024. **2**: 2125–2149. https://doi.org/10.1039/D4SU00098F.

[13] Crosby A.J., Hageman M., Duncan A. Controlling polymer adhesion with "pancakes". *Langmuir*. 2005. **21**: 11738–11743. https://doi.org/10.1021/la051721k.

[14] Li J., Sun J., Shi H., Liu J. Water-based binder and cathode slurry for lithium-ion battery as well as preparation methods for water-based binder and cathode slurry: Pat. CN104789160A China. № CN201510161982.7; filed 08.04.2015; publ. 22.07.2015.

[15] Yuca N., Zhao H., Song X. et al. A systematic

investigation of polymer binder flexibility on the electrode performance for lithium-ion batteries. *ACS Appl. Mater. Interfaces*. 2014. **6**(19): 17411–17418. https://doi.org/10.1021/am504736y.

[16] Aoki S., Han Z.J., Yamagiwa K., Yabuuchi N. et al. Acrylic acid-based copolymers as functional binder for silicon/graphite composite electrode in lithium-ion batteries. *J. Electrochem. Soc*. 2015. **162** (12): A2245–A2249. https://doi.org/10.1149/2.0171512jes.

[17] Hu H., Zhang L., Jin S., Hu W., Jiang N., Xu X., Zhou J. Water-soluble binder, lithium-ion battery cathode paste prepared by using water-soluble binder, preparation methods and coating methods thereof: Pat. CN104293239A China. № CN201410521837.0; filed 30.09.2014; publ. 21.01.2015.

[18] Zhang Y., Liu X. et al. Beyond binding: A review on binders in high-voltage transition metal oxide cathode of lithium-ion battery. *J. Energy Storage*. 2024. **97**: 112816. https://doi.org/10.1016/j.est.2024.112816.

[19] Akhilash M., Salini P.S., John B., Sujatha S., Mercy T.D. A comparative study of aqueous- and nonaqueous-processed Li-rich $Li_{1.5}Ni_{0.25}Mn_{0.75}O_{2.5}$ cathodes for advanced lithium-ion cells. *RSC Sustain*. 2024. **2**: 416–424. https://doi.org/10.1039/D3SU00168G.

[20] Wohlfahrt-Mehrens M., Vogler C., Garche J. Aging mechanisms of lithium cathode materials. *J. Power Sources*. 2004. **127**: 58–64. https://doi.org/10.1016/j.jpowsour.2003.09.034.

[21] Schmidt J.P., Chrobak T., Ender M., Illig J., Klotz D., Ivers-Tiffée E. Studies on $LiFePO_4$ as cathode material using impedance spectroscopy. *J. Power Sources*. 2011. **196**: 5342–5348. https://doi.org/10.1016/j.jpowsour.2010.09.121.

[22] Qiu X.-Y., Zhuang Q.-C., Zhang Q.-Q., Cao R., Qiang Y.-H., Ying P.-Z., Sun S.-G. Investigation of layered $LiNi_{1/3}Co_{1/3}Mn_{1/3}O_2$ cathode of lithium ion battery by electrochemical impedance spectroscopy. *J. Electroanal. Chem*. 2013. **688**: 393–402. https://doi.org/10.1016/j.jelechem.2012.09.027.

[23] Moriguchi I., Nakahara F., Furukawa H., Yamada H., Kudo T. Colloidal Crystal-Templated Porous Carbon as a High Performance Electrical Double-Layer Capacitor Material. *Electrochem. Solid-State Lett*. 2004. **7**(8): A221–A223. https://doi.org/10.1149/1.1756491.

[24] Shi H. Activated carbons and double layer capacitance. *Electrochim. Acta*. 1996. **41**: 1633–1639. https://doi.org/10.1016/0013-4686(95)00416-5.

Стаття надійшла: 09.04.2026.
Статтю прийнято до друку: 13.05.2026.
Статтю опубліковано: 25.06.2026.

UDC 546.26-162: 541.13:549.21 doi: 10.33609/2708-129X.92.5.2026.31-63

APPLICATION OF D-AMINO ACIDS IN DRUG DESIGN (review)

Alicja Wzorek[1]: https://orcid.org/0000-0001-9041-7034;
Taizo Ono[2]: https://orcid.org/0009-0002-3268-2344;
Daniel Baecker[3]: https://orcid.org/0000-0002-1963-9838;
Wei Zhang[4]: https://orcid.org/0000-0002-6097-2763;
Hiroki Moriwaki[5]: https://orcid.org/0000-0002-2028-2565;
Kunisuke Izawa;
Hiroyuki Konno[6]: https://orcid.org/0000-0002-6629-6102;
Vadim A. Soloshonok[2,7*]: https://orcid.org/0000-0003-0681-4526.

[1] Institute of Chemistry, Jan Kochanowski University in Kielce, Uniwersytecka 7, 25-406 Kielce, Poland;
[2] National Institute of Advanced Industrial Science and Technology (AIST), 2266-98, Anagahora, Shimoshidami, Moriyama-ku, Nagoya, 463-8560, Japan;
[3] Department of Pharmaceutical and Medicinal Chemistry, Institute of Pharmacy, Freie Universität Berlin, Königin-Luise-Straße 2+4, 14195 Berlin, Germany;
[4] Department of Chemistry, University of Massachusetts Boston, Boston MA 02125, Unites States
[5] Hamari Chemical Ltd., Osaka, Japan;
[6] Department of Chemistry and Biological Engineering, Graduate School of Science and Engineering, Yamagata University, 992–8510 Yonezawa, Yamagata, Japan;
[7] IKERBASQUE, Basque Foundation for Science, María Díaz de Haro 3, Plaza Bizkaia, 48013 Bilbao, Spain.
E-mail: vadimsoloshonok@gmail.com

Dedication: To Professor Tamio Hayashi — a giant in the realm of asymmetric catalysis, a North Star of a man, whose guidance has gifted generations of chemists their most formative intellectual experiences.

D-Amino acids (D-AAs) have become indispensable building blocks in modern peptide drug design. Although relatively rare in higher organisms, D-AAs are widely utilized in nature, particularly in bacterial peptidoglycans and microbial antimicrobial peptides, where they confer proteolytic stability and unique biological activities. Inspired by these natural strategies, medicinal chemists have successfully incorporated D-Aas into synthetic peptides to overcome the inherent limitations of conventional peptide therapeutics, such as rapid enzymatic degradation and poor bioavailability. The incorporation of D-AAs offers several key advantages, including dramatically enhanced proteolytic resistance, prolonged plasma

half-life, reduced immunogenicity, and improved receptor selectivity. These properties have enabled the development of clinically successful drugs across multiple therapeutic areas. Prominent examples include the early antibiotic gramicidin D (1955), the immunosuppressive agent cyclosporine, D-penicillamine, daptomycin, etelcalcetide, difelikefalin, and voclosporin. These compounds illustrate the transformative impact of D-AAs on peptide pharmacology and their expanding role in treating infectious diseases, autoimmune disorders, nephrological conditions, and beyond.

This review highlights the strategic importance of D-AAs in pharmaceutical design, their natural occurrence, clinical applications, and major advances in synthetic methodologies, with particular emphasis on the versatile Ni(II) Schiff base complex approach for the preparation of tailor-made D-AAs. The evolution of D-AA-containing pharmaceuticals demonstrates how stereochemical engineering continues to drive innovation in peptide drug discovery and development.

Keywords: D-amino acids, chirality, chirobiotics, Ni(II) complexes, drug design, proteolytic stability, peptide therapeutics, marketed pharmaceuticals.

INTRODUCTION. The biochemistry of life exhibits a strong preference for homochiral peptides and proteins, composed almost exclusively of L-amino acids (L-AAs) [1-3]. This chiral homogeneity confers critical advantages in structural stability, folding efficiency, and functional precision that racemic or heterochiral mixtures cannot achieve. Consistent chirality enables the formation of stable, regular secondary structures, particularly α-helices and pleated β-sheets, which rely on uniform backbone dihedral angles (φ/ψ) and regular i to i+4 hydrogen bonding patterns [4-6]. Introducing D-amino acids (D-AAs) disrupts this geometry, preventing helix propagation and reducing the number of backbone hydrogen bonds (approximately 60% in homochiral proteins versus ~30% in demi-chiral models). This leads to a narrower and deeper folding funnel toward the native state, lowering the entropic cost of folding by restricting the unfolded ensemble and increasing the thermodynamic stability of compact conformations through enhanced enthalpy from helical collapse and backbone interactions. In contrast, racemic systems favor rippled β-sheets (as predicted by Pauling and Corey) [7], which exhibit distinct geometry and often stronger inter-strand associations but are incompatible with the compact, functional folds required for enzymatic active sites and molecular recognition. Homochirality further ensures precise stereospecific interactions with other chiral biomolecules (e.g., D-sugars in nucleic acids), supporting efficient catalysis, ligand binding, and biochemical cooperativity [4]. Evolutionarily, once a slight chiral bias emerged, via amplification through polymerization [8,9], self-disproportionation of enantiomers [10-12], and selection favored homochiral systems, as their superior folding reliability and functional competence provided a decisive competitive edge over mixed-chira-

lity alternatives in sustaining metabolism and replication. Thus, homochirality is not merely a historical contingency but a biochemical necessity enabling the sophisticated protein machinery central to terrestrial life [4].

Similar to the xenobiotic fluorine, which has revolutionized medicinal chemistry by conferring enhanced metabolic stability, bioavailability, and receptor affinity to pharmaceutical compounds [13-17], abiotic D-AAs, here termed chirobiotics, possess tremendous yet largely untapped potential in drug design, offering unique stereochemical advantages that can circumvent biological degradation pathways and modulate molecular interactions in ways unattainable with their L-configured counterparts. In this review article, we delve into the natural occurrence of D-AAs, ranging from their presence in bacterial peptidoglycans and antimicrobial peptides to their roles as neuromodulators in eukaryotic systems, while also examining state-of-the-art synthesis methodologies that enable scalable production for therapeutic applications. Moreover, we outline the major avenues for their pharmaceutical exploitation as chirobiotics, such as in the development of protease-resistant peptides for antimicrobial and anticancer therapies, enantioselective receptor agonists or antagonists for neurological disorders, and immunomodulatory agents that exploit chirality to enhance specificity and reduce immunogenicity. Furthermore, we trace the evolutionary trajectory of D-AA–containing drugs, from their serendipitous discovery in natural products like gramicidin [18] and cyclosporine [19], through preclinical optimizations addressing pharmacokinetic challenges, to pivotal milestones including the first regulatory approvals by agencies such as the U.S. Food and Drug Administration (FDA) for compounds like D-penicillamine in treating Wilson's disease and rheumatoid arthritis, thereby illustrating a paradigm shift toward incorporating abiotic chirality in modern pharmacopeia. This review article will be of interest to medicinal chemists, pharmacologists, biochemists, and drug discovery professionals seeking to harness D-amino acids as innovative chirobiotic tools in addressing unmet medical needs, fostering interdisciplinary collaborations to unlock their full therapeutic promise.

Natural occurrence. D-AAs occur naturally across a wide range of biological systems. They are particularly prominent in microorganisms, where D-alanine (D-Ala) and D-glutamic acid (D-Glu) serve as key components of the bacterial peptidoglycan in cell walls, contributing to structural integrity and resistance.

Beyond bacteria, D-AAs appear in numerous bioactive natural compounds, including peptides produced by algae, fungi, marine invertebrates, and even some vertebrates, with at least 132 documented peptide natural products incorporating D-AAs such as D-Ala, D-valine (D-Val), D-leucine (D-Leu), D-serine (D-Ser) (Fig. 1), and others. Across these organisms, D-AAs are not rare curiosities but purposeful molecular features that shape peptide stability, bioactivity, and ecological interactions. In marine organisms, this stability supports peptides that must persist in high-salinity or protease-rich surroundings [20]. In fungi and algae, D-AAs help maintain bioactive conformations that would otherwise be unstable [21].

Free D-AAs in higher organisms, including mammals and humans, arise through intrinsic biosynthesis, gut microbiota, diet, and age-related racemization. Among them, D-Ser is the key endogenous co-agonist at

the glycine site of *N*-methyl-D-aspartate receptors (NMDARs), enabling full receptor activation with glutamate. It is more potent than glycine and predominates in forebrain regions such as the cortex and hippocampus. Formed from L-serine by the serine racemase (mainly neuronal in adults), D-serine is released synaptically—often via glia—to drive calcium influx, synaptic plasticity (long-term potentiation and long-term depression, LTP/LTD), learning, memory, neuronal maturation, and cognitive processes including mood regulation and fear extinction [22].

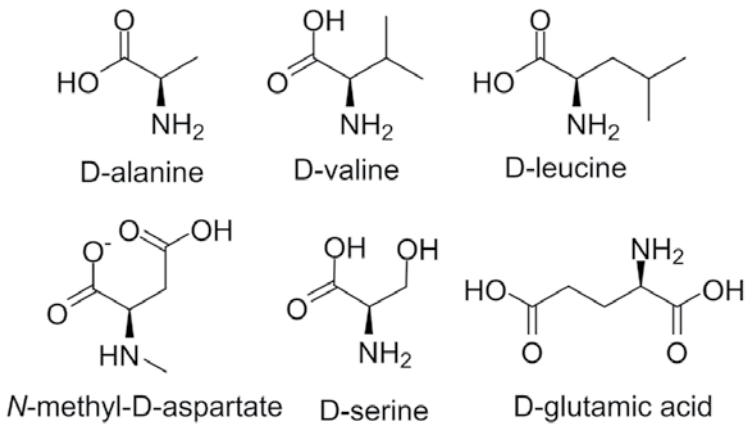

Fig. 1. Chemical structures of some D-AAs found in higher organisms.

Disrupted D-Ser signaling contributes to disease: reduced levels and NMDAR hypofunction are linked to schizophrenia, Alzheimer's disease, and age-related cognitive decline, whereas excess D-Ser can promote excitotoxicity in ischemia or epilepsy. In aging, forebrain D-Ser typically declines, correlating with impaired NMDAR activity, weaker plasticity, and deficits in learning and memory. Experimental D-Ser supplementation can restore NMDAR function, connectivity, and neuronal structure, improving cognitive performance in aging models [23].

In proteins, particularly long-lived ones like lens crystallins, tooth enamel, or certain brain proteins, L-AAs (mainly L-aspartate/L-asparagine) undergo time-dependent spontaneous racemization to D-forms (e.g., D-Asp) during aging. This alters protein higher-order structure, function, and stability, contributing to age-related diseases such as cataracts, Alzheimer's (via protein misfolding/aggregation), and other degenerative conditions. D-AAs accumulate progressively with age, serving as a molecular index of aging and protein "fatigue" damage [24].

D-AAs are also detected in plants, soils, aquatic environments, and processed foods, highlighting their broader ecological distribution and roles in physiological functions, microbial competition, and potentially disease-related processes [25].

Primary Advantages and Applications of D-AAs in drug design. L-AAs are fundamental to modern drug design [26-30]. They provide chiral, metabolically compatible building blocks that shape the three-dimensional archi-

tecture, stability, and biological activity of therapeutic molecules. Their natural stereochemistry allows medicinal chemists to construct peptides, peptidomimetics, and small-molecule scaffolds that engage protein targets with high affinity and selectivity, while minimizing immunogenicity and improving pharmacokinetic behavior. L-AAs contribute functional diversity through side-chain chemistry, enabling hydrogen bonding, hydrophobic packing, metal coordination, and covalent interactions, and their predictable metabolic pathways support rational optimization of absorption, distribution, and clearance [31-33].

Incorporating non-natural, tailor-made amino acids greatly expands the utility of L-AAs in drug design by introducing functions and physicochemical properties that natural residues cannot provide [32]. These engineered amino acids allow medicinal chemists to fine-tune molecular conformation, polarity, lipophilicity, metabolic stability, and target engagement with a level of precision that surpasses the natural amino acid repertoire. Side-chain modifications can introduce steric bulk, hydrogen-bonding motifs, redox activity, metal-binding groups, or conformational constraints that enhance potency and selectivity while reducing off-target effects or proteolytic degradation. Among these designer residues, fluorinated amino acids are the most extensively studied and widely applied. The unique electronic and steric characteristics of fluorine enable modulation of pK_a, dipole moments, hydrophobicity, and metabolic resistance, allowing strategic control over binding affinity, membrane permeability, and pharmacokinetic behavior. As a result, tailor-made—and especially fluorinated—amino acids serve as powerful tools for optimizing peptide therapeutics, stabilizing secondary structure, improving oral bioavailability, and designing next-generation peptidomimetics and small-molecule scaffolds [34–39].

The incorporation of D-AAs represents a cornerstone strategy in contemporary peptide and protein drug design, addressing key limitations of natural L-AAs-based therapeutics while enabling novel pharmacological profiles. Unlike their L-enantiomers, which predominate in eukaryotic biology, D-AAs confer distinct advantages rooted in stereochemical differences that disrupt recognition by endogenous proteases, alter conformational dynamics, and modulate biological interactions.

Enhanced Proteolytic Stability and Pharmacokinetic Profile. The most established rationale for D-AA incorporation is resistance to enzymatic degradation. Proteases exhibit high stereospecificity for L-configured peptide bonds, rendering D-AA-substituted sequences dramatically more stable in plasma, gastrointestinal environments, and intracellular compartments [40-42]. This often translates to extended half-lives (up to orders of magnitude in some cases), reduced dosing frequency, and improved bioavailability—critical for transitioning from injectable to potentially oral formulations. In practice, partial or full D-AA substitution (e.g., retro-inverso or mirror-image designs) [43] has been pivotal in developing long-acting analogs of natural peptides, such as somatostatin (octreotide with D-Trp) [44], and supports emerging oral peptide candidates like cyclic PCSK9 inhibitors [45].

Improved Conformational Rigidity and Target Binding. D-AAs introduce local stereochemical perturbations that favor specific secondary structures (e.g., β-turns via D-Pro or D-AA-induced turns), enhancing receptor affinity,

selectivity, and potency. In cyclic or constrained peptides, strategic D-AA placement stabilizes bioactive conformations, often yielding superior binding kinetics compared to all-L-configured counterparts. This is particularly valuable in targeting G-protein coupled receptors (GPCRs), ion channels, or enzymes where precise geometry dictates efficacy [46-48].

Reduced Immunogenicity and Toxicity. Full D-peptides (mirror-image proteins) evade immune surveillance due to non-recognition by major histocompatibility complex (MHC) presentation pathways and lack of proteolytic processing into immunogenic fragments. This property underpins mirror-image phage display technologies for discovering ultra-stable, non-immunogenic binders against challenging targets (e.g., human immunodeficiency virus (HIV) entry inhibitors like CPT31 in clinical trials). Heterochiral designs can also mitigate cytotoxicity in self-assembling biomaterials or amyloid-targeted therapies [49, 50].

Disruption of Biofilms and Antimicrobial Enhancement. D-AAs (especially free D-AAs or D-AA-rich peptides) interfere with bacterial peptidoglycan synthesis, quorum sensing, and biofilm integrity, offering synergistic effects with conventional antibiotics against resistant pathogens. This application extends to preventing microbial colonization in medical devices and combating chronic infections [51, 52].

Direct Therapeutic Effects and Emerging Roles. Certain D-AAs serve as bioactive entities themselves (e.g., D-Ser as an NMDA receptor co-agonist in neurological disorders; D-Trp/D-Phe modulators in neurology). D-AA-containing natural products inspire anticancer, antimicrobial, and neuroprotective agents, with some exerting antiproliferative effects via metabolic pathways (e.g., H_2S generation from D-Cys). In cancer, D-AAs show promise as prodrugs in oxidase-based therapies or as inhibitors of tumor proliferation [53, 54].

Facilitation of Advanced Delivery and Biomaterials. Heterochiral self-assembling peptides form nanostructured hydrogels with unexpected benefits, including altered gelation kinetics, reduced cytotoxicity, and enhanced drug release profiles for localized therapy (e.g., in wound healing or tissue engineering) [55, 56].

Illustrative Examples of FDA-Approved Therapeutics Incorporating D-Aas. Gramicidins. Gramicidins are a family of peptide antibiotics produced by the soil bacterium *Brevibacillus brevis* (formerly *Bacillus brevis*). They represent some of the earliest clinically used antibiotics, discovered in 1939 during intensive research into soil microbes. The sequence of gramicidin A was elucidated in 1964 with the ion-channel dimer structure confirmed by nuclear magnetic resonance (NMR) spectroscopy in the 1970s–1990s [57].

Gramicidins occur in multiple natural variants produced non-ribosomally. Gramicidin D (the primary commercial form) is a mixture of linear pentadecapeptides (Fig. 2) gramicidin A (80%), B (5%), and C (15%). The general sequence is formyl-L-X-Gly-L-Ala-D-Leu-L-Ala-D-Val-L-Val-D-Val-L-Trp-D-Leu-L-Y-D-Leu-L-Trp-D-Leu-L-Trp-ethanolamide, where X is Val or Ile, and Y is Trp (A), Phe (B), or Tyr (C). Alternating D- and L-AAs enables formation of a right-handed β-helix. In lipid bilayers, two monomers associate head-to-head into a transmembrane channel ~2.6 nm long that selectively conducts monovalent cations (K^+, Na^+) [58].

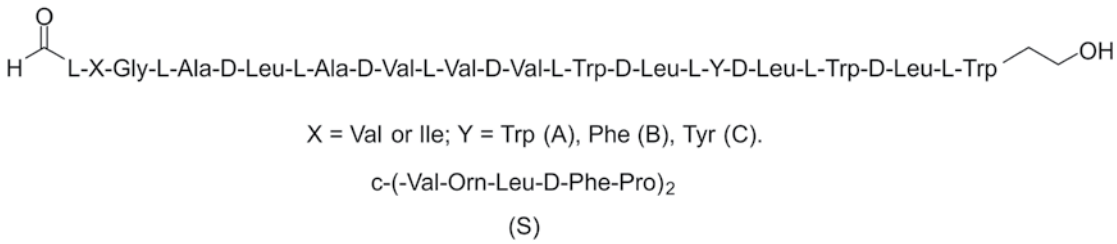

Fig. 2. Structures of gramicidins A, B, C, and S.

Gramicidin S is a distinct cyclic decapeptide: *cyclo*-(-Val-Orn-Leu-D-Phe-Pro)$_2$. It adopts an amphipathic antiparallel β-sheet conformation with a hydrophobic face (Val, Leu, D-Phe) and a positively charged ornithine face. This cyclic, symmetric structure differs markedly from the linear gramicidin D forms and confers broader membrane-disrupting activity [59].

As mentioned above, gramicidins are bactericidal ionophores or membrane disruptors. Linear gramicidin D forms cation-selective channels that collapse ion gradients, depolarize the membrane, and inhibit synthesis of adenosine triphosphate (ATP)—highly effective against Gram-positive bacteria (*Staphylococcus*, *Streptococcus*, *Bacillus*) but inactive against most Gram-negatives due to the outer membrane barrier. Gramicidin S inserts into bacterial membranes, increasing permeability and causing leakage of cellular contents. It shows activity against some Gram-negatives and fungi as well. Both are hemolytic and toxic to mammalian cells at higher concentrations, restricting use to topical applications. They exhibit rapid killing at low micromolar doses and low resistance potential because they target the lipid bilayer rather than a specific protein [60].

Owing to systemic toxicity (hemolysis, organ damage), gramicidins are used exclusively topically. Gramicidin D is formulated in ophthalmic solutions (often combined with neomycin and polymyxin B) for bacterial conjunctivitis, corneal ulcers, and external eye infections. It also appears in some skin/wound creams and throat lozenges. Gramicidin S has been applied for infected wounds, dental infections, and historically as a topical spermicide or treatment for genital ulcers. Veterinary use (e.g., in equine eye drops) is also common. They provide broad-spectrum coverage against Gram-positive pathogens in superficial infections where systemic antibiotics are unnecessary [61].

Gramicidins are produced by large-scale fermentation of *B. brevis* strains. Biosynthesis occurs via non-ribosomal peptide synthetases (NRPS): four large multimodular enzymes for linear forms and two (GrsA/GrsB) for the cyclic Gramicidin S, incorporating D-AAs and performing cyclization. The crude tyrothricin mixture is extracted, purified by chromatography or crystallization, and formulated into sterile ophthalmic drops, ointments, or creams. Production is well-established, cost-effective, and yields stable crystalline solids [62].

Gramicidin has long-standing FDA recognition as an active ingredient in approved combination products, e.g., neomycin/polymyxin B/gramicidin ophthalmic solution under Abbreviated New Drug Applications since the 1960s. It is listed in the FDA Orange Book for topical/ophthalmic use in superficial bacterial

infections. Gramicidins A-C and gramicidin S have not been granted new-drug approval for systemic administration or novel indications. Their use remains confined to traditional topical, multi-component preparations available by prescription or over the counter. The lack of recent FDA approvals highlights their mature, well-characterized profile as safe and effective topical antimicrobials [63].

Gramicidins exemplify early peptide antibiotics whose distinctive ion-channel-forming and membrane-disruptive activities remain clinically relevant for topical use, even though their intrinsic properties preclude systemic administration. Their discovery helped inaugurate the antibiotic era, and their unusual sequence architecture, most notably the incorporation of D-AAs that confer conformational rigidity, proteolytic stability, and defined channel geometry, continues to inspire contemporary research on membrane-active peptides. This combination of structural novelty and functional robustness underscores why gramicidins remain a foundational model for designing next-generation peptide therapeutics [57–63].

Cyclosporine. Cyclosporine (also known as ciclosporin or cyclosporine A, CsA) is a potent immunosuppressant and the prototype calcineurin inhibitor. It revolutionized organ transplantation and remains a cornerstone therapy for preventing graft rejection and treating certain autoimmune conditions [64].

Cyclosporine was first isolated in 1971 from the soil fungus *Tolypocladium inflatum* during routine screening for new antibiotics. A key breakthrough followed in 1972, when its potent immunosuppressive activity was identified in a functional screening assay, leading to further characterization of its selective T-cell–suppressive effects. The complete chemical structure was elucidated in 1976 (Fig. 3). Clinical efficacy in preventing organ rejection was subsequently demonstrated in kidney and liver transplantation, with the first patient receiving cyclosporine in 1980. The drug entered medical use after FDA approval in 1983 (as Sandimmune®) and is now included on the World Health Organization (WHO) List of Essential Medicines [65,66].

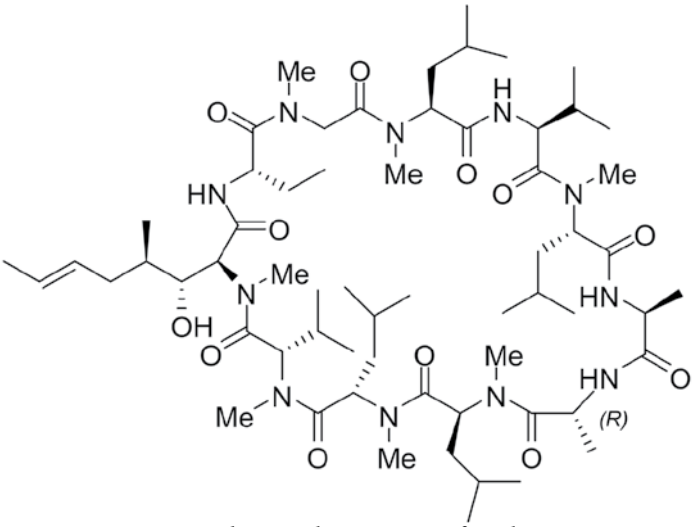

Fig. 3. Chemical structure of cyclosporine.

Cyclosporine is a cyclic undecapeptide (Fig. 3) produced non-ribosomally. It contains seven *N*-methylated amide bonds, which confer exceptional metabolic stability, high lipophilicity, and a 'chameleonic' conformational flexibility that enables membrane permeation despite its large size. The peptide includes several unusual residues, most notably the unique amino acid at position 1, (2*S*,3*R*,4*R*,6*E*)-3-hydroxy-4-methyl-2-(methylamino)-6-octenoic acid (MeBmt or Bmt), as well as sarcosine (*N*-methyl-glycine) and 2-aminobutyric acid (Abu). It also contains one single D-AA, i.e., D-Ala at position 8. The macrocycle is closed by a peptide bond, forming a highly stable 33-membered ring. This structural architecture enables cyclosporine to bind intracellular cyclophilin A. The resulting complex inhibits calcineurin, thereby blocking T-cell activation [66, 67].

As noted above, the FDA first approved cyclosporine (Sandimmune®) in 1983 for the prophylaxis of organ rejection in allogeneic kidney, liver, and heart transplantation. A microemulsion formulation with improved oral bioavailability (Neoral®) was subsequently approved. Ophthalmic emulsions (0.05%) for dry-eye disease (keratoconjunctivitis sicca) and additional topical formulations followed. Numerous generic versions are now available. In 2021, the structurally related analog voclosporin was also approved by the FDA [68].

Cyclosporine is a calcineurin inhibitor that selectively suppresses T-cell activation and proliferation by blocking interleukin-2 production. FDA-approved indications include: prevention of organ rejection in kidney, liver, and heart transplantation (typically in combination regimens); treatment of severe, recalcitrant plaque psoriasis in non-immunocompromised adults; rheumatoid arthritis inadequately controlled by methotrexate alone; and dry-eye disease, for which a 0.05% ophthalmic emulsion is approved for keratoconjunctivitis sicca associated with Sjögren's syndrome or meibomian gland dysfunction [69,70].

Additional or off-label uses include atopic dermatitis, ulcerative colitis, nephrotic syndrome, graft-versus-host disease, and certain veterinary applications (e.g., canine atopic dermatitis). Cyclosporine is administered primarily orally—with therapeutic drug monitoring due to its narrow therapeutic index—or topically; intravenous administration is reserved for specific situations. Major adverse effects include nephrotoxicity, hypertension, and an increased risk of infections and malignancies [70].

D-penicillamine. D-penicillamine is a chelating and disease-modifying therapeutic agent that has been used in medicine for several decades, particularly in the treatment of heavy metal poisoning, Wilson's disease, and certain autoimmune disorders. It is a degradation product of penicillin, although it does not possess antibiotic activity. Its discovery and therapeutic development represent an important example of how chemical derivatives of existing drugs can acquire entirely different medical applications [71].

D-penicillamine was first identified as a metabolite of penicillin during studies of penicillin degradation in the mid-20th century. Chemically, it is a dimethylated analog of the amino acid cysteine, containing a free sulfhydryl (-SH) group that gives it strong metal-binding properties (Fig. 4). This characteristic led to its recognition as an effective chelating agent capable of forming stable complexes with metals such as copper, lead, and mercury.

Its therapeutic importance became evident in the 1950s, when researchers discovered its ability to remove excess copper from the body, providing a breakthrough treatment for Wilson's disease [71-73].

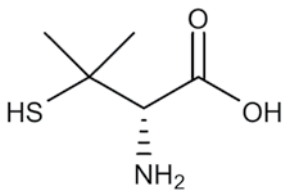

Fig. 4. Chemical structure of D-penicillamine.

The FDA approved D-penicillamine in the late 1950s and early 1960s for clinical use, and it was marketed under trade names such as Cuprimine® and Depen®. Its approval was particularly significant for Wilson's disease, as it became the first effective oral treatment for reducing copper accumulation and preventing severe liver and neurological damage [71–73].

Medically, D-penicillamine has three major therapeutic applications. The most important is in the treatment of Wilson's disease, a rare genetic disorder characterized by excessive copper accumulation in tissues, especially the liver and brain. By binding copper and promoting its urinary excretion, D-penicillamine helps reduce toxic copper levels and prevents disease progression [74-76].

A second important use is in the management of heavy metal poisoning, including lead and mercury intoxication. As a chelating agent, D-penicillamine binds toxic metals and facilitates their elimination from the body, although in many cases newer chelators are now preferred because of better safety profiles [72–76].

The third major use is in the treatment of severe rheumatoid arthritis, where D-penicillamine acts as a disease-modifying antirheumatic drug (DMARD). In rheumatoid arthritis, it helps reduce inflammation and slow joint damage, although its use has declined due to the availability of safer and more effective alternatives [71].

Additionally, D-penicillamine is used in the management of cystinuria, a hereditary disorder in which excessive cystine in the urine leads to recurrent kidney stone formation. The drug reacts with cystine to form a more soluble compound, thereby reducing stone formation.

Despite its effectiveness, D-penicillamine is associated with significant adverse effects, including skin reactions, bone marrow suppression, nephrotoxicity, and autoimmune complications such as drug-induced lupus. Because of these risks, its use requires careful medical supervision and regular monitoring [74].

D-Penicillamine is a remarkable example of a simple D-AA derivative produced by the chemical degradation of penicillin. This compound has emerged as a valuable therapeutic agent with key applications in heavy metal chelation and the treatment of autoimmune diseases. Its contribution to the management of Wilson's disease is especially noteworthy: introduced in the 1950s, it dramatically transformed a previously fatal inherited disorder into a treatable condition and remains an essential medicine in modern clinical practice.

Daptomycin. Daptomycin is a cyclic lipopeptide antibiotic and the first member of its class approved for clinical use. It represents a unique example of a complex molecule containing multiple D-AAs that exhibits potent bactericidal activity against Gram-positive bacteria, including methicillin-resistant *Staphylococcus aureus* (MRSA) and vancomycin-resistant *Enterococci* (VRE) [77].

Daptomycin was discovered in the late 1980s by researchers at Eli Lilly and Company from the soil actinomycete *Streptomyces roseosporus*. Early clinical development by Eli Lilly was halted due to concerns about skeletal muscle toxicity at high doses. In 1997, the rights were acquired by Cubist Pharmaceuticals, which optimized the dosing regimen (once-daily administration) to minimize toxicity while maintaining efficacy. Daptomycin was approved by the FDA in September 2003 under the brand name Cubicin® and has since become an important option for treating resistant Gram-positive infections [77-79].

Daptomycin is a 13-amino acid cyclic lipodepsipeptide (Fig. 5). It consists of a decanoyl fatty acid tail attached to the *N*-terminus of a linear tripeptide "handle", linked to a 10-amino acid macrocyclic core closed by an ester (lactone) bond: decanoyl-Trp^{1}-Asn^{2}-Asp^{3}-Thr^{4}-Gly^{5}-Orn^{6}-Asp^{7}-D-Ala^{8}-Asp^{9}-Gly^{10}-D-Ser^{11}-MeGlu^{12}-Kyn^{13} (10-residue lactone ring between Thr^{4} and Kyn^{13}). It contains three D-AAs (D-Asn at position 2, D-Ala at position 8, and D-Ser at position 11), as well as several non-proteinogenic amino acids including L-ornithine, (2*S*,3*R*)-3-methyl-L-glutamic acid, and kynurenine (Kyn) (2*S*)-2-amino-4-(2-aminophenyl)-4-oxobutanoic acid. The molecule is anionic and requires calcium ions (Ca^{2+}) for its membrane-inserting activity [78–80].

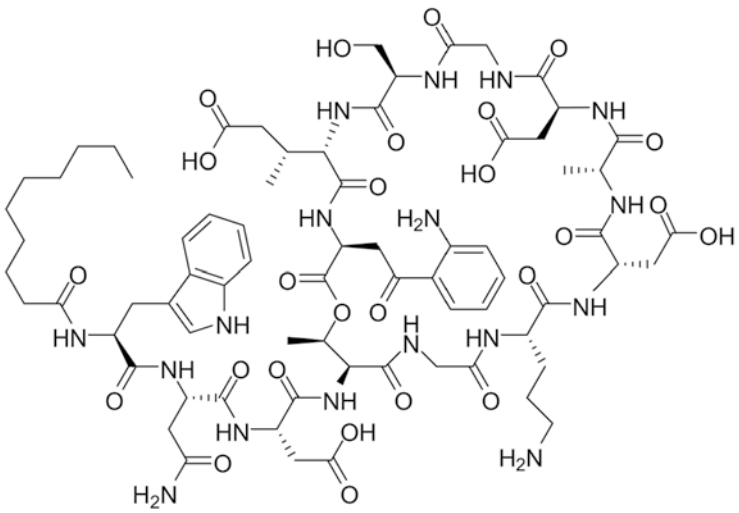

Fig. 5. Chemical structure of daptomycin.

As stated above, the FDA first approved daptomycin (Cubicin®) in 2003 for the treatment of complicated skin and skin structure infections (cSSSI) caused by susceptible Gram-positive bacteria. In 2006, the indication was expanded to include *Staphylococcus aureus* bloodstream infections (bacteremia), including right-sided infective endocarditis caused by methicillin-susceptible and methicillin-resistant isolates. It is also approved for pediatric patients (1–17 years) for cSSSI and bacteremia. A new formulation (Cubicin® RF) was later approved for improved stability and shorter infusion time [77–81].

Daptomycin exerts rapid, concentration-dependent bactericidal activity by binding to the bacterial cell membrane in a calcium-dependent manner, inserting its lipid tail, and causing rapid depolarization of the membrane potential. This leads to disruption of multiple membrane functions, potassium efflux, and ultimately bacterial cell death without significant lysis. It is primarily used for serious Gram-positive infections [82].

Daptomycin is produced commercially by submerged fermentation of *Streptomyces roseosporus*. It belongs to the A21978C family of lipopeptides and is biosynthesized by a large NRPS system. The fatty acid side chain is added by supplying decanoic acid (or its precursors) during fermentation to direct production toward the decanoyl derivative. After fermentation, the compound is extracted and highly purified. Strain improvement, precursor feeding, and metabolic engineering have been used to significantly increase yields for industrial production [77, 79, 81].

Daptomycin itself remains the only clinically approved member of this specific lipopeptide class for systemic use. Semisynthetic derivatives and analogs have been explored in research to improve activity, reduce toxicity, or expand the spectrum, but none have yet reached broad clinical approval. Minor natural variants produced by the same organism differ mainly in the length of the lipid tail and show reduced potency [82].

Etelcalcetide. Etelcalcetide (brand name: Parsabiv®) is a synthetic peptide calcimimetic agent and the first intravenous calcimimetic approved for clinical use. It is a unique example of a chirobiotic peptide composed almost entirely of D-AAs, designed to act as an allosteric agonist of the calcium-sensing receptor (CaSR). It is used for the treatment of secondary hyperparathyroidism (SHPT) in patients with chronic kidney disease (CKD) on hemodialysis [83, 84].

Etelcalcetide (originally known as AMG 416 or KAI-4169) was developed by Amgen (in collaboration with KAI Pharmaceuticals). It was designed as a novel, longer-acting chirobiotic alternative to the oral calcimimetic cinacalcet (Mimpara®). The compound entered clinical development in the early 2010s. Amgen submitted the New Drug Application to the FDA in 2015. It received approval from the European Medicines Agency (EMA) in November 2016 and from the FDA in February 2017 under the brand name Parsabiv® [83–85].

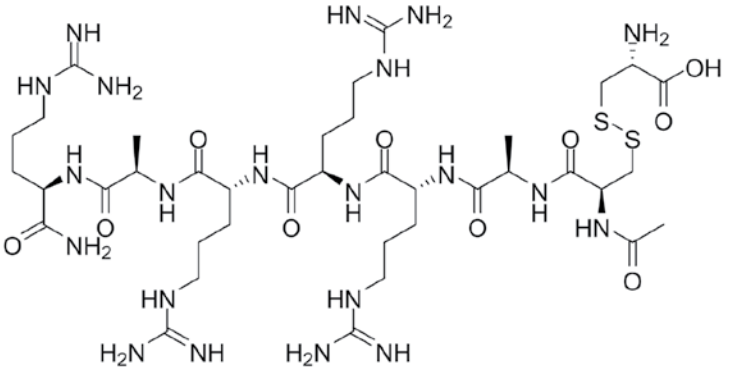

Fig. 6. Chemical structure of etelcalcetide.

Etelcalcetide is an 8-amino acid linear peptide with a disulfide linkage. It consists of a chain of seven D-AAs linked via a disulfide bond to an L-cysteine residue (Fig. 6).

The high content of D-AAs provides excellent proteolytic stability, allowing the chirobiotic peptide to remain active in circulation despite being a relatively small peptide [86].

Etelcalcetide (Parsabiv®) was approved in 2017 for the treatment of SHPT in adult patients with CKD on hemodialysis. It is administered as a bolus injection three times per week at the end of hemodialysis sessions. Etelcalcetide acts as a positive allosteric modulator (agonist) of the CaSR on the parathyroid glands. Activation of CaSR decreases the secretion of parathyroid hormone (PTH), lowers serum calcium and phosphorus levels, and helps control the mineral and bone disorder associated with CKD. It is indicated for secondary hyperparathyroidism in adult CKD patients on hemodialysis [86]. Unlike oral cinacalcet, etelcalcetide is given intravenously during dialysis, which improves adherence and ensures delivery in patients who have difficulty taking oral medications. Common side effects include hypocalcemia, nausea, vomiting, and muscle spasms. Serum calcium levels must be monitored closely [83–86].

Etelcalcetide is produced by chemical synthesis using solid-phase peptide synthesis (SPPS) technology. Because the molecule consists predominantly of D-AAs, it is assembled using protected D-AA building blocks. The disulfide bond is formed in a controlled oxidation step between the D-Cys and L-Cys residues. The final product is purified and converted to the hydrochloride salt for pharmaceutical use. As a synthetic peptide, it does not rely on fermentation or biological extraction [87, 88].

Difelikefalin. Difelikefalin (brand name: Korsuva™) is a synthetic tetrapeptide and a first-in-class, peripherally restricted kappa opioid receptor (KOR) agonist. It is a notable example of a peptide drug composed entirely of D-AAs, designed to selectively activate peripheral KORs while minimizing central nervous system penetration. It is approved for the treatment of moderate-to-severe pruritus (itch) associated with chronic kidney disease (CKD-aP) in adults undergoing hemodialysis [89, 90].

Difelikefalin (originally developed as CR845) was discovered and developed by Cara Therapeutics. The compound was engineered to create a potent and selective KOR agonist with minimal ability to cross the blood-brain barrier, thereby reducing the risk of centrally mediated side effects such as dysphoria or sedation commonly associated with traditional opioids. After successful Phase 3 clinical trials (KALM-1 and KALM-2), the FDA approved difelikefalin in August 2021 under the brand name Korsuva™, making it the first approved therapy specifically for chronic kidney disease-associated pruritus [89–90].

Difelikefalin is a tetrapeptide consisting of four D-AAs linked to a modified piperidine moiety (Fig. 7).

The exclusive use of D-AAs confers high resistance to proteolytic degradation, resulting in a favorable pharmacokinetic profile for intravenous administration. Difelikefalin was approved for the treatment of moderate-to-severe pruritus associated with chronic kidney disease (CKD-aP) in adults undergoing hemodialysis. It is administered as an intravenous bolus injection (0.5 mcg/kg) at the end of each hemodialysis session, typically three times per week. It has also received approval in several other countries, including the European Union and Australia [91].

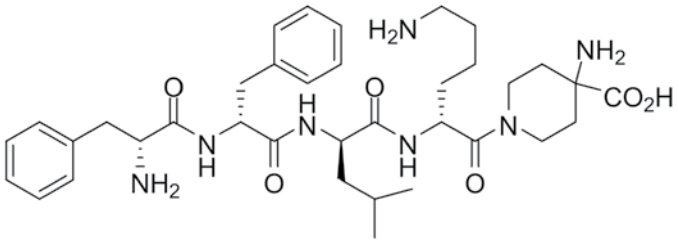

Fig. 7. Chemical structure of difelikefalin.

Difelikefalin selectively activates KORs located on peripheral sensory neurons and immune cells. This activation modulates itch signaling pathways without significant central opioid effects. It is the first and only FDA-approved treatment specifically indicated for CKD-associated pruritus, a condition that significantly impairs quality of life in hemodialysis patients. Clinical studies demonstrated significant reduction in itch intensity and improvement in itch-related quality of life compared to placebo. Common side effects include dizziness, somnolence, and paresthesia, which are generally mild to moderate. Because of its peripheral restriction, it has a lower risk of central side effects compared to non-selective opioids [92,93].

Difelikefalin is produced by chemical synthesis using SPPS. The peptide chain is assembled from protected D-AA building blocks, followed by coupling to the 4-aminopiperidine-4-carboxylic acid moiety. The final product is purified and formulated as a sterile solution for intravenous injection (often as the acetate salt). As a small synthetic peptide, it does not require biological fermentation or recombinant production [90-92].

Difelikefalin remains the only approved drug in its chirobiotic class. Oral formulations of Difelikefalin have been investigated for other indications such as postoperative pain and osteoarthritis pain but have not yet received broad regulatory approval. No major structural analogs are currently in late-stage clinical development.

Voclosporin. Voclosporin (brand name: Lupkynis®) is a semisynthetic cyclic undecapeptide and a next-generation calcineurin inhibitor. It is a structural analog of cyclosporine A with a modified side chain at the unique MeBmt residue. Voclosporin was specifically designed to offer improved potency, a more predictable pharmacokinetic profile, and potentially reduced nephrotoxicity compared to cyclosporine [94].

Voclosporin was developed by Isotechnika Pharma (later Aurinia Pharmaceuticals) in Edmonton, Canada. The molecule was created through a targeted chemical modification of cyclosporine A, replacing the MeBmt at position 1 with a modified amino acid containing a shorter unsaturated side chain. After successful Phase 2 and Phase 3 clinical trials (AURA-LV and AURORA), the FDA approved voclosporin in January 2021 under the brand name Lupkynis®, making it the first approved oral therapy for lupus nephritis in over a decade [94, 95].

Voclosporin is a cyclic undecapeptide (Fig. 8). It retains the core macrocyclic structure of cyclosporine A but features a modified side chain at position 1. The molecule contains seven *N*-methylated amide bonds and one D-AA (D-Ala at position 8), which contribute to its metabolic stability and membrane permeability [96].

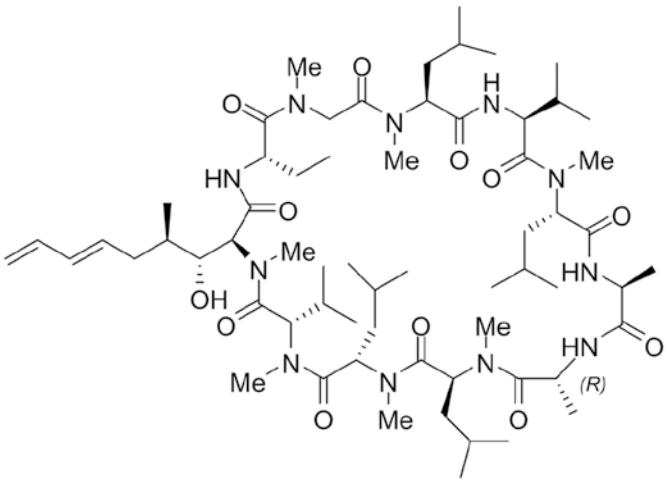

Fig. 8. Chemical structure of voclosporin.

The FDA approved voclosporin (Lupkynis®) for the treatment of adult patients with active lupus nephritis (LN), in combination with background immunosuppressive therapy (typically mycophenolate mofetil and low-dose corticosteroids). It is currently the only approved calcineurin inhibitor specifically indicated for LN [94,95].

Voclosporin acts as a calcineurin inhibitor by binding to cyclophilin A, forming a complex that inhibits the phosphatase activity of calcineurin. This prevents dephosphorylation of nuclear factor of activated T-cells (NFAT), thereby suppressing T-cell activation and interleukin-2 production. It is primarily used for active LN (Class III, IV, or V) in combination with standard-of-care therapy [97].

Voclosporin offers a more consistent pharmacokinetic profile and a narrower therapeutic index than cyclosporine, allowing for more predictable dosing with therapeutic drug monitoring. Common side effects include hypertension, nephrotoxicity, tremor, and increased infection risk. Regular monitoring of renal function and blood pressure is essential [98].

Voclosporin is produced by semisynthetic modification of cyclosporine A. The process begins with fermentation-derived cyclosporine A, followed by selective chemical transformation of the MeBmt side chain at position 1 to introduce the shorter unsaturated chain. The final product is purified by chromatography and formulated into soft-gelatin capsules for oral administration. This semisynthetic route is significantly more efficient than total chemical synthesis of the entire 11-residue macrocycle [96].

Voclosporin is currently the only approved derivative of cyclosporine specifically optimized for LN. Other experimental analogs of cyclosporine (such as alisporivir) have been investigated for antiviral indications but have not reached approval for autoimmune diseases.

Synthesis

The development of efficient, scalable, and environmentally sustainable synthetic methodologies for D-AAs is no longer a niche academic pursuit but a strategic necessity in pharmaceutical science. Continued innovation in asymmetric synthesis [99-108], biocatalysis

[109–115], and chemoenzymatic approaches [116–120] will be crucial to unlocking the full therapeutic potential of D-AA-containing peptides and to meeting the growing needs of the peptide drug pipeline. As the field of peptide therapeutics advances toward more stable, selective, and orally bioavailable candidates, robust access to diverse D-AAs will remain a cornerstone of future drug discovery and development.

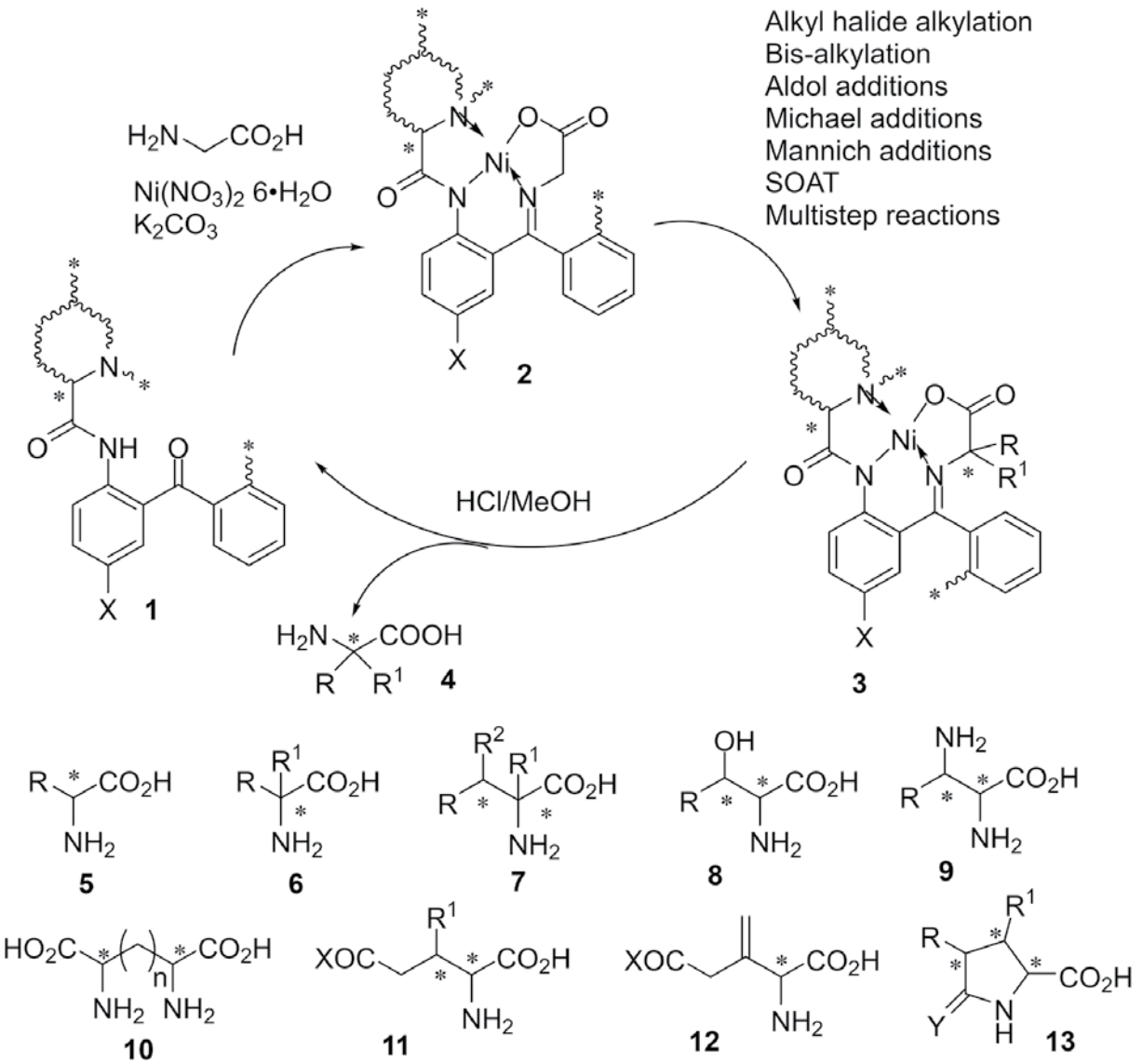

Scheme 1. General application of chiral Ni(II) complexes for asymmetric synthesis of tailor-made amino acids.

The Ni(II) complexes of amino acid Schiff bases (Scheme 1) represent one of the most powerful and versatile general methodologies for the asymmetric synthesis of tailor-made α-amino acids [121–23]. In its most general form, as depicted in Scheme 1, this approach utilizes ligands **1** bearing a chiral auxiliary on the amino acid fragment, which are condensed with o-benzophenone or its derivatives. Ligand **1** is subsequently transformed into the corresponding Ni(II) complex **2** by reaction with glycine under basic conditions in the presence of Ni(II) ions. The Ni(II) ion serves a dual role: as a template that rigidly organizes the molecule and as a Lewis acid that dramatically increases the acidity of the α-hydrogen of the coordinated glycine. This enables highly stereoselective transformations at the α-position, including alkylation, dialkylation, aldol, Michael, and Mannich additions, as well as other C–C bond-forming reactions, under mild conditions. After the reaction, the products **3** can be readily disassembled under acidic conditions to release the enantiomerically enriched tailor-made amino acid **4**, while the chiral auxiliary is typically recovered and reused. Thanks to its high diastereoselectivity, operational simplicity, scalability, and broad substrate scope, the Ni(II)-complex methodology has become a widely adopted strategy for the preparation of structurally diverse, non-proteinogenic, and isotopically labeled α-amino acids required in modern medicinal chemistry and peptide drug development [121-123].

For example, amino acids of type **5** bearing virtually any substituents or functional groups on the side chain R can be readily prepared via alkylation of the Ni(II) glycine Schiff base complex with alkyl halides [124–127]. This methodology can be further extended to the synthesis of α,α-dialkyl-substituted amino acids **6** [128–131]. The approach also works efficiently with secondary alkyl halides, providing access to highly sterically hindered amino acids **7** containing both α- and β-stereogenic centers [132,133]. Additionally, the use of α,ω-dihaloalkanes enables the preparation of bis-amino acids of type **10** [134, 135]. β-Hydroxy amino acids **8** [136–138] and β-amino derivatives **9** [139, 140] are accessible through aldol and Mannich addition reactions, respectively. The Michael addition reaction of glycine Schiff base complex **2** [141–143] is particularly versatile, allowing the synthesis of a wide range of glutamic acid derivatives **11** [144–146], including β-methylene analogs **12** [147], as well as highly substituted pyroglutamates [148-150] and prolines **13** [151, 152]. Furthermore, multistep sequences employing these Schiff base complexes facilitate the preparation of more structurally complex targets, such as thalidomide derivatives [153-155], oxazolomycin and neooxazolomycin analogs [156], the AHOD (3-amino-2-hydroxy-octadecanoic acid) moiety of ralstonin A [157], and various derivatives of 1-amino-2-vinyl-cyclopropanecarboxylic acid [158–160].

Creative efforts in the structural design of ligands **1** [161–163] have led to the development of a new generation of chiral auxiliaries. These include derivatives featuring planar chirality **14** [164–166], (Fig. 9), axial chirality **15** [167, 168], and N–H-containing ligands **16** with a stereogenic nitrogen center [169–171]. Among the most practical and versatile structures is the Ni(II) complex **17** [172–174], which bears three strategically positioned chlorine atoms that enhance both reactivity and stereoselectivity. Notably, Ni(II) complexes **14** and **17** have proven particularly effective for the large-scale preparation of D-AAs.

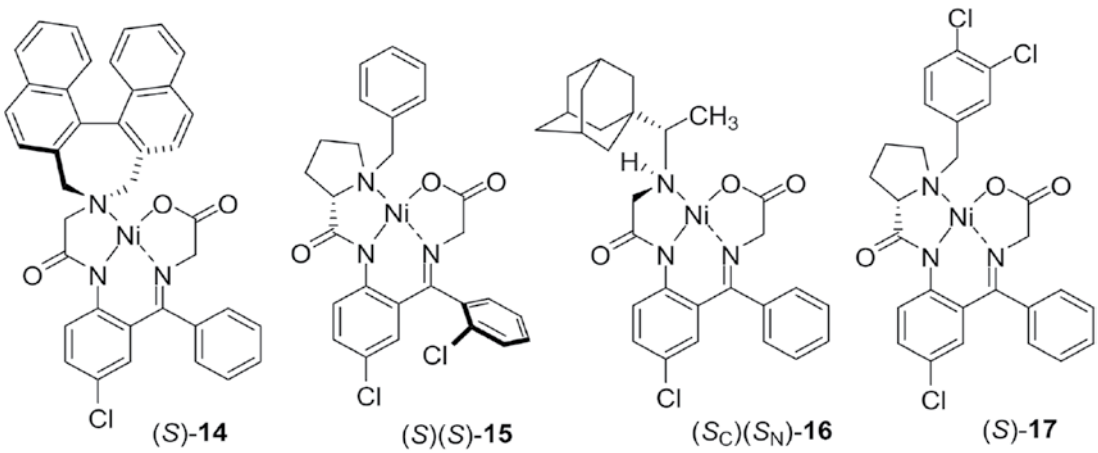

Fig. 9. New generation of chiral Ni(II) complexes.

D-AAs can be efficiently prepared via the Ni(II) Schiff base methodology using either L-to-D interconversion or deracemization strategies [175-177]. This allows the conversion of readily available L-AAs into their D-configured enantiomers or the direct transformation of inexpensive racemic (L/D) mixtures into the desired D-AAs with high selectivity [178-180]. As illustrated in Scheme 2, the planar chiral ligand **18** is reacted with an L-AA or its racemic counterpart to form the corresponding Ni(II) Schiff base complex **19**. The (*S*)-configuration of the chiral amine moiety in the ligand strongly favors (>95% diastereoselectivity) the formation of the D-configured amino acid. The resulting complex **19** is typically isolated by filtration and then disassembled under mild acidic conditions (aqueous HCl) to liberate the free D-AA while allowing recovery of the chiral ligand **18** [181–183]. Because the planar chirality of ligand **18** remains stable under the reaction conditions, it can be recovered and reused over multiple cycles without loss of performance. Owing to its high efficiency, excellent recyclability, and operational simplicity, this Ni(II) methodology is often more economically attractive than many catalytic approaches. It has been successfully scaled up to kilogram-scale production of various D-AAs.

Conclusions. In summary, the strategic incorporation of D-AAs has fundamentally transformed peptide therapeutics, converting inherently fragile and rapidly degraded biologics into stable, drug-like chirobiotic molecules with enhanced pharmacokinetic profiles, improved target specificity, and prolonged duration of action. This approach has significantly broadened the therapeutic utility of peptides across multiple therapeutic areas, including infectious diseases, metabolic disorders, oncology, autoimmune conditions, nephrology, and neurology. The evolution of D-AA–containing pharmaceuticals reflects more than seven decades of progress, from the early clinical use of gramicidin D in 1955 to modern approved drugs such as cyclosporine, daptomycin, etelcalcetide, difelikefalin, voclosporin, and others. This remarkable journey highlights the critical role of molecular chirality in drug dis-

covery and development. Advances in asymmetric synthesis, particularly Ni(II) Schiff base methodologies, computational design, mirror-image phage display, and peptidomimetic engineering have enabled the creation of increasingly sophisticated D-AA-rich peptides and macrocycles that were previously inaccessible. These innovations have delivered tangible clinical benefits, offering new treatment options for conditions with historically limited therapies, such as CKD-aP, LN, and rare complement-mediated disorders. By enhancing proteolytic stability and membrane permeability while reducing immunogenicity, D-AAs have helped bridge the gap between promising peptides and successful marketed drugs. Nevertheless, challenges remain. High manufacturing costs, potential off-target effects, and the need for specialized synthetic expertise continue to limit broader application. To fully unlock the potential of this class, future efforts should prioritize scalable and sustainable production methods, deeper structure–activity relationship studies, and the development of next-generation delivery systems. Overall, D-AA–containing chirobiotics exemplify how precise stereochemical design continues to drive innovation in pharmaceutical science. As synthetic methodologies mature and our understanding of peptide pharmacology deepens, D-AA strategies are poised to play an increasingly central role in the development of safer, more effective, and longer-lasting therapeutic agents for a wide range of human diseases.

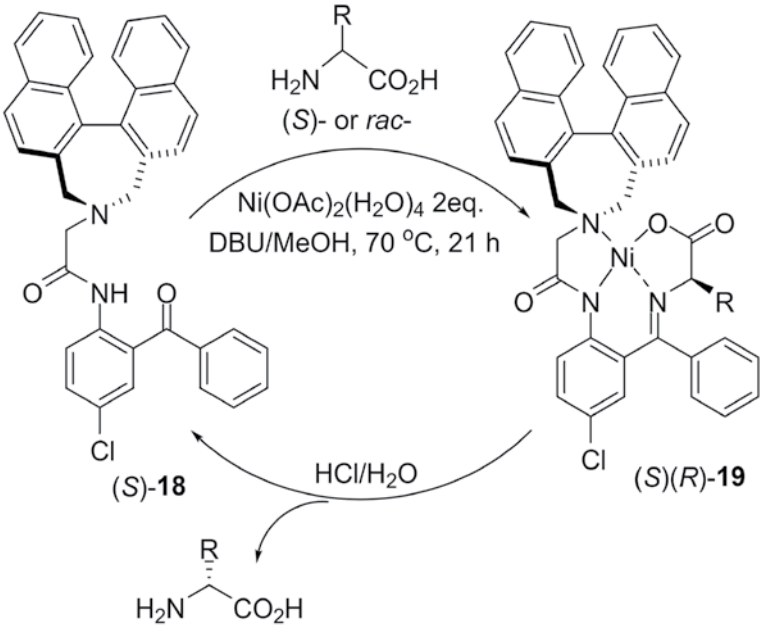

Scheme 2. Procedure for the preparation of D-AAs.

AUTHORS' CONTRIBUTION. All authors have read the research results and approved the final version of the manuscript.

CONFLICT OF INTEREST. The authors declare no conflict of interest.

ACKNOWLEDGMENTS. During the preparation of this work, the authors used Google Gemini to facilitate the Ukrainian translation. The authors reviewed and edited the output as needed and take full responsibility for the content of the publication.

ЗАСТОСУВАННЯ D-АМІНОКИСЛОТ У ДИЗАЙНІ ЛІКАРСЬКИХ ЗАСОБІВ (огляд)

Аліція Взорек,[1] Таїзо Оно,[2] Даніель Беккер,[3] Вей Чжан,[4] Хіроїкі Морівакі[5], Кунісуке Ізава[5], Хіройукі Конно[6], Вадим А. Солошонок[2,7]*

[1] Хімічний інститут, Університет Яна Кохановського в Кельці, вул. Університетська 7, 25-406 Кельце, Польща;
[2] Національний інститут передової науки та технологій (AIST), 2266-98, Анагахора, Шімошідамі, район Моріяма, Нагоя, 463-8560, Японія;
[3] Відділ фармацевтичної та лікарської хімії, Фармацевтичний інститут, Вільний університет Берліна, Кьонігін-Луїзе-Штрасе 2+4, 14195 Берлін, Німеччина;
[4] Хімічний факультет, Університет Массачусетса в Бостоні, Бостон, Массачусетс 02125, Сполучені Штати;
[5] Hamari Chemical Ltd., Осака, Японія;
[6] Департамент хімії та біологічної інженерії, Аспірантура наук та інженерії, Університет Ямагата, 992-8510 Йонедзава, Ямагата, Японія;
[7] ІКЕРБАСКЕ, Баскська наукова фундація, вул. Марія Діас де Харо 3, Площа Бізкая, 48013 Більбао, Іспанія
E-mail: vadimsoloshonok@gmail.com

Присвята
Професору Таміо Хаяші – титану асиметричного каталізу, Полярній зірці в науці, чиє мудре керівництво стало для багатьох поколінь хіміків найформативнішим інтелектуальним досвідом.

D-амінокислоти стали незамінними будівельними блоками в сучасному дизайні пептидних лікарських засобів. Незважаючи на їхню відносну рідкісність у вищих організмах, D-амінокислоти є досить поширеними в природі, зокрема в бактеріальних пептидогліканах та мікробних антимікробних пептидах, де вони забезпечують протеолітичну стабільність і унікальну біологічну активність. Натхненні цими природними стратегіями, медичні хіміки успішно впровадили D-амінокислоти в синтетичні пептиди, щоб подолати притаманні обмеження традиційних пептидних препаратів, такі як швидка ферментативна деградація та низька біодоступність. Включення D-амінокислот пропонує низку ключових переваг, зокрема суттєво підвищену стійкість до протеолізу, подовжений період напіввиведення з плазми, знижену імуногенність та покращену селективність до рецепторів. Ці властивості дозволили розробити клінічно успішні препарати в багатьох терапевтичних галузях. Серед помітних прикладів – ранній антибіотик граміцидин D (1955), імуносупресивний агент циклоспорин, D-пеніциламін, даптоміцин, етелькальцетид, дифелікфалін та воклоспорин. Ці сполуки яскраво демонструють трансформаційний вплив D-амінокислот на пептидну фармакологію та їхню зростаючу роль у лікуванні інфекційних захворю-

вань, аутоімунних розладів, нефрологічних станів та багатьох інших патологій. Цей огляд висвітлює стратегічну важливість D-амінокислот у фармацевтичному дизайні, їхнє природне походження, клінічне застосування та значні досягнення в синтетичних методологіях з особливим акцентом на універсальний підхід на основі комплексів Шиффа Ni(II) для отримання tailor-made D-амінокислот. Еволюція лікарських засобів, що містять D-амінокислоти, демонструє, як стереохімічне конструювання продовжує стимулювати інновації у відкритті та розробленні пептидних препаратів.

Ключові слова: D-амінокислоти, хіральність, хіробіотики, комплекси Ni(II), дизайн лікарських засобів, протеолітична стабільність, пептидні терапевтичні засоби, лікарські препарати, що вийшли на ринок.

REFERENCES

[1] Daniel I., Oger P., Winter R. Origins of life and biochemistry under high-pressure conditions. *Chem. Soc. Rev*. 2006. **35**(10): 858–875. https://doi.org/10.1039/b517766a .

[2] Fujii N., Saito T. Homochirality and life. *Chem. Rec*. 2004. **4**(5): 267–278. https://doi.org/10.1002/tcr.20020 .

[3] Meierhenrich U.J. Amino acids and the asymmetry of life. *Europ. Rev*. 2013. **21**(2): 190–199. https://doi.org/10.1017/S106279871200035X.

[4] Keszthelyi L. Origin of the homochirality of biomolecules. *Quart. Rev. Bioph*. 1995. **28**(4): 473–507. https://doi.org/10.1017/S0033583500003309.

[5] Shepherd N.E., Hoang H.N., Abbenante G., Fairlie D.P. Left-and right-handed alpha-helical turns in homo-and hetero-chiral helical scaffolds. *J. Am. Chem. Soc*. 2009. **131**(43): 15877–15886. https://doi.org/10.1021/ja9065283 .

[6] Mazzier D., De S., Wicher B. *et al*. Parallel Homochiral and Anti-Parallel Heterochiral Hydrogen-Bonding Interfaces in Multi-Helical Abiotic Foldamers. *Angew. Chem. In. Ed*. 2020. **59**(4): 1606–1610. https://doi.org/10.1002/anie.201912805 .

[7] Hazari A., Sawaya M.R., Vlahakis N *et al*. The rippled β-sheet layer configuration — a novel supramolecular architecture based on predictions by Pauling and Corey. Chem. Scien. 2022. **13**(31): 8947–8952. https://doi.org/10.1039/D2SC02531K .

[8] Ikai T., Shimizu S., Awata S., Shinohara K.I. Chiral Amplification in π-Conjugated Helical Polymers with Circularly Polarized Luminescence. *Macromol*. 2018. **51**(6): 2328–2334. https://doi.org/10.1021/acs.macromol.8b00229 .

[9] Maeda K., Yashima E. Dynamic Helical Structures: Detection and Amplification of Chirality. In: Crego-Calama, M., Reinhoudt, D.N. (eds) Supramolecular Chirality. Topics in Current Chemistry, vol 265. Springer, Berlin, Heidelberg. 2006 Mar 9:47–88. https://doi.org/10.1007/128_035 .

[10] Sorochinsky A.E., Soloshonok V.A. Self-disproportionation of Enantiomers of Enantiomerically Enriched Compounds. In: Schurig, V. (eds) Differentiation of Enantiomers II. Topics in Current Chemistry, vol 341. Springer, Cham. 2013 Apr 19:301–339. https://doi.org/10.1007/128_2013_434 .

[11] Han J., Wzorek A., Klika K.D., Soloshonok V.A. Recommended tests for the self-disproportionation of enantiomers (SDE) to ensure accurate reporting of the stereochemical outcome of enantioselective reactions. *Molecules*. 2021. **26**(9): 2757. https://doi.org/10.3390/molecules26092757.

[12] Han J., Wzorek A., Soloshonok V.A., Klika K.D. The self-disproportionation of enantiomers (SDE): The effect of scaling down,

potential problems versus prospective applications, possible new occurrences, and unrealized opportunities? *Electrophoresis*. 2019. **40**(15): 1869–1880. https://doi.org/10.1002/elps.201800414 .

[13] Du Y., Bian Y., Baecker D. *et al*. Fluorine in the Pharmaceutical Industry: FDA-Approved Fluorine-Containing Drugs in 2024. *Chem. Eur. J*. 2025. e202500662. https://doi.org/10.1002/chem.202500662 .

[14] Wang Q., Bian Y., Dhawan G. *et al*. FDA approved fluorine-containing drugs in 2023. *Chin. Chem. Lett*. 2024. **35**(11): 109780. https://doi.org/10.1016/j.cclet.2024.109780 .

[15] Han J., Wzorek A., OnoT. *et al*. Modern pharmaceutical drugs featuring aliphatic fluorine-containing groups. *Ukr. Chem. J*. 2025. **91**(6): 15–54. https://doi.org/10.33609/2708-129X.91.6.2025.15-54 .

[16] Han J., Wzorek A., Dhawan G. *et al*. Chiral, Fluorine-containing Pharmaceuticals. *Ukr. Chem. J*. 2025. **91**(2): 55–90. https://doi.org/10.33609/2708-129X.91.2.2025.55-90 .

[17] Wzorek A., Han J., Ono T. *et al*. Synthesis of Tailor-Made Amino Acids Containing C(sp2)–F bonds. *Ukr. Chem. J*. 2025. **91**(8): 36–64. https://doi.org/10.33609/2708-129X.91.8.2025.36-64 .

[18] Kawai M., Nagai U. Comparison of conformation and antimicrobial activity of synthetic analogs of gramicidin S: Stereochemical consideration of the role of D-phenylalanine in the antibiotic. *Biopol. Orig. Res. Biomol*. 1978. **17**(6): 1549–1565. https://doi.org/10.1002/bip.1978.360170613 .

[19] Řeháček Z., De-xiu Z. The biochemistry of cyclosporin formation: a review. *Proc. Biochem*. 1991. **26**(3): 157–166. doi.org/10.1016/0032-9592(91)80012-E.

[20] Abe H., Yoshikawa N., Sarower M.G., Okada S. Physiological function and metabolism of free D-alanine in aquatic animals. *Biol. Pharma. Bull*. 2005. **28**(9): 1571–1577. https://doi.org/10.1248/bpb.28.1571 .

[21] Armstrong D.W., Berthod A. Occurrence of D-amino acids in natural products. *Nat. Prod. Bioprospec*. 2023. **13**(1): 47. https://doi.org/10.1007/s13659-023-00412-0 .

[22] Fujii N. D-amino acids in living higher organisms. *Orig. Life Evol. Biosph*. 2002. **32**(2): 103–127. https://doi.org/10.1023/A:1016031014871 .

[23] MacKay M.A., Kravtsenyuk M., Thomas R. *et al*. D-Serine: potential therapeutic agent and/or biomarker in schizophrenia and depression? Front. Psych. 2019. **10**: 25. https://doi.org/10.3389/fpsyt.2019.00025 .

[24] Kalíková K., Šlechtová T., Tesařová E. Enantiomeric ratio of amino acids as a tool for determination of aging and disease diagnostics by chromatographic measurement. *Separations*. 2016. **3**(4): 30. https://doi.org/10.3390/separations3040030.

[25] Marcone G.L., Rosini E., Crespi E., Pollegioni L. D-amino acids in foods. *App. Microbio. Biotech*. 2020. **104**(2): 555–574. https://doi.org/10.1007/s00253-019-10264-9.

[26] Liu A., Han J., Nakano A. *et al.* New pharmaceuticals approved by FDA in 2020: Small-molecule drugs derived from amino acids and related compounds. *Chirality.* 2022. **34**(1): 86–103. https://doi.org/10.1002/chir.23376 .

[27] Yin Z., Hu W., Zhang W. *et al.* Tailor-made amino acid-derived pharmaceuticals approved by the FDA in 2019. *Amino Acids.* 2020. **52**(9): 1227–1261. https://doi.org/10.1007/s00726-020-02887-4 .

[28] Liu J., Han J., Izawa K. *et al.* Cyclic tailor-made amino acids in the design of modern pharmaceuticals. *Eur. J. Med. Chem.* 2020. **208**: 112736. doi: 10.1016/j.ejmech.2020.112736.

[29] Han J., Konno H., Sato T. *et al*. Tailor-made amino acids in the design of small-molecule

blockbuster drugs. *Eur. J. Med. Chem.* 2021. **220**: 113448. https://doi.org/10.1016/j.ejmech.2021.113448.

[30] Han J., Konno H., Sato T. *et al.* Peptidomimetics and Peptide-Based Blockbuster Drugs. *Curr. Org. Chem.* 2021. **25**(14): 1627–1658. https://doi.org/10.2174/1385272825666210610155047 .

[31] Farhadi T., Hashemian S.M. Computer-aided design of amino acid-based therapeutics: A review. *Drug Des. Develop. Therapy*. 2018. **14**: 1239–1254. https://doi.org/10.2147/DDDT.S159767 .

[32] Sharma K.K., Sharma K., Rao K. *et al*. Unnatural amino acids: strategies, designs, and applications in medicinal chemistry and drug discovery. *J. Med. Chem*. 2024. **67**(22): 19932–1965. https://doi.org/10.1021/acs.jmedchem.4c00110 .

[33] Vig B.S., Huttunen K.M., Laine K., Rautio J. Amino acids as promoieties in prodrug design and development. *Adv. Drug Del. Rev*. 2013. **65**(10): 1370–1385. https://doi.org/10.1016/j.addr.2012.10.001 .

[34] Wang Q., Han J., Sorochinsky A. *et al.* The Latest FDA-Approved Pharmaceuticals Containing Fragments of Tailor-Made Amino Acids and Fluorine, *Pharmaceuticals*. 2022. **15**: 999. https://doi.org/10.3390/ ph15080999 .

[35] Wang N., Mei H., Dhawan G. *et al*. New Approved Drugs Appearing in the Pharmaceutical Market in 2022, Featuring Fragments of Tailor-Made Amino Acids and Fluorine, *Molecules*. 2023. **28**: 3651. https://doi.org/10.3390/molecules28093651.

[36] Han J., Wzorek A. Dhawan G. *et al.* New drugs on the pharmaceutical market containing fluorine and residues of tailor-made amino acids. *Ukr. Chem. J.* 2024. **90**(9): 31–56. https://doi.org/10.33609/2708-129X.90.9.2024.31-56.

[37] Han J., Wzorek A., Dhawan G. *et al.* New drugs appearing on the market in 2023: molecules containing fluorine and fragments of tailor-made amino acids. *Ukr. Bioorg. Acta.* 2024. **19**(1): 3–20. https://doi.org/10.15407/bioorganica2024.01.003.

[38] Yu Y., Liu A., Dhawan G. *et al.* Fluorine-containing pharmaceuticals approved by the FDA in 2020: Synthesis and biological activity. *Chin. Chem. Lett.* 2021. **32**(11): 3342–3354. https://doi.org/10.1016/j.cclet.2021.05.042 .

[39] Wang Q., Bian Y., Abouchabaka E. *et al*. Fluorine-containing drugs approved by the US FDA in 2025. *Chin. Chem. Lett*. 2026. **20**: 112640. https://doi.org/10.1016/j.cclet.2026.112640 .

[40] Bomb K., Zhang Q., Ford E.M. *et al*. Systematic d-amino acid substitutions to control peptide and hydrogel degradation in cellular microenvironments. *ACS Macro Lett*. 2023. **12**(6): 725–732. https://doi.org/10.1021/acsmacrolett.3c00144.

[41] Soloshonok V.A., Kirilenko A.G., Fokina N.A. et al. Biocatalytic Resolution of b-Fluoroalkyl-b-Amino Acids, *Tetrahedron: Asym*. 1994. **5**. 1119–1126. https://doi.org/10.1016/0957-4166(94)80063-4.

[42] Rezende S.B., Oshiro K.G., Júnior N.G. *et al.* Advances on chemically modified antimicrobial peptides for generating peptide antibiotics. *Chem. Commun*. 2021. **57**(88): 11578–11590. https://doi.org/10.1039/d1cc03793e .

[43] Rai J. Peptide and protein mimetics by retro and retroinverso analogs. *Chem. Biol. Drug Des*. 2019. **93**(5): 724–736. https://doi.org/10.1111/cbdd.13472 .

[44] Pohl E.H., Heine A.N., Sheldrick G.M. *et al.* Structure of octreotide, a somatostatin analogue. *Biol. Crystal*. 1995. **51**(1): 48–59. https://doi.org/10.1107/S0907444994006104 .

[45] Sabatine M.S. PCSK9 inhibitors: clinical evidence and implementation. *Nature Rev*.

Cardiol. 2019. **16**(3): 155–165. https://doi.org/10.1038/s41569-018-0107-8 .

[46] Chen S., Gfeller D., Buth S.A. *et al*. Improving binding affinity and stability of peptide ligands by substituting glycines with d-amino acids. *Chembiochem*. 2013. **14**(11): 1316–1322. https://doi.org/10.1002/cbic.201300228.

[47] Sugio S., Petsko G.A., Manning J.M. *et al*. Crystal structure of a D-amino acid aminotransferase: how the protein controls stereoselectivity. *Biochemistry*. 1995. **34**(30): 9661–9669. https://doi.org/10.1021/bi00030a002 .

[48] Krishnamoorthy G., Selvakumar R., Sastry T.P. *et al*. Effect of D-amino acids on collagen fibrillar assembly and stability: Experimental and modelling studies. *Biochem. Eng. J*. 2013. **75**: 92–100. https://doi.org/10.1016/j.bej.2013.04.002 .

[49] Seia M., Zisman E. Different roles of D-amino acids in immune phenomena. *FASEB J*. 1997. **11**(6): 449–456. https://doi.org/10.1096/fasebj.11.6.9194525 .

[50] Li H., Anuwongcharoen N., Malik A.A. *et al*. Roles of d-amino acids on the bioactivity of host defense peptides. *Int. J. Mol. Scien*. 2016. **17**(7): 1023. https://doi.org/10.3390/ijms17071023 .

[51] Sanchez Jr. C.J., Akers K.S., Romano D.R. *et al*. D-amino acids enhance the activity of antimicrobials against biofilms of clinical wound isolates of Staphylococcus aureus and Pseudomonas aeruginosa. *Antimicrob. Agents Chemother*. 2014. **58**(8): 4353–4361. https://doi.org/10.1128/aac.02468-14 .

[52] Caldwell M., Hughes M., Wei F. *et al*. Promising applications of D-amino acids in periprosthetic joint infection. *Bone Res*. 2023. **11**(1): 14. https://doi.org/10.1038/s41413-023-00254-z .

[53] Shi Y., Hussain Z., Zhao Y. Promising application of D-amino acids toward clinical therapy. *Int. J. Mol. Scien*. 2022. **23**(18): 10794. https://doi.org/10.3390/ijms231810794 .

[54] Sasabe J., Suzuki M.. Emerging role of D-amino acid metabolism in the innate defense. *Front. Microbiol*. 2018. **9**: 933. https://doi.org/10.3389/fmicb.2018.00933 .

[55] Ravibaskar K., Ganguly A., Roy Barman S. From Amino Acids to Proteins: Biomolecular Nanostructures as Closed-Loop Platforms for Tissue Engineering and Drug Delivery. *ACS Nanoscien. Au*. 2025. **6**(1): 1–20. https://doi.org/10.1021/acsnanoscienceau.5c00108 .

[56] Chen M., Zhang S., He Z. Controlled block polypeptide composed of d-type amino acids: a therapeutics delivery platform to inhibit biofilm formation of drug-resistant bacteria. *ACS App. Biomater*. 2020. **3**(9): 6343–6350. https://doi.org/10.1021/acsabm.0c00795 .

[57] Takada Y., Itoh H., Paudel A. *et al*. Discovery of gramicidin A analogues with altered activities by multidimensional screening of a one-bead-one-compound library. *Nature Commun*. 2020. **11**(1): 4935. https://doi.org/10.1038/s41467-020-18711-2 .

[58] Andersen O.S. Gramicidin channels. *Ann. Rev. Physiol*. 1984. **46**(1): 531–548. https://doi.org/10.1146/annurev.ph.46.030184.002531 .

[59] Guan Q., Huang S., Jin Y. *et al*. Recent advances in the exploration of therapeutic analogues of gramicidin S, an old but still potent antimicrobial peptide. *J Med. Chem*. 2019. 62(17): 7603–7617. https://doi.org/10.1021/acs.jmedchem.9b00156 .

[60] Durand G.A., Raoult D., Dubourg G. Antibiotic discovery: history, methods and perspectives. *Int. J. Antimicrob. Agents*. 2019. **53**(4): 371–382. https://doi.org/10.1016/j.ijantimicag.2018.11.010 .

[61] Pavithrra G., Rajasekaran R. Gramicidin peptide to combat antibiotic resistance: a review. *Int. J. Pep. Res. Therap*. 2020. **26**(1): 191–199.

https://doi.org/10.1007/s10989-019-09828-0.
[62] Blanch H.W., Rogers P.L. Optimal conditions for gramicidin S production in continuous culture. *Biotech. Bioengineer*. 1972. **14**(2): 151–171. https://doi.org/10.1002/bit.260140202.
[63] Das P., Delost M.D., Qureshi M.H. *et al*. A survey of the structures of US FDA approved combination drugs. *J. Med. Chem*. 2018. **62**(9): 4265–4311. https://doi.org/10.1021/acs.jmedchem.8b01610.
[64] Tedesco D., Haragsim L. Cyclosporine: a review. *J. Transplant*. 2012. 230386. https://doi.org/10.1155/2012/230386.
[65] Kahan B.D. Cyclosporine. *New Eng. J. Med*. 1989. **321**(25): 1725–1738. https://doi.org/10.1056/NEJM198912213212507.
[66] Ptachcinski R.J., Burckart G.J., Venkataramanan R. Cyclosporine. Drug Intell. Clin. Pharm. 1985. **19**(2): 90–100. https://doi.org/10.1177/106002808501900202.
[67] Nussenblatt R.B., Palestine A.G. Cyclosporine: immunology, pharmacology and therapeutic uses. *Survey Ophthalmol*. 1986. **31**(3): 159–169. https://doi.org/10.1016/0039-6257(86)90035-4.
[68] Borel J.F., Kis Z.L., Beveridge T. The history of the discovery and development of cyclosporine (Sandimmune®). The search for anti-inflammatory drugs: *Case His. Con. Clin*. 1995. 27–63. https://doi.org/10.1007/978-1-4615-9846-6_2.
[69] Patocka J., Nepovimova E., Kuca K., Wu W. Cyclosporine A: chemistry and toxicity–a review. Cur. Med. Chem. 2021. **28**(20): 3925–3934. https://doi.org/10.2174/0929867327666201006153202.
[70] Bennett W.M., Norman D.J. Action and toxicity of cyclosporine. *Ann. Rev. Med*. 1986. **37**: 215–224. https://doi.org/10.1146/annurev.me.37.020186.001243.
[71] Weigert W.M., Offermanns H., Degussa P.S. D-Penicillamine—Production and Properties. *Angew. Chem. Int. Ed. Eng*. 1975. **14**(5): 330–336. https://doi.org/10.1002/anie.197503301.
[72] Van de Stadt R.J., Muijsers A.O., Henrichs A.M., Van der Korst J.K. D-penicillamine: biochemical, metabolic and pharmacological aspects. *Scandin. J. Rheumatol*. 1979. **8**: 13–20. https://doi.org/10.3109/03009747909108229.
[73] Epstein O., Lee R., Boss A.M. et al. D-penicillamine treatment improves survival in primary biliary cirrhosis. *Lancet*. 1981. **317**(8233): 1275–1277. https://doi.org/10.1016/S0140-6736(81)92456-9.
[74] Perrett D. An outline of D-penicillamine metabolism. *Proceed. Royal Soc. Med*. 1977. **70**: 61–64. https://doi.org/10.1177/00359157770700S321.
[76] Neuberger J., Christensen E., Portmann B. *et al*. Double-blind controlled trial of d-penicillamine in patients with primary biliary cirrhosis. *Gut*. 1985. **26**(2): 114–119. https://doi.org/10.1136/gut.26.2.114.
[77] Tedesco K.L., Rybak M.J.. Daptomycin. Pharmacotherapy: *J. Hum. Pharm. Drug Ther*. 2004. **24**(1): 41–57. https://doi.org/10.1592/phco.24.1.41.34802.
[78] Humphries R.M., Pollett S., Sakoulas G. A current perspective on daptomycin for the clinical microbiologist. *Clin. Microb. Rev*. 2013. **26**(4): 759–780. https://doi.org/10.1128/cmr.00030-13.
[79] Enoch D.A., Bygott J.M., Daly M.L., Karas J.A. Daptomycin. *J. Infec*. 2007. **55**(3): 205–213. https://doi.org/10.1016/j.jinf.2007.05.180.
[80] Fenton C., Fenton C., Keating G.M., Curran M.P. Daptomycin. *Drugs*. 2004. **64**(4): 445–455. https://doi.org/10.2165/00003495-200464040-00009.
[81] Raja A., LaBonte J., Lebbos J., Kirkpatrick P. Daptomycin. *Nature Rev. Drug Dis*. 2003.

2(12): 943–944.
https://doi.org/10.1038/nrd1258.
[82] Baltz R.H. Daptomycin: mechanisms of action and resistance, and biosynthetic engineering. *Cur. Opin. Chem. Biol*. 2009. **13**(2): 144–151. https://doi.org/10.1016/j.cbpa.2009.02.031.
[83] Blair H.A. Etelcalcetide: first global approval. *Drugs*. 2016. **76**(18): 1787–1792. https://doi.org/10.1007/s40265-016-0671-3.
[84] Dörr K., Kammer M., Reindl-Schwaighofer R. *et al*. Randomized trial of etelcalcetide for cardiac hypertrophy in hemodialysis. *Circul. Res*. 2021. **128**(11): 1616–1625. https://doi.org/10.1161/CIRCRESAHA.120.318556.
[85] Block G.A., Bushinsky D.A., Cunningham J. *et al*. Effect of etelcalcetide vs placebo on serum parathyroid hormone in patients receiving hemodialysis with secondary hyperparathyroidism: two randomized clinical trials. *JAMA*. 2017. **317**(2): 146–155. https://doi.org/10.1001/jama.2016.19456.
[86] Block G.A., Bushinsky D.A., Cheng S. *et al*. Effect of etelcalcetide vs cinacalcet on serum parathyroid hormone in patients receiving hemodialysis with secondary hyperparathyroidism: a randomized clinical trial. *JAMA*. 2017. **317**(2): 156–164. https://doi.org/10.1001/jama.2016.19468.
[87] Yu L., Tomlinson J.E., Alexander S.T. *et al*. Etelcalcetide, a novel calcimimetic, prevents vascular calcification in a rat model of renal insufficiency with secondary hyperparathyroidism. *Cal. Tissue Int*. 2017. 101(6): 641–653. https://doi.org/10.1007/s00223-017-0319-7.
[88] Freitas P., Pereira L. Etelcalcetide: What we know eight years since its approval. *Nefrologia*. 2025. **45**(2): 116–134. https://doi.org/10.1016/j.nefro.2024.09.004.
[89] Deeks E.D. Difelikefalin: first approval. *Drugs*. 2021. **81**(16): 1937–1944. https://doi.org/10.1007/s40265-021-01619-6.
[90] Fugal J., Serpa S.M. Difelikefalin: a New κ-Opioid receptor agonist for the treatment of hemodialysis-dependent chronic kidney disease–associated pruritus. *Ann. Pharm*. 2023. **57**(4): 480–488. https://doi.org/10.1177/10600280221115889.
[91] Cai X., Wu G., Lin Y., Yang L. Difelikefalin in the treatment of hemodialysis patients with pruritus: a systematic review and meta-analysis. Front. Pharm. 2024. **15**: 1476587. https://doi.org/10.3389/fphar.2024.1476587.
[92] Stark J.G., Noonan P.K., Spencer R.H. *et al*. Pharmacokinetics, metabolism, and excretion of intravenous [14C] Difelikefalin in healthy subjects and subjects on hemodialysis. *Clin. Pharm*. 2023. **62**(9): 1231. https://doi.org/10.1007/s40262-023-01262-2.
[93] Spahia N., Rroji M., Mumajesi S. *et al*. Beyond the itch: chronic kidney disease-associated pruritus, a multimodal approach, and the role of difelikefalin. *Arch. Derma. Res*. 2024. **317**(1): 120. https://doi.org/10.1007/s00403-024-03640-7.
[94] van Gelder T., Lerma E., Engelke K., Huizinga R.B. Voclosporin: a novel calcineurin inhibitor for the treatment of lupus nephritis. *Exp. Rev. Clin. Pharm*. 2022. **15**(5): 515–529. https://doi.org/10.1080/17512433.2022.2092470.
[95] Abdel-Kahaar E., Keller F. Clinical pharmacokinetics and pharmacodynamics of voclosporin. *Clin. Pharm*. 2023. **62**(5): 693–703. https://doi.org/10.1007/s40262-023-01246-2.
[96] Jiang B., Liu J., Li Y. *et al*. Synthesis and Crystallization Research of Voclosporin. *Org. Proc. Res. Develop*. 2024. **28**(4):1151–1158. https://doi.org/10.1021/acs.oprd.3c00518.
[97] Li Y., Palmisano M., Sun D., Zhou S. Pharmacokinetic disposition difference between cyclosporine and voclosporin drives their distinct efficacy and safety profiles in clinical studies. *Clin. Pharm. Adv. App*. 2020. **1**: 83–96. https://doi.org/10.2147/CPAA.S255789.
[98] Mejía-Vilet J.M., Romero-Díaz J. Voclosporin: a novel calcineurin inhibitor for the man-

agement of lupus nephritis. *Exp. Rev. Clin. Immun*. 2021, **17**(9): 937–945. https://doi.org/10.1080/1744666X.2021.1967747.

[99] Najera C., Sansano J.M. Catalytic asymmetric synthesis of α-amino acids. Chem. Rev. 2007. **107**(11): 4584–4671. https://doi.org/10.1021/cr050580o.

[100] Wang Y., Song X., Wang J. *et al.* Recent approaches for asymmetric synthesis of α-amino acids via homologation of Ni(II) complexes. *Amino Acids*. 2017. **49**(9): 1487–1520. https://doi.org/10.1007/s00726-017-2458-6.

[101] Zou Y., Han J., Saghyan A.S. *et al*. Asymmetric Synthesis of Tailor-Made Amino Acids Using Chiral Ni(II)-Complexes of Schiff Bases; An Update of the Recent Literature, *Molecules*. 2020. **25**: 2739. https://doi.org/10.3390/molecules25122739.

[102] Takeda R., Abe H., Shibata N. *et al*. Asymmetric synthesis of α-deuterated α-amino acids. *Org. Biomol. Chem*. 2017. **15**(33): 6978–6983. https://doi.org/10.1039/C7OB01720K.

[103] Sun X.-S., Ou-Yang Q., Xu S.-M. *et al*. Asymmetric synthesis of quaternary α-trifluoromethyl α-amino acids by Ir-catalyzed allylation followed by kinetic resolution. *Chem. Commun*. 2020. **56**(22): 3333–3336. https://doi.org/10.1039/d0cc00845a.

[104] Phillips A.M., Pombeiro A.J. Electrochemical asymmetric synthesis of biologically active substances. *Org. Biomol. Chem*. 2020. **18**(36): 7026–7055. https://doi.org/10.1039/D0OB01425G.

[105] Yuan T., Tang Q., Radefeld K. *et al*. Facile Asymmetric Synthesis of α, α-Disubstituted Amino Acid Derivatives with Gold Redox Catalysis Using a Chiral Auxiliary. *ACS Cat*. 2025. **15**(17): 14845–14852. https://doi.org/10.1021/acscatal.5c02965.

[106] Sato T., Izawa K., Aceña J.L. *et al*. Tailor-Made α-Amino Acids in Pharmaceutical Industry: Synthetic Approaches to (1*R*,2*S*)-1-Amino-2-vinylcyclopropane-1-carboxylic Acid (Vinyl-ACCA). *Eur. J. Org. Chem*. 2016, 2757–2774. https://doi.org/10.1002/ejoc.201600112.

[107] Turcheniuk K.V., Poliashko K.O., Kukhar V.P. *et al*. Efficient asymmetric synthesis of trifluoromethylated β-aminophosphonates and their incorporation into dipeptides. *Chem. Commun*. 2012. **48**(94): 11519–11521. https://doi.org/10.1039/c2cc36702e.

[108] Soloshonok, V.A.; Ohkura, H.; Yasumoto M. Operationally convenient asymmetric synthesis of (*S*)- and (*R*)-3-amino-4,4,4-trifluorobutanoic acid: Part II. Enantioselective biomimetic transamination of 4,4,4-trifluoro-3-oxo-*N*-[(*R*)-1-phenylethyl)butanamide. *J. Fluor. Chem*. 2006. **127**(7): 930–935. https://doi.org/10.1016/j.jfluchem.2006.04.004.

[109] Dennig A., Blaschke F., Gandomkar S. *et al.* Preparative asymmetric synthesis of canonical and non-canonical α-amino acids through formal enantioselective biocatalytic amination of carboxylic acids. *Adv. Syn. Cat*. 2019. **361**(6): 1348–1358. https://doi.org/10.1002/adsc.201801377.

[110] Patel RN. Biocatalysis: Synthesis of key intermediates for development of pharmaceuticals. *ACS Cat*. 2011. **1**(9): 1056–1074. https://doi.org/10.1021/cs200219b.

[111] Wohlgemuth R. Tools and ingredients for the biocatalytic synthesis of metabolites. *Biotech. J.* 2009. **4**(9): 1253–1265, https://doi.org/10.1002/biot.200900002.

[112] Tomoiaga R.B., Nagy L.C., Boros K. *et al*. Engineered Biocatalysts for the Asymmetric Synthesis of d-Phenylalanines. *ACS Cat*. 2025. **15**(9): 7361–7389. https://doi.org/10.1021/acscatal.5c00837.

[113] Petchey M.R., Schneider P., Harwood L.A. Biocatalytic Amino Acid Functionalisation. *ChemMedChem*. 2025. **20**(5): e202400628. https://doi.org/10.1002/cmdc.202400628.

[114] Soloshonok V.A., Kirilenko A.G., Fokina N.A. *et al*. Chemo-enzymatic approach to the synthesis of each of the four isomers of α-alkyl-β-fluoroalkyl-substituted β-amino acids. *Tetrahedron: Asym*. 1994. **5**(7): 1225–1228. https://doi.org/10.1016/0957-4166(94)80163-0.

[115] Soloshonok V.A., Fokina N.A., Rybakova A.V. *et al*. Biocatalytic Approach to Enantiomerically Pure b-Amino Acids. *Tetrahedron: Asym*. 1995. **6**: 1601–1610. https://doi.org/10.1016/0957-4166(95)00204-3.

[116] Pollegioni L., Rosini E., Molla G. Advances in enzymatic synthesis of D-amino acids. *Int. J. Mol. Scien*. 2020. **21**(9): 3206. https://doi.org/10.3390/ijms21093206.

[117] Wang F., Qi H., Li H. *et al*. State-of-the-art strategies and research advances for the biosynthesis of D-amino acids. *Crit. Rev. Biotech*. 2024. **44**(4): 495–513. https://doi.org/10.1080/07388551.2023.2193861.

[118] Soloshonok V.A., Soloshonok I.V., Kukhar V.P., Svedas V.K. Biomimetic transamination of α-alkyl β-keto carboxylic esters. Chemo-enzymatic approach to the stereochemically defined α-alkyl β-fluoroalkyl β-amino acids. *J. Org. Chem*. 1998. **63**(6): 1878–1884. https://doi.org/10.1021/jo971777m.

[119] Chakrabarty S., Romero E.O., Pyser J.B. *et al*. Chemoenzymatic total synthesis of natural products. *Acc. Chem. Res*. 2021. **54**(6): 1374–1384. https://doi.org/10.1021/acs.accounts.0c00810.

[120] Kaspar F., Schallmey A. Chemo-enzymatic synthesis of natural products and their analogs. *Curr. Opin. Biotechnol*. 2022. **77**: 102759. https://doi.org/10.1016/j.copbio.2022.102759.

[121] Sorochinsky A.E., Aceña J.L., Moriwaki H. *et al*. Asymmetric synthesis of α-amino acids via homologation of Ni(II) complexes of glycine Schiff bases; Part 1: Alkyl halide alkylations. *Amino Acids*. 2013. **45**: 691–718. https://doi.org/10.1007/s00726-013-1539-4.

[122] Sorochinsky A.E., Aceña J.L., Moriwaki H. *et al*. Asymmetric synthesis of a-amino acids via homologation of Ni(II) complexes of glycine Schiff bases. Part 2: Aldol, Mannich addition reactions, deracemization and (*S*) to (*R*) interconversion of a-amino acids. *Amino Acids*. 2013. **45**: 1017–1033. https://doi.org/10.1007/s00726-013-1580-3.

[123] Aceña J.L., Sorochinsky A.E., Soloshonok V. Asymmetric synthesis of a-amino acids via homologation of Ni(II) complexes of glycine Schiff bases. Part 3: Michael addition reactions and miscellaneous transformations. *Amino Acids*. 2014. **46**: 2047–2073. https://doi.org/10.1007/s00726-014-1764-5.

[124] Wang J., Lin D., Zhou S. *et al*. Asymmetric Synthesis of Sterically Constrained Linear Trifluoromethyl Containing Amino Acids via Alkylation of Chiral Equivalents of Nucleophilic Glycine and Alanine. J. Org. Chem. 2011. **76**: 684–687. https://doi.org/10.1021/jo102031b.

[125] Tang X., Soloshonok V.A., Hruby V.J. Convenient Asymmetric Synthesis of Enantiomerically Pure 2',6'-Dimethyltyrosine (DMT) via Alkylation of Chiral Nucleophilic Glycine Equivalent. *Tetrahedron: Asym*. 2000. **11**: 2917–2925. https://doi.org/10.1016/S0957-4166(00)00250-0.

[126] Soloshonok V.A., Tang X., Hruby V.J. Large-Scale Asymmetric Synthesis of Novel Sterically Constrained 2',6'-Dimethyl- and a,2',6'-Trimethyltyrosine and –phenylalanine Derivatives via Alkylation of Chiral Equivalents of Nucleophilic Glycine and Alanine. *Tetrahedron*. 2001. **57**: 6375–6382. https://doi.org/10.1016/S0040-4020(01)00504-X.

[127] Ellis T.K., Ueki H., Yamada T. *et al*. The Design, Synthesis and Evaluation of a New Generation of Modular Nucleophilic Glycine Equivalents for the Efficient Synthesis of Sterically Constrained a-Amino Acids *J. Org. Chem*. 2006. **71**: 8572–8578.

[128] Ellis T.K., Hochla V.M., Soloshonok V.A. Efficient synthesis of 2-aminoindane-2-carboxylic acid via dialkylation of nucleophilic glycine equivalent. *J. Org. Chem*. 2003. **68**(12): 4973–4976. https://doi.org/10.1021/jo030065v.

[129] Ellis T.K., Martin C.H., Ueki H., Soloshonok V.A. Efficient, Practical Synthesis of Symmetrically a,a-Disubstituted a-Amino Acids. *Tetrahedron Lett*. 2003. **44**: 1063–1066. https://doi.org/10.1016/S0040-4039(02)02719-3.

[130] Ueki H., Ellis, T. K., Martin C.H. Soloshonok V.A. Efficient Large-Scale Synthesis of Picolinic Acid Derived Ni(II)-Complexes of Glycine. *Eur. J. Org. Chem*. 2003. 1954–1957. https://doi.org/10.1002/ejoc.200200688.

[131] Ellis T.K., Martin C.H., Tsai G.M. *et al*. Efficient Synthesis of Sterically Constrained Symmetrically a,a-Disubstituted a-Amino Acids under Operationally Convenient Conditions. *J. Org. Chem*. 2003. **68**: 6208–6214. https://doi.org/10.1021/jo030075w.

[132] Soloshonok V.A., Tang X., Hruby V.J., Meervelt L.V. Asymmetric Synthesis of a,b-Dialkyl-a-Phenylalanines via Direct Alkylation of Chiral Alanine Derivative with Racemic a-Alkylbenzylbromides. A Case of High Enantiomer Differentiation at Room Temperature. Org. Lett. 2001. **3**: 341–343. https://doi.org/10.1021/ol000330o.

[133] Soloshonok V.A, Boettiger T.U., Bolene S.B. Asymmetric Synthesis of (2*S*,3*S*)- and (2*R*,3*R*)-a,b-Dialkyl-a-Amino Acids via Alkylation of Chiral Ni(II)-Complexes of Aliphatic a-Amino Acids with Racemic a-Alkylbenzylbromides. *Synthesis*. 2008. 2594–2602. https://doi.org/10.1055/s-2008-1067172.

[134] Taylor S.M., Yamada T., Ueki H., Soloshonok V.A. Asymmetric synthesis of enantiomerically pure 4-aminoglutamic acids via methylenedimerization of chiral glycine equivalents with dichloromethane under operationally convenient conditions. *Tetrahedron Lett*. 2004. **45**(50): 9159–9162. https://doi.org/10.1016/j.tetlet.2004.10.111.

[135] Wang J., Liu H., Aceña J.L. *et al*. Synthesis of bis-α,α-amino acids through diastereoselective bis-alkylations of chiral Ni(II)-complexes of glycine. *Org. Biomol. Chem*. 2013. **11**: 4508–4515. https://doi.org/10.1039/C3OB40594J.

[136] Soloshonok V.A., Kukhar V.P., Galushko S.V. *et al*. General Method for the Synthesis of Enantiomerically Pure b-Hydroxy-a-Amino Acids, Containing Fluorine Atoms in the Side Chains. Case of Stereochemical Distinction Between Methyl and Trifluoromethyl Groups. X-Ray Crystal and Molecular Structure of the Nickel(II) Complex of (2*S*,3*S*)-2-(Trifluoromethyl)threonine. *J. Chem. Soc. Perkin Trans 1*. 1993. 3143–3155. https://doi.org/10.1039/P19930003143.

[137] Soloshonok V.A., Avilov D.V., Kukhar V.P. Highly Diastereoselective Asymmetric Aldol Reactions of Chiral Ni(II)-Complex of Glycine with Trifluoromethyl Ketones. *Tetrahedron: Asym*. 1996. **7**: 1547–1550. https://doi.org/10.1016/0957-4166(96)00177-2.

[138] Soloshonok V.A., Avilov D.V., Kukhar V.P. Asymmetric Aldol Reactions of Trifluoromethyl Ketones with a Chiral Ni(II) Complex of Glycine: Stereocontrolling Effect of the Trifluoromethyl Group. *Tetrahedron*. 1996. **52**: 12433–12442. https://doi.org/10.1016/0040-4020(96)00741-7.

[139] Kawamura A., Moriwaki H., Röschenthaler G.-V. *et al*. Synthesis of (2*S*,3*S*)-β-(trifluoromethyl)-α,β-diamino acid by Mannich addition of glycine Schiff base Ni(II)

complexes to *N-tert*-butylsulfinyl-3,3,3-trifluoroacetaldimine. *J. Fluor. Chem*. 2015. **171**: 67–72. https://doi.org/10.1016/j.jfluchem.2014.09.013.

[140] Soloshonok V.A., Avilov D.V., Kukhar V.P. *et al*. Highly Diastereoselective aza-Aldol Reactions of a Chiral Ni(II) Complex of Glycine with Imines. An Efficient Asymmetric Approach to 3-Perfluoroalkyl-2,3-Diamino Acids. *Tetrahedron Lett*. 1997. **38**: 4671–4674. https://doi.org/10.1016/S0040-4039(97)00963-5.

[141] Soloshonok V.A., Cai C., Hruby V.J. A Practical Asymmetric Synthesis of Enantiomerically Pure 3-Substituted Pyroglutamic Acids and Related Compounds. *Angew. Chem. Int. Ed*. 2000. **39**: 2172–2175. *Angew. Chem*. 2000. **112**: 2256–2259. https://doi.org/10.1002/1521-3757(20000616)112:12<2256::AID-ANGE2256>3.0.CO;2-9.

[142] Soloshonok V.A., Cai C., Hruby V.J. A Unique Case of Face Diastereoselectivity in the Michael Addition Reactions Between Ni(II)-Complexes of Glycine and Chiral 3-(*E*-enoyl)-1,3-oxazolidin-2-ones. *Tetrahedron Lett*. 2000. **41**: 9645–9649. https://doi.org/10.1016/S0040-4039(00)01737-8.

[143] Soloshonok V.A., Cai C., Hruby V.J. Asymmetric Michael Addition Reactions of Chiral Ni(II) Complex of Glycine with *N*-(Enoyl) oxazolidinones: Improved Reactivity and Stereochemical Outcome. *Tetrahedron: Asym*. 1999. **10**: 4265–4269. https://doi.org/10.1016/S0957-4166(99)00483-8.

[144] Soloshonok V.A., Cai C., Hruby V.J. Toward Design of a Practical Methodology for Stereocontrolled Synthesis of c-Constrained Pyroglutamic Acids and Related Compounds. Virtually Complete Control of Simple Diastereoselectivity in the Michael Addition Reactions of Glycine Ni(II) Complexes with *N*-(Enoyl)oxazolidinones. *Tetrahedron Lett*. 2000. **41**: 135–139. https://doi.org/10.1016/S0040-4039(99)02018-3.

[145] Soloshonok V.A., Ueki H., Ellis T.K. *et al*. Application of Modular Nucleophilic Glycine Equivalents for Truly Practical Asymmetric Synthesis of b-Substituted Pyroglutamic Acids. *Tetrahedron Lett*. 2005. **46**: 1107–1110. https://doi.org/10.1016/j.tetlet.2004.12.093.

[146] Soloshonok V.A., Cai C., Hruby V.J. (*S*)- or (*R*)-*N*-(*E*-enoyl)-4-phenyl-1,3-oxazolidin-2-ones: Ideal Michael Acceptors to Afford a Virtually Complete Control of Simple and Face Diastereoselectivity in Addition Reactions with Glycine Derivatives. *Org. Lett*. 2000. 2: 747–750. https://doi.org/10.1021/ol990402f.

[147] Shigeno Y., Han J., Soloshonok V.A. *et al*. Asymmetric synthesis of (*S*)-3-methyleneglutamic acid and its *N*-Fmoc derivative via Michael addition of chiral glycine Schiff base Ni(II) complex with enol tosylates. *Chirality*. 2021. **33**: 115–123. https://doi.org/doi.org/10.1002/chir.23291.

[148] Cai, C.; Soloshonok, V.A.; Hruby V.J. Michael Addition Reactions between Chiral Ni(II) Complex of Glycine and 3-(*trans*-Enoyl)oxazolidin-2-ones. A Case of Electron Donor–Acceptor Attractive Interaction-Controlled Face Diastereoselectivity. *J. Org. Chem*. **2001**, *66*(4), 1339–1350. https://doi.org/10.1021/jo0014865.

[149] Soloshonok V.A., Avilov D.V., Kukhar V. P. *et al*. An Efficient Asymmetric Synthesis of (2*S*,3*S*)-3-Trifluoromethylpyroglutamic Acid. *Tetrahedron Lett*. 1997. **38**: 4903–4904. https://doi.org/10.1016/S0040-4039(97)01054-X.

[150] Soloshonok V.A., Cai C., Hruby V.J. *et al*. Rational Design of Highly Diastereoselective, Organic Base-Catalyzed, Room Temperature Michael Addition Reactions. *J. Org. Chem*. 2000. **65**: 6688-6696.

https://doi.org/10.1021/jo0008791.

[151] Cai M., Cai C., Mayorov A.V. *et al*. Biological and conformational study of b-substituted prolines in MT-II template: steric effects leading to human MC5 receptor selectivity. *J. Pep. Res*. 2004. **63**: 116–131. https://doi.org/10.1111/j.1399-3011.2003.00105.x.

[152] Qiu W., Gu X., Soloshonok V.A. *et al*. Stereoselective synthesis of conformationally constrained reverse turn dipeptide mimetics. *Tetrahedron Lett*. 2001. **42**(2): 145–148. https://doi.org/10.1016/S0040-4039(00)01864-5.

[153] Tokunaga E., Akiyama H., Soloshonok V.A. *et al*. Biological evaluation of both enantiomers of fluoro-thalidomide using human myeloma cell line H929 and others. *PLoS ONE*. 2017. **12**(8): e0182152. https://doi.org/10.1371/journal.pone.0182152.

[154] Soloshonok V.A., Yamada T., Sakaguchi K., Ohfune Y. Concise Asymmetric Synthesis of Configurationally Stable 4-trifluoromethyl Thalidomide, *Fut. Med. Chem*. 2009. **1**: 897–908. https://doi.org/10.4155/fmc.09.63.

[155] Yamada T., Okada T., Sakaguchi K. *et al*. Efficient Asymmetric Synthesis of Novel 4-Substituted and Configurationally Stable Analogs of Thalidomide. *Org. Lett*. 2006. **8**: 5625–5628. https://doi.org/10.1021/ol0623668.

[156] Yamada T., Sakaguchi K., Shinada T. *et al*. Efficient asymmetric synthesis of the functionalized pyroglutamate core unit common to oxazolomycin and neooxazolomycin using Michael reaction of nucleophilic glycine Schiff base with a,b-disubstituted acrylate. *Tetrahedron: Asym*. 2008. **19**: 2789–2795. https://doi.org/10.1016/j.tetasy.2008.11.036.

[157] Oyama K., Han J., Moriwaki H. *et al*. Synthesis of Ahod moiety of ralstonin A using amino acid Schiff base Ni(II)-complex chemistry. *Helv. Chim. Acta*. 2020. **103**: e2000077. https://doi.org/10.1002/hlca.202000077.

[158] Kawashima A., Shu S., Takeda R. *et al*. Advanced asymmetric synthesis of (1*R*,2*S*)-1-amino-2-vinylcyclopropanecarboxylic acid by alkylation/cyclization of newly designed axially chiral Ni(II) complex of glycine Schiff base. *Amino Acids*. 2016. **48**: 973–986. https://doi.org/10.1007/s00726-015-2138-3.

[159] Kawashima A., Xie C., Mei H. *et al*. Soloshonok, Asymmetric synthesis of (1*R*,2*S*)-1-amino-2-vinylcyclopropanecarboxylic acid by sequential SN_2–SN_2, dialkylation of (*R*)-*N*-(benzyl)proline-derived glycine Schiff base Ni(II) complex, *RSC Adv*. 2015. **5**: 1051–1058. https://doi.org/10.1039/C4RA12658K.

[160] Wzorek A., Han J., Ono T. *et al*. Cutting-Edge Strategies in the Asymmetric Synthesis of α-Aminocyclopropyl Carboxylic Acids: Essential Scaffolds for Drug Discovery. *Ukr. Chem. J*. 2025. **91**(10): 27–71. https://doi.org/10.33609/2708-129X.91.10.2025.27-71.

[161] Ueki H., Ellis T.K., Martin C.H. *et al*. Improved Synthesis of Proline Derived Ni(II)-Complexes of Glycine, a Versatile Chiral Equivalents of Nucleophilic Glycine for General Asymmetric Synthesis of a-Amino Acids. *J. Org. Chem*. 2003. **68**: 7104–7107. https://doi.org/10.1021/jo0301494.

[162] Soloshonok V.A., Ueki H., Ellis T.K. New Generation of Nucleophilic Glycine Equivalents. *Tetrahedron Lett*. 2005. **46**: 941–944. https://doi.org/10.1016/j.tetlet.2004.12.093.

[163] Soloshonok V.A., Ueki H., Moore J.L., Ellis T.K. Design and Synthesis of Molecules with Switchable Chirality via Formation and Cleavage of Metal-Ligand Coordination Bonds, *J. Am. Chem. Soc*. 2007. **129**: 3512–3513. https://doi.org/10.1021/ja067995r.

[164] Han J., Romoff T.T., Moriwaki H.H. *et al*. Development of Hamari Ligands for

Practical Asymmetric Synthesis of Tailor-Made Amino Acids. *ACS Omega*. 2019. **4**: 18942–18947. https://doi.org/10.1021/acsomega.9b02940.

[165] Mei H., Han J., Takeda R. *et al.* Practical Method for Preparation of (*S*)-2-Amino-5,5,5-trifluoropentanoic Acid via Dynamic Kinetic Resolution. *ACS Omega*. 2019. **4**: 11844–11851. https://doi.org/10.1021/acsomega.9b01537.

[166] Han J., Liu H., Wang J. *et al.* Hamari's contribution to the asymmetric synthesis of tailor-made amino acids. *Ukr. Chem. J*. 2024. **90**(10): 88–134. https://doi.org/10.33609/2708-129X.90.10.2024.88-134.

[167] Jörres M., Aceña J.L., Soloshonok V.A., Bolm C. Asymmetric Carbon-Carbon Bond Formations under Solvent-Less Conditions in Ball Mills. *ChemCatChem*. 2015. **7**: 1265–1269. https://doi.org/10.1002/cctc.201500102.

[168] Jörres M., Chen X., Aceña J.L. *et al.* Asymmetric Synthesis of a-Amino Acids under Operationally Convenient Conditions. *Adv. Synth. Catal*. 2014. **356**: 2203–2208. https://doi.org/10.1002/adsc.201400405.

[169] Bergagnini M., Fukushi K., Han J. *et al.* NH-type of chiral Ni(II) complexes of glycine Schiff base: design, structural evaluation, reactivity and synthetic applications. *Org. Biomol. Chem*. 2014. 12: 1278–1291. https://doi.org/10.1039/C3OB41959B.

[170] Takeda R., Kawamura A., Kawashima A. *et al.* Second-order asymmetric transformation and its application for the practical synthesis of α-amino acids. *Org. Biomol. Chem*. 2018. **16**: 4968–4972. https://doi.org/10.1039/C8OB00963E.

[171] Soloshonok V.A., Ellis T.K. Design and Synthesis of a New Generation of "NH" Ni(II) Complexes of Glycine Schiff Bases and Their Unprecedented C-H vs. N-H Chemoselectivity in the Alkyl Halide Alkylations and Michael addition Reactions. *Synlett*. 2006. 533–538. https://doi.org/10.1055/s-2006-926252.

[172] Romoff T.T., Palmer A.B., Mansour N. *et al.* Scale-up Synthesis of (*R*)- and (*S*)-*N*-(2-benzoyl-4-chlorophenyl)-1-(3,4-dichlorobenzyl)pyrrolidine-2-carboxamide hydrochloride, a Versatile Reagent for Preparation of Tailor-made α- and β-Amino Acids in Enantiomerically Pure Form. *Org. Process Res. Dev*. 2017. **21**: 732–739. https://doi.org/10.1021/acs.oprd.7b00055.

[173] Romoff T.T., Ignacio B.G., Mansour N. *et al.* Large-Scale Synthesis of the Glycine Schiff Base Ni(II) Complex Derived from (*S*)- and (*R*)-*N*-(2-Benzoyl-4-chlorophenyl)-1-[(3,4-dichlorophenyl)methyl]-2-pyrrolidinecarboxamide. *Org. Process Res. Dev*. 2020. **24**: 294–300. https://doi.org/10.1021/acs.oprd.9b00399.

[174] Nian Y., Wang J., Moriwaki H. *et al.* Analysis of crystallographic structures of Ni(II) complexes of α-amino acid Schiff bases; Elucidation of the substituents effect on stereochemical preferences *Dalton Trans*. 2017. **46**: 4191–4198. https://doi.org/10.1039/C7DT00014F.

[175] Nian Y., Wang J., Zhou S. *et al.* Recyclable Ligands for the Non-Enzymatic Dynamic Kinetic Resolution of Challenging a-Amino Acids. *Angew. Chem. Int. Ed*. 2015. **54**: 12918-12922. https://doi.org/10.1002/anie.201507273.

[176] Wang S., Zhou S., Wang J. *et al.* Chemical Dynamic Thermodynamic Resolution and *S*/*R* Interconversion of Unprotected Unnatural Tailor-made a-Amino Acids. *J. Org. Chem*. 2015. **80**: 9817–9830. https://doi.org/10.1021/acs.joc.5b01292.

[177] Takeda R., Kawamura A., Kawashima A. *et al.* Chemical Dynamic Kinetic Resolution and (*S*)/(*R*)-Interconversion of Unprotected α-Amino Acids. *Angew. Chem. Int. Ed*. 2014. **53**: 12214–12217.

https://doi.org/10.1002/anie.201407944.
[178] Soloshonok V.A., Ellis T.K., Ueki H., Ono T. Resolution/Deracemization of Chiral a-Amino Acids Using Resolving Reagents with Flexible Stereogenic Centers. *J. Am. Chem. Soc*. 2009. **131**: 7208-7209. https://doi.org/10.1021/ja9026055.
[179] Zhou S., Wang J., Chen X. *et al*. Chemical Kinetic Resolution of Unprotected b-Substituted-b-Amino Acids Using Recyclable Chiral Ligands. *Angew. Chem. Int. Ed*. 2014. **53**: 7883–7886. https://doi.org/10.1002/anie.201403556.
[180] Sorochinsky A.E., Ueki H., Aceña J.L. *et al*. Chemical approach for interconversion of (*S*)- and (*R*)-α-amino acids. *Org. Biomol. Chem*. 2013. **11**: 4503–4507. https://doi.org/10.1039/C3OB40541A.
[181] Nian Y., Wang J., Zhou S. *et al*. Purely Chemical Approach for Preparation of D-alpha-amino Acids via (*S*)-to-(*R*)-interconversion of Unprotected Tailor-made alpha-amino Acids. *J. Org. Chem*. 2016. 81: 3501–3508. https://doi.org/10.1021/acs.joc.5b02707.
[182] Sorochinsky A.E., Ueki H., Aceña J.L. *et al*. Chemical deracemization and (*S*) to (*R*) interconversion of some fluorine-containing α-amino acids. *J. Fluor. Chem*. 2013. **152**: 114–118. https://doi.org/10.1016/j.jfluchem.2013.02.022.

Стаття надійшла: 25.04.2026.
Статтю прийнято до друку: 25.05.2026.
Статтю опубліковано: 25.06.2026.